Full characterization of the initial microstructure

Authors : Mrs. Onorbe ELVIRA (CIEMAT), V. Marques, K. Naziris, M. Kolluri (NRG), P.Chekhonin, A. Ulbricht (HZDR), E. Oñorbe, M. Hernández-Mayoral (CIEMAT), J. Lydman, Y. Ge (VTT), D. Sharma, A. Etienne, P. Pareige, B. Radiguet (CNRS), J. Degmova (STUBA)

STRUMAT-LTO - Contract Number: 945272

Project officer: Panagiotis Manolatos

Document title	Full characterization of the initial microstructure
Author(s)	Mrs. Onorbe ELVIRA, V. Marques, K. Naziris, M. Kolluri (NRG), P.Chekhonin, A. Ulbricht (HZDR), E. Oñorbe, M. Hernández-Mayoral (CIEMAT), J. Lydman, Y. Ge (VTT), D. Sharma, A. Etienne, P. Pareige, B. Radiguet (CNRS), J. Degmova (STUBA)
Number of pages	87
Document type	Deliverable
Work Package	WP3
Document number	D3.1
Issued by	CIEMAT
Date of completion	2022-09-05 15:29:28
Dissemination level	Public

Summary

Full characterization of the selected materials (described in the Proposal Submission Form) in the initial condition and after irradiation (irradiation conditions describe in LYRA-304/10 Irradiation Report) is necessary to reach the objectives set in WP3. The aim of Task 3.1 is the description of the initial microstructure of the different selected materials analysed by partners employing different techniques.

Approval

Date	By
2022-09-05 15:31:26	Dr. Andreas ULBRICHT (HZDR)
2022-09-05 16:08:09	Dr. Akos HORVATH (MTA EK)

D.3.1. Test matrix and characterization of the initial microstructures

Version N°1

Contributors:

V. Marques, K. Naziris, M. Kolluri (NRG)

P.Chekhonin, A. Ulbricht (HZDR)

E. Oñorbe, M. Hernández-Mayoral (CIEMAT)

J. Lydman, Y. Ge (VTT)

D. Sharma, A. Etienne, P. Pareige, B. Radiguet (CNRS)

J. Degmova (STUBA)

Document Information

Grant Agreement Number	945272
Project Title	STRUctural MATerials research for safe Long Term Operation of LWR NPPs
Project Acronym	STRUMAT-LTO
Project Start Date	01 September 2020
Related Work Package	WP3
Related Task(s)	D3.1
Lead Organisation	CIEMAT
Submission Date	12 August 2022
Dissemination Level	Public

History

Date	Submitted by	Reviewed by	Version (Notes)
22 August 2021	Elvira Oñorbe		V Nº1

Table of Contents

List of figures

List of tables

Abbreviations and acronyms

Acronym	Description
WP	Work Package
MS	Milestone
TEM	Transmission Electron Microscopy
SEM	Scanning Electron Microscopy
EBSD	Electron Backscattered Scanning Diffraction
EDS	Energy Dispersive X-ray spectroscopy
LOM	Light Optical Microscopy
APT	Atom Probe Tomography
PAS	Positron Annihilation Spectroscopy
FEG	Field Emission Gun
SE	Secondary electron
BSE	Backscatter electron
BF	Bright Field
WBDF	Weak Beam Dark Field
CBED	Convergent Beam Electron Diffraction
FIB	Focused Ion Beam
PALS	Positron Annihilation Lifetime Spectroscopy
FWHM	Full width at half maximum
(C)DBS	(Coincidence) Doppler broadening spectroscopy
KAM	Kernel Average Misorientation
MOA	Misorientation Angle

Summary

Full characterization of the selected materials (described in the Proposal Submission Form) in the initial condition and after irradiation (irradiation conditions describe in LYRA-304/10 Irradiation Report) is necessary to reach the objectives set in WP3. The aim of Task 3.1 is the description of the initial microstructure of the different selected materials analysed by partners employing different techniques.

1. Introduction

The aim of this Task is the description of the initial microstructure of the selected materials. The experimental work and studied materials was previously described in MS9 and a summary is shown in Table 1.

Partner	Reference material	Activity
NRG	Model steels K, L, M and N	TEM
HZDR	Model steels A, B, C, F, G and H	SEM/EBSD, EDX
CIEMAT	Model steels A, B, C, F, G and H	SEM, (S)TEM
VTT	Model steels A, B and C	Hardness, LOM, SEM, (S)TEM
CNRS	Model steels A, B, C, F, G and H	APT
STUBA	Model steels A-H, K, L, M and N	PAS

Table 1: Experimental work within Task 3.1

The work carried out by each partner is described in this deliverable as well as a discussion according to the obtained results.

2. Materials

Different steels and weld have been selected in order to explain the synergetic effects of VVER-1000 steels typical alloying elements in terms of irradiation-induced microstructures and mechanical properties changes. The selection of materials and fabrication routes are well described in the Technical Report: "Origin and Manufacturing of the LYRA-10 Specimens".

2.1.   Model steels

The chemical composition of model steels are shown in Table 2.

Model	C	Si	Mn	Cr	Ni	Mo	V	Cu	S	P
A	0.11	0.28	0.43	2.22	<0.02	0.71	0.10	0.09	0.008	0.010
B	0.11	0.26	0.38	2.19	0.99	0.70	0.10	0.10	0.008	0.010
C	0.12	0.24	0.38	2.13	2.00	0.69	0.10	0.10	0.008	0.010
D	0.11	0.23	0.83	2.13	2.00	0.68	0.10	0.09	0.008	0.009
E	0.12	0.33	0.77	2.16	1.02	0.70	0.10	0.10	0.008	0.009
F	0.12	0.33	1.37	2.15	1.02	0.70	0.10	0.10	0.008	0.010
G	0.11	0.32	1.36	2.06	1.99	0.69	0.10	0.10	0.008	0.009
H	0.12	0.51	1.31	2.07	2.00	0.69	0.10	0.10	0.008	0.010
K	0.17	0.35	0.78	0.10	0.58	0.64	-	0.07	0.005	0.009
L	0.18	0.35	0.77	0.08	0.96	0.63	-	0.05	0.005	0.010
M	0.16	0.37	0.74	0.09	1.90	0.61	-	0.05	0.005	0.010
N	0.16	0.33	1.27	0.07	1.97	0.63	-	0.06	0.005	0.010

Table 2: Chemical composition of model steels

2.2. Realistic welds

The chemical composition of welds are shown in Table 3.

Weld	C	Si	Mn	Cr	Ni	Mo	V	Cu	S	P	Co
A	0.07	0.18	0.57	2.07	1.30	0.59	0.09	0.06	0.007	0.011	0.02
B	0.06	0.31	0.56	2.04	1.59	0.60	0.09	0.06	0.009	0.007	0.02
C	0.05	0.32	0.60	1.95	1.87	0.58	0.08	0.06	0.010	0.007	0.02
D	0.06	0.29	0.72	2.01	1.57	0.59	0.09	0.06	0.009	0.006	0.02
E	0.05	0.30	0.89	2.00	1.94	0.57	0.09	0.06	0.009	0.006	0.02
F	0.06	0.29	1.07	2.04	1.26	0.58	0.09	0.06	0.009	0.006	0.02
G	0.06	0.30	1.07	2.04	1.57	0.59	0.09	0.06	0.001	0.007	0.02

H	0.06	0.32	1.08	1.98	1.89	0.58	0.09	0.06	0.001	0.007	0.02

Table 3: Chemical composition of realistic welds.

3. Method

3.1. Optical Microscopy

The 6 model steels studied at CIEMAT (A, B, C, F, G and H) were in first case observed by means of optical microscopy. Samples were prepared by conventional polishing techniques and etched with Vilella´s reagent to reveal the grain structure of each model steel.

The same model steels were also characterized at VTT using a Zeiss Axio Observer 7 light optical microscope.

3.2. Scanning Electron Microscopy

The unirradiated model steels studied at CIEMAT were supplied by HZDR in the form of plates of 12x5x0.4 mm^3. The microstructure of the materials before irradiation was analysed using Scanning Electron Microscopy (SEM) on a Hitachi SU6600 field emission gun scanning electron microscope (FEG-SEM) equipped with an Oxford Instruments HKL Nordlys detector. Samples were prepared by conventional polishing techniques and etched with Vilella's reagent to reveal the bainitic microstructure. The analysis carried out at CIEMAT was focused in the quantification of the size and density of the precipitates presents in the materials.

In the case of HZDR, electro discharge machining was applied to produce $10 \times 10 \times 1$ mm^3 sized sample of each of the 6 materials (A, B, C, F, G and H model steels). These samples were subsequently grinded with SiC paper and diamond paste. The last preparation step was done by mechanical polishing with 60 nm silica suspension (MasterMet).

SEM overview imaging using secondary electron (SE) as well as backscatter electron (BSE) imaging was done in a EVO 50 SEM (Zeiss) equipped with a tungsten filament operated at 15 kV acceleration voltage.

Using the same samples, Electron Backscatter Diffraction (EBSD) measurements were performed in a NVision 40 SEM (Zeiss) equipped with a field emission gun (FEG) and a Bruker EBSD system. The acceleration voltage was set to 16 kV, the beam current to about 10 nA using a 120 µm aperture, while the integration time per EBSD frame was set between 60 ms and 65 ms. In order to ensure sufficient statistics, the mapping dimension was always set to 1400 × 1050 mapping points arranged in a square grid with step size of 200 nm.

The evaluation of the EBSD measurements was done by an in-house written software (P. Chekhonin). Data correction was applied using the neighborhood orientation of unindexed points. Additionally, two loops to correct outliers were done. The data correction resulted in only insignificant changes in the data, as the original indexation rate was 96% for model alloy

A, and above 99% for the other 5 model alloys. In the present evaluation, grains are defined as areas enclosed by grain boundaries with a misorientation angle (MOA) ≥ 5°. First, the grains were identified and the area of each grain is calculated. Afterwards, the grain size is calculated as the equivalent circle diameter from the averaged grain area. Grains with less than 5 EBSD mapping pixels (≡ diameter < 0.5 μm) were not considered for grain size determination. Grains at mapping boundaries are included.

VTT fractography of Model steels A, B and C was carried out using a Zeiss Crossbeam 540 scanning electron microscope.

Finally, an SEM was used at NRG for observing the general microstructure (matrix, precipitates) of model steels K, L, M and N. SEM analyses were conducted in a Hitachi S-3700N. Samples for SEM analysis were cut from broken KLST specimens, as indicated in Figure 1.
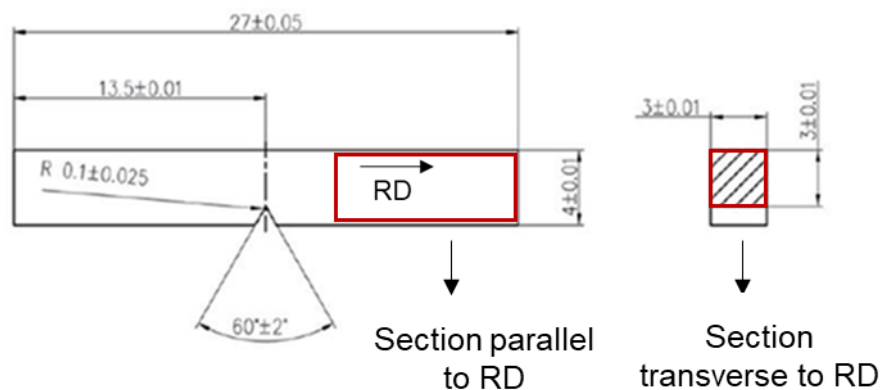
Figure 1: Scheme containing drawing of KLST specimen and the sections from which samples were taken for SEM analysis (outlined in red).

Sample preparation for SEM investigation consisted of the following steps: grinding with SiC paper from grit 220 up to 4000; mechanical polishing with diamond suspensions of 3 μm and 1 μm; final mechanical polishing step with colloidal silica. The samples were then etched with Nital 2% solution (2% HNO_3 + 95% ethanol), by immersion for approximately 10-15 s.

The software Thermo-Calc v.2021a was used to calculate the equilibrium diagrams of the evaluated steels. For grades K, L and M, which have the same chemical composition, except for the variation in Ni content, the composition used for the calculation was Fe-0.17C-0.78Mn-0.10Cr-0.96Ni-0.6Mo (Ni content was made variable) and for grade N the composition used was Fe-0.17C-1.27Mn-0.10Cr-0.96Ni-0.6Mo (Ni content was made variable). The database used was TCFE11: steels/Fe-alloys v.11.0.

3.3. Transmission Electron Microscopy

The microstructural features of A, B, C, F, G and H model steels were also studied by transmission electron microscopy (TEM) at CIEMAT, on 3mm discs drilled form the plates supplied by HZDR. The surface of electron transparent samples analysed were prepared with

a final electrolytic polishing, using a mixture of 5% perchloric acid and methanol at -60 ºC. TEM analysis was carried out using standard imaging methods of Bright Field (BF) and Weak Beam Dark Field (WBDF) in a FEG (S)TEM (Talos F200X, FEI) operating at 200 keV and a JEOL-JEM2010 microscope available at CIEMAT operating at 200 keV. Convergent Beam Electron Diffraction (CBED) method was employed to determine the specimen thickness in those regions where dislocation density was measured.

The Talos F200 STEM was equipped with a chemical analysis system via energy-dispersive X-ray spectroscopy (EDS) that was used to obtain better insight into the elemental components of the different precipitates found in the model steels.

Model steels A, B and C were also characterized by means of TEM by VTT. The grain morphology, elemental maps and precipitates of Model steels A, B, and C are studied with scanning/transmission electron microscope, Thermo Scientific Talos F200X with SuperX energy Dispersive spectrometry system. TEM foil was cut by electrical discharge machining (EDM) and ground with emery paper to about 100 μm. Final thinning of foil is electropolished using a Struers Tenupol-5 twin jet polisher with 6% Perchloric acid in 10% Butoxyethanol and ethanol.

Finally, a TEM was used at NGR to characterize the dislocation/defect structure prior to irradiation of model steels K, L, M and N. TEM investigation was carried out in a JEOL JEM-1200ex, operating at 120 kV. Samples for TEM analysis were sliced from the grips of broken tensile specimens, as shown in Figure 2.
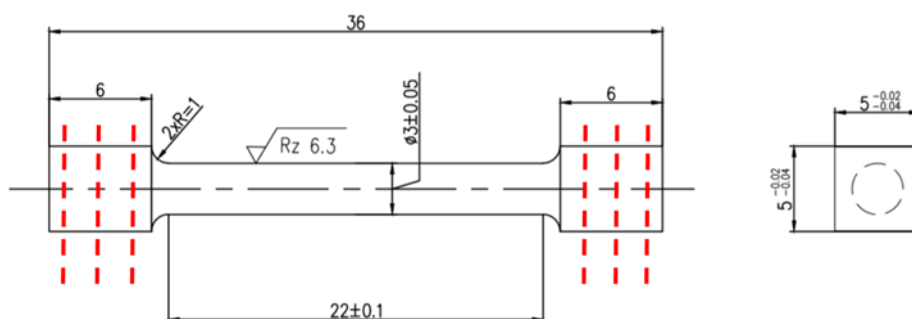
Figure 2: Scheme containing drawing of tensile specimen. The dashed lines represent the orientation for extraction of TEM samples.

Sample preparation for TEM analysis consisted of grinding the samples up to a thickness of ~ 80 μm (in many cases thickness was of 26 to 80 μm), with final grinding step done using grit 4000 SiC; punching discs of 3 mm diameter and final thinning step is done with electropolishing. The electrolyte used is composed of 5% perchloric acid and 95% methanol; electropolishing was done at temperatures ranging from -20 ºC to -30 ºC.

3.4. Atom Probe Tomography

The as-received (unirradiated) alloys were mounted in epoxy using a hot mounting method. The samples were then mechanically ground to 9 µm using diamond pads, followed by sequential polishing down to 0.04 µm. The polished samples were finally cleaned with soap under running water.

To ensure the reproducibility of APT observations, two chunks were lifted out from two different locations on the samples using focused ion beam (FIB) milling, as shown in Figure 3. At least three tips were prepared from each chunk using FIB annular milling. One such tip is shown in Figure 3. The final stage of tip preparation included a low-energy cleanup at 2 kV and 90 pA to reduce the Ga damage of the tips.

APT characterisation was carried out on a Cameca LEAP 4000X HR and a Cameca LEAP 5000 XR at Groupe de Physique des Matériaux (GPM), Rouen, France. All the samples were analysed using the electric mode, where the sample temperature was kept at 50 K. The detection rate, pulse fraction, and pulse frequency were kept as 0.1%, 20%, and 200 kHz, respectively.

The APT data was reconstructed using the IVAS commercial software (3.8.10 version) from Cameca. The initial several thousands of atoms were discarded during reconstruction as the tip was being aligned and had a higher Ga and O concentration during the start of the APT analysis. A standard image compression factor value of 1.65 was used for the reconstruction, whilst the k values were determined by calibrating the d spacing values for the poles, such as (011), (002), or (222). The atom files were then saved from these reconstructions, which were then imported into GPM3D-soft software, developed by GPM, to perform further analysis. Each peak (mass to charge ratio) of the mass spectrum was identified and deconvoluted based on the natural abundances of several isotopes of different elements. Subsequently, elemental composition, three-dimensional (3D) representation of atoms (atom maps), and atomic distance distribution of each element were extracted from the reconstructed data.
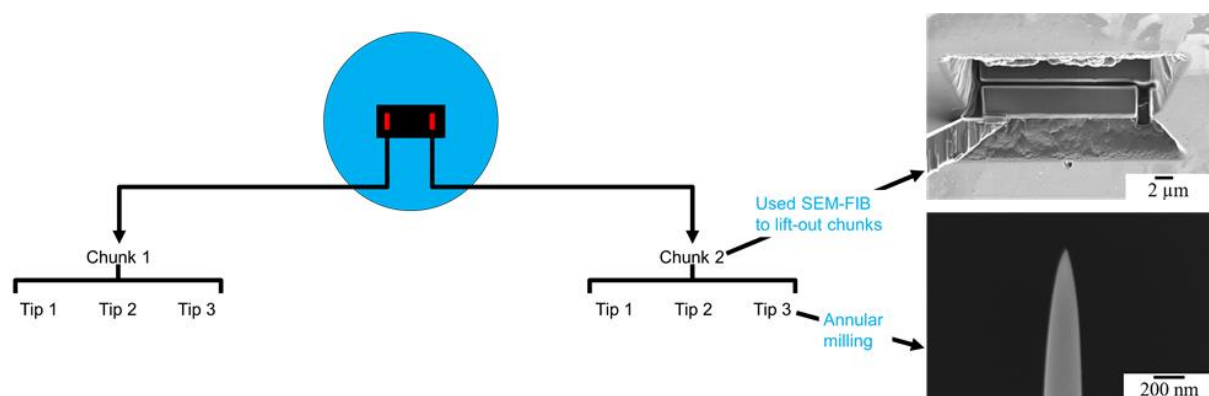
Figure 3: Schematics of the tip preparation from the unirradiated samples. Two chunks were lifted out using FIB milling to measure at least three tips from each chunk. Tips were prepared using annular milling under FIB.

3.5. Positron Annihilation Spectroscopy

Positron annihilation spectroscopy (PAS) is a well-established non-destructive spectroscopic method for evaluating defect size (size of clusters), defects density and their chemical environment. The radioactive sodium 22Na with a half-lifetime of 2.6 years is used as a positron source. The 22Na isotope emits one positron during its decay to 22Ne. As the 22Ne is in the excited state, it emits gamma particles with the kinetic energy of 1274 keV to get into the ground state. This gamma is emitted approximately after 3.7 ps and gives the information about the positron birth. The positron source usually consists of two thin capton foils with a small, dried drop of radioactive water solution of salt with 22Na placed between these two foils, as can see in Figure 4.

a)   **b)**

$$^{22}_{11}Na \rightarrow \, ^{22}_{10}Ne + \, \beta^+ + \, \upsilon_e + \, \gamma$$
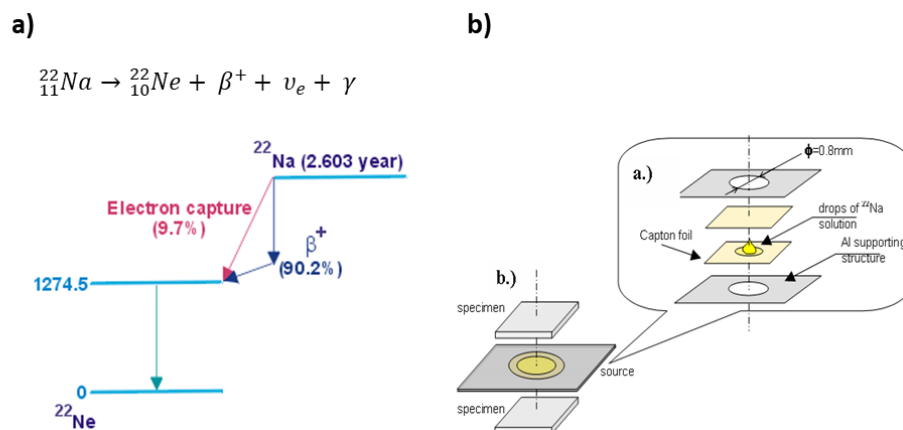
Figure 4: Positron source a) decay scheme of ^{22}Na and b) construction of the source.

During the measurements, the samples of investigated materials are placed from both sides of the source in the so-called "sandwich geometry" (see Figure 4). Positrons are emitted from the source into the samples with a maximum kinetic energy of around 540 keV and a maximum depth approximately 120 μm. Their most potential energy is close to 120 keV. There are many techniques using positron annihilation to study materials' properties. In this project, two of them are used: positron annihilation lifetime spectroscopy and Doppler broadening spectroscopy.

3.5.1. Positron annihilation lifetime spectroscopy (PALS)

This technique is based on a positron (e+) annihilation with electron (e-), where the positron is produced by β+ decay. The γ-photon with the energy of 1270 keV is emitted at the same time, providing a start signal for PALS. Afterwards, positron thermalizes (duration of ~1 ps) and diffuses in the specimen. Subsequently, the position is most likely trapped in the vacancy-type defect due to its attractive potential of volume defects caused by a lack of positively charged nuclei (repulsive forces). After some time, depending on the defect size and electron density, the positron recombines with the electron and annihilates, which leads to an emission of two γ-photons ($E_0 = m_e c^2 = 511$ keV – stop signal for PALS), as can be seen in Figure 5. These gamma quanta can be detected as a signal of positron death. If we detect the positron birth energy and the energy of annihilation, the positron lifetime (in ps) can be measured.
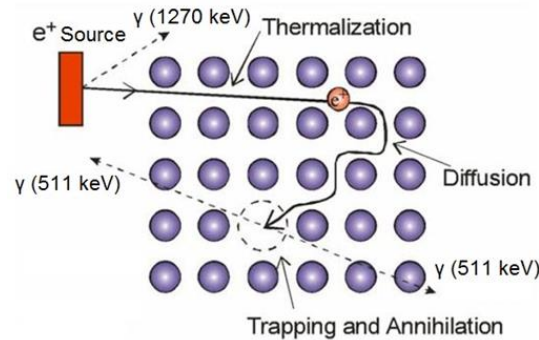
Figure 5: Scheme of positron annihilation in matter [1].

3.5.1.1. Measuring setup

Since we would like to keep the same measuring geometry for measurements of reference and irradiated samples, the same three detector setup is used for both types of materials. The measurement of irradiated materials has some difficulties compared to non-irradiated ones. Neutron-irradiated specimens must be measured with 3-detector setup apparatus (Figure 6) to compensate for a parasitic effect of γ photons emitted from unstable elements created by the neutron capture. It is mainly ^{60}Co, which during the decay emits two γ photons of energies 1174 keV and 1332 keV. These energies are very close to the energy of the start signal for PALS (1274 keV) and can be detected as a false start signal. In the case of a 3-detector setup, each annihilation event is accompanied by three γ photons – one with the energy of 1274 keV (birth of positron) and two with the energy of 511 keV (annihilation of positron), where a valid event is measured only when there are recorded both of 511 keV photons. Disadvantages, compared to a 2-detector setup, are a loss of an annihilation signal count rate and a consequent increase of a measurement time. The total uncertainty of the apparatus is ±2 ps, and FWHM (Full width at half maximum – resolution of the spectrometer, characterized by a Gaussian) is stable at our setup at about 175 ps.
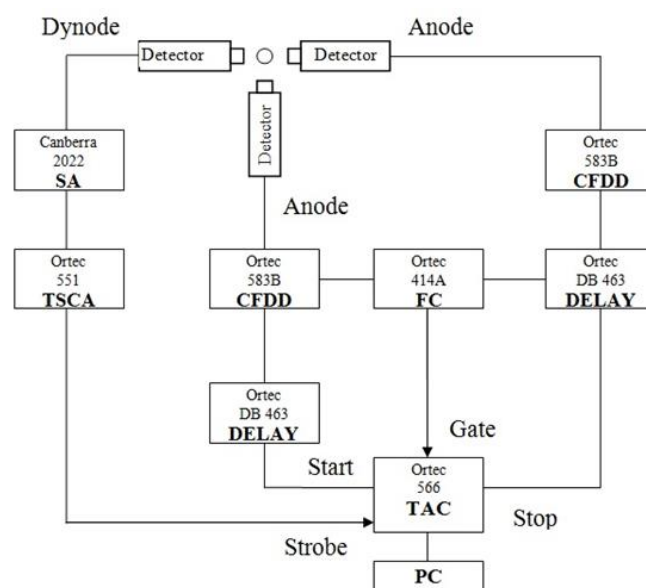
Figure 6: Scheme of 3-detector set-up for PALS measurements.

3.5.1.2. Trapping model

In a perfect defect-free crystal lattice, the positrons will diffuse in a layer ranging from 100 to 200 micrometers during their lifetimes [2]. For "ideal" iron (100% pure and defect-free structure), a total positron lifetime is, for example, 110 ps [3]. However, no real structure is perfect, and the value of the total lifetime (in this case, the so-called mean lifetime) is affected by defects, impurities, grid organization of a structure and chemical composition.

The mean lifetime can be divided into three or more lifetimes according to the properties of studied materials [4]:

i) first lifetime – a shorter value, which includes positron annihilation in defect-free zones and annihilation in some impurities. This lifetime is affected by evaluating software during calculations; therefore, an accurate physical meaning of this lifetime does not exist.

ii) second lifetime – a longer value characterizes the annihilation in the defects (see Figure 7).

iii) third lifetime – positron annihilation in air between the source and samples, so called in-flight annihilation [5].

Figure 7: Typical lifetimes for defects in matter [6].

Positrons are trapped in zones with lower atomic density, which is typical for vacancy defects, vacancy clusters, bubbles, voids or cavities. Dislocations can also attract positrons because lower local atomic density is present in front of the dislocations.

Although the open volume defect contains valence electrons of neighboring atoms, the total electron density and the atomic density are smaller. As a result, the positron lifetimes increase in view of a lower probability of annihilation.

On the ground of a change of annihilation conditions, different lifetimes describe different defect sizes; therefore, more types of defects can be observed in the structure. The behavior of positrons annihilated in samples can be described by two following rate equations [7]:

$$\frac{dP_b}{dt} + \lambda_b P_b + \kappa P_b = 0 \qquad (3.5.1)$$

$$\frac{dP_d}{dt} + \lambda_d P_d = \kappa P_b \tag{3.5.2}$$

Where P_b is probability that positron annihilated in the bulk, P_d – probability that positron annihilated in the defect, κ – trapping rate (s^{-1}), λ_b – annihilation rates in the bulk and λ_d is annihilation rates in the defect.

From the annihilation rates, positron lifetimes (τ_1, τ_2) can be derived [8].

$$\tau_1 = \frac{1}{(\lambda_b + \kappa)} \tag{3.5.3}$$

$$\tau_2 = \frac{1}{\lambda_d} \tag{3.5.4}$$

Two relative intensities, describing a percentage of positrons annihilated with a belonging lifetime, are written as follows:

$$I_1 = 1 - I_2 \tag{3.5.5}$$

$$I_2 = \frac{\kappa}{(\lambda_b - \lambda_d + \kappa)} \tag{3.5.6}$$

These equations characterize annihilation only in one type of defects, but it can be extended about more defects with different annihilation trapping rates.

The defect concentration can be calculated from values of the intensity according to equation [9]:

$$\kappa_i = \mu_i \cdot C_i \tag{3.5.7}$$

Where μ is the Specific trapping rate depending on the type of a defect and C_i is the defect concentration.

3.5.1.3. Data evaluation

The obtained spectrum (Figure 8) is evaluated with one or more exponential functions by an evaluating program. In the case of a perfect lattice, the spectrum is characterized by only one positron lifetime, and this value corresponds to the defect-free structure, so-called bulk. The bulk values for pure iron and chromium are around 110 ps. A higher value of the positron lifetime indicates defects, voids or formation of positronium. PALS is sensitive to changes in a defect concentration and defect size in samples before and after some change of a microstructure. When defects grow or increase their amount, also an average lifetime of positrons will increase– τ_{avg} . The average positron lifetime is calculated from measured data including only annihilations in the material: components τ_1 and τ_2 and considers the insities I_i of those components.

$$\tau_{avg} = \sum_{i=1}^{2} \tau_i . I_i \tag{3.5.8}$$

$$N(t) = \sum_{i=1}^{k+1} \frac{I_i}{\tau_i}\left(-\frac{t}{\tau_i}\right)$$

τ_1 - Material bulk
τ_2 - Defects or impurity
τ_3 - In flight annihilation
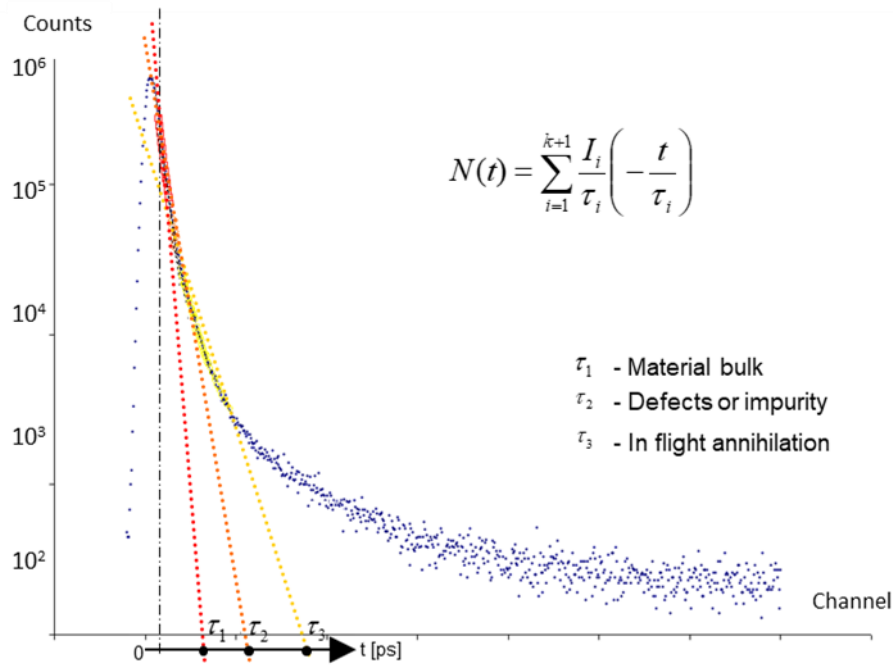
Figure 8: Typical spectra decomposition of the metal sample damaged by one type of a defect (impurity), where τ_i. is the lifetime of the component and I_i is is corresponding intensity [10].

A time resolution is determined by a parameter full-wide at half maximum (FWHM) obtained directly from the spectrum. FWHM is affected by settings of equipment and can be expressed by the following equation:

$$FWHM = 2\sigma_S \sqrt{\ln 2} \tag{3.5.9}$$

Where σ_s is the Standard deviation of Gaussian distribution function. The value of the FWHM parameter for all our measurements was close to 175 ps. The Fit Variant (reduction of χ^2) achieved value in range (1; 1.1).

The measured data (spectrum of positron lifetimes for one million annihilations – suitable statistics for an evaluation) is processed in the software LT-10 [11]. In the first step, the free-defect silicon is measured by PALS. The measurement is evaluated, considering the known lifetimes of positrons in pure silicon (222 ps) and kapton (382 ps), to obtain a source contribution for the measured spectra (mostly ~ 20% of annihilations). Annihilations with the highest lifetime and low intensity are from in-flight annihilations. Fitting the silicon in LT-10 is based on a selection of the measured data, which we want to process and put the known lifetimes to individual components. If the selected data are chosen correctly, then ''fit's variance'' will be between 0.9 and 1.1 (the error of evaluation is below 0.1%). In this case, one can proceed to the processing of the measured specimen. The processing area of the studied material remains the same as for the silicon. The calculated contribution of the source (containing annihilations in the source, kapton, air and holder) is moved to a ''Source'' memory, and then parameters of the Gaussian function are fixed. Afterwards, several expected components with their estimated positron lifetimes are entered. The following calculation provides results containing the lifetime of positrons and their intensity for the

expected components – usually three components such as annihilation in bulk (basic material – mostly the lowest lifetime with the greatest intensity), air (or so-called in-flight annihilation – the greatest lifetime and intensity of level about 1-2%) and defects. The lifetime of annihilations in defects informs about the type and concentration of vacancy-type defects in the crystal lattice [12].

The sensitivity of PALS is relatively very high, with an ability to recognize defects which cannot be seen by an electron microscope, which provides a unique type of information for microstructural studies in selected materials, for example, before and after an external treatment (irradiation, annealing, etc.). The basic principle of the evaluation is to compare the results before and after treatment, where this ratio can be used to estimate the degree of damage in the studied materials accurately.

3.5.2. (Coincidence) Doppler broadening spectroscopy ((C)DBS)

A measurement of Doppler broadening of positron annihilation spectra is one of the momentum-based techniques, where the momentum of the electron-positron pair is transferred to the photon pair during the annihilation process. The motion of the annihilating pair causes a Doppler shift ΔE of the annihilation energy of 511 keV, which can be calculated approximately as [13]:

$$\Delta E_\gamma = \frac{1}{2} c \, p_l \tag{3.5.10}$$

Where p_l stands for the longitudinal component of the pair in the direction of the annihilation gamma emission and c is light velocity in vacuum.

This causes the 511 keV annihilation line's broadening, as seen in Figure 9. The measuring of the positron annihilation energy with energy deviations 511 keV ± ΔEγ makes possible to characterize the material microstructure at atomic scale due to the non-zero momentum of the electron-positron pairs modifies the features of the annihilation radiation [14].
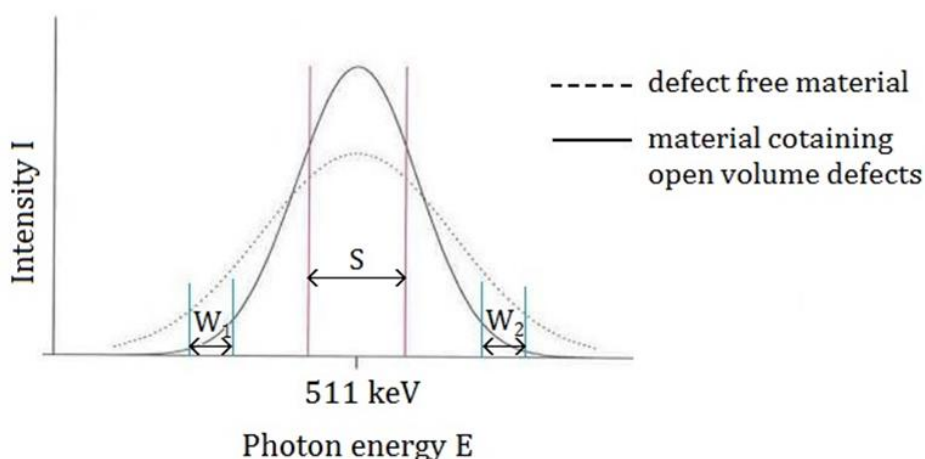
Figure 9: Doppler broadening of positron annihilation spectra with two plots: defect free material and material containing open volume defects; and schematic representation of S and W parameter of spectra [14].

DBS is a progressive non-destructive technique which can be used to characterize open volume defects at the nanoscale and their chemical environment. Since the energy deviations, ΔE_γ from 511 keV are dominated by the moment of the electrons due to the relative velocities of the positron and electron before the annihilation, a lineshape of the DBS carries the information about the material where the annihilation has occurred. Annihilations in some defect sites in the material will bring a "fingerprint" of the defect structure in the form of ΔE_γ. Thus, changes in defect types and/or defect concentration can be studied by means of monitoring of DBS lineshape changes.

Coincidence Doppler broadening spectroscopy (CDBS) is one of the DBS techniques, which is based on the use of a two-detector set-up (Figure 10) in order to obtain a second annihilation quantum in a coincidence of annihilation events with core electrons. This results in an improvement of the peak-to-background ratio by 3-4 orders of magnitude (Figure 10). This way, it is possible to detect high-momentum annihilations with the core electrons [14]. Then, the measured background can be effectively eliminated, which leads to a more precise evaluation of the spectra. We know that a sum of both energies is 1022 keV, and when, for instance, 515 keV is detected in one detector, the second detector shows 507 keV. Thus, the electron energy is detected twice. This means that the resolution of the system is improved by a factor of 0.707. On the other side, there are also some disadvantages as well, for instance, low efficiency and a more complicated setup [15].
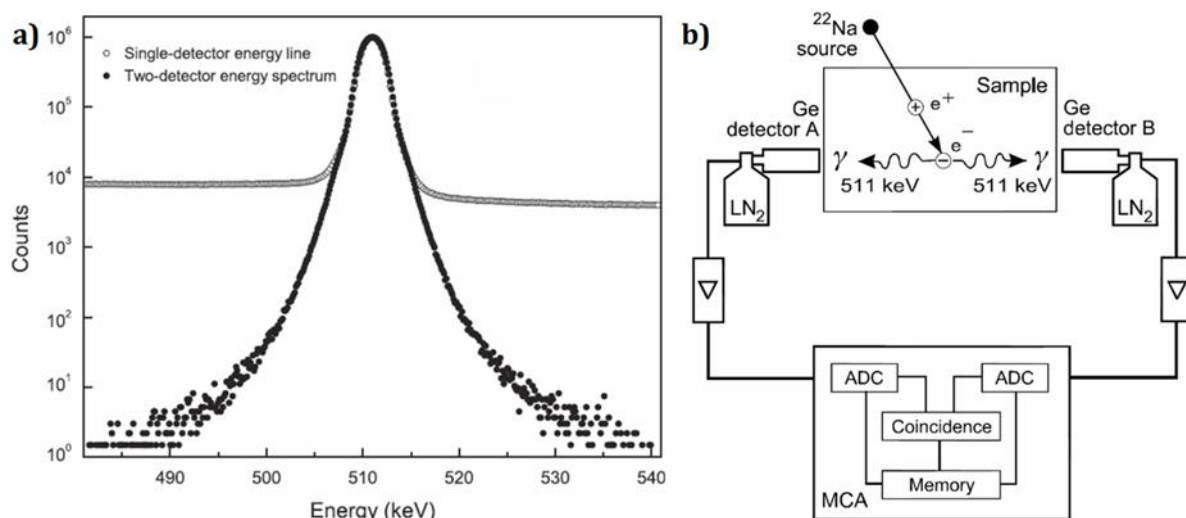
Figure 10: a) Distribution of energy spectra for using of one and two-detector measurements; b) CDBS set-up [16].

3.5.2.1.   Date evaluation

The motion of positron-electron pairs prior to annihilation causes Doppler broadening of the photopeak in the measured energy spectrum of the annihilation photons, which can be characterized by the lineshape parameter S. The S is higher for positrons trapped at, and annihilated in, open-volume defects (corresponds to positron annihilation with valence

electrons) and it is sensitive to size and concentration of vacancy-like defects. The W parameter ("wing" or core annihilation parameter) is taken at the high-momentum region away from the centre. Since the positron annihilation takes place with core electrons, the W parameter probes the chemical surrounding of the annihilation site. The parameters S and W are calculated as the normalized area of the curve in a fixed energy interval (Fig. 5.5.8). The correlation between both parameters varies for different defect types [17].
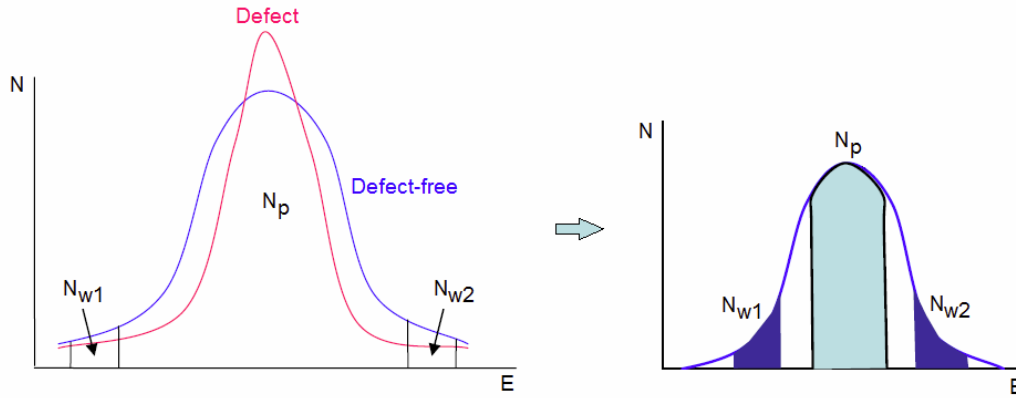
Figure 11: Doppler broadening spectra for S and W parameters determination [18].

The Figure 11 shows a short procedure of the S and W estimation, where N_p is number of counts near the peak are and N_{w1}, N_{w2} represent number of counts in wings areas. Following the equations (3.5.11-3.5.13) the parameters values can be calculated:

$$S = \frac{N_p}{N_{total}} \tag{3.5.11}$$

$$S_{defect} > S_{defect\,free} \tag{3.5.12}$$

$$W = \frac{N_{w1} + N_{w2}}{N_{total}} \tag{3.5.13}$$

The determination of S and W parameters and ratio curves comparison was, in this project, performed by CDBtools3 software developed at INPE by Martin Petriska [19].

4. Results and Discussion

4.1. Optical Microscopy

The first study of the materials has been done with optical microscopy and the results obtained at CIEMAT are shown in Figure 12. The materials have been etched with Vilella's reagent to reveal the bainitic microstructure. At this scale a refinement of the microstructure in the case of B, C and G model steels has been observed.
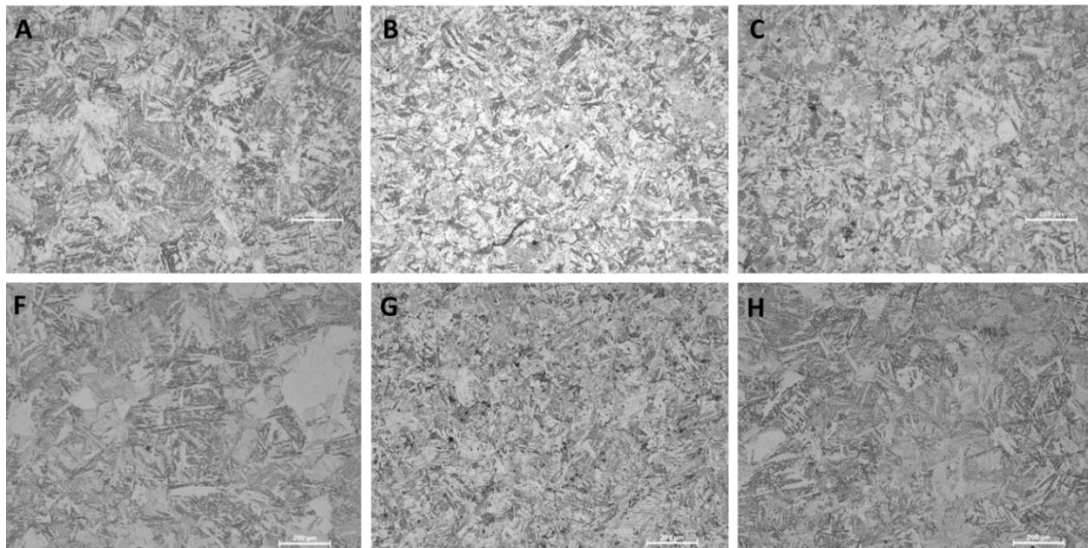
Figure 12: Optical images of the model steels

A deeper characterization of the microstructure by means of optical microscopy of model alloys have been carried out at VTT. The microstructures of Model steels A, B, C, F, G and H were characterized from three orientations. Cross-sections of Model steels A, B and C were cut from tested fracture toughness specimens. The selected specimens were AC26, BC26 and CC26. Orientations x, y and z can be seen in Figure 13. The sizes of the cross-sections were $8*7.5 \text{ mm}^2$ (x) $8*5 \text{ mm}^2$ (y) and $5*7.5 \text{ mm}^2$ (z).

Cross-sections of Model steels F, G and H were cut from $2*5*10 \text{ mm}^3$ plates. The sizes of cross-sections were $2*7.5 \text{ mm}^2$ (x), $2*5 \text{ mm}^2$ (y) and $2.3*7.5 \text{ mm}^2$ (z).
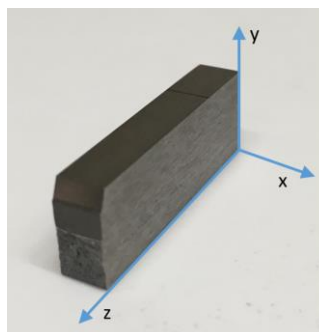
Figure 13. A tested fracture toughness specimen with determined orientations x, y and z.

Model steel A

The microstructure of Model steel A is mainly upper bainite. Small islands of grain boundary ferrite and polygonal ferrite were observed. The microstructures of orientations x, y and z are shown in Figure 14. All the orientations show similar microstructure and, therefore, the rolling direction is not evident.

Ghost lines are not present in the microstructure. Ghost lines are also known as segregation lines, which in the microstructure consists of parallel stripe-like areas, with slightly darker appearance. Ghost lines are due to macrosegregation from the manufacturing of the material. Impurities such as S and P and alloying elements such as C and Mn are known to segregate to

ghost lines. Ghost lines can be seen in base material but they are also visible in fine-grained heat-affected zone, which means that temperature has not been high enough to affect the macrosegregation. Ghost lines can have higher hardenability than non-segregated areas of the base material. Also, martensite may be present at the ghost lines.
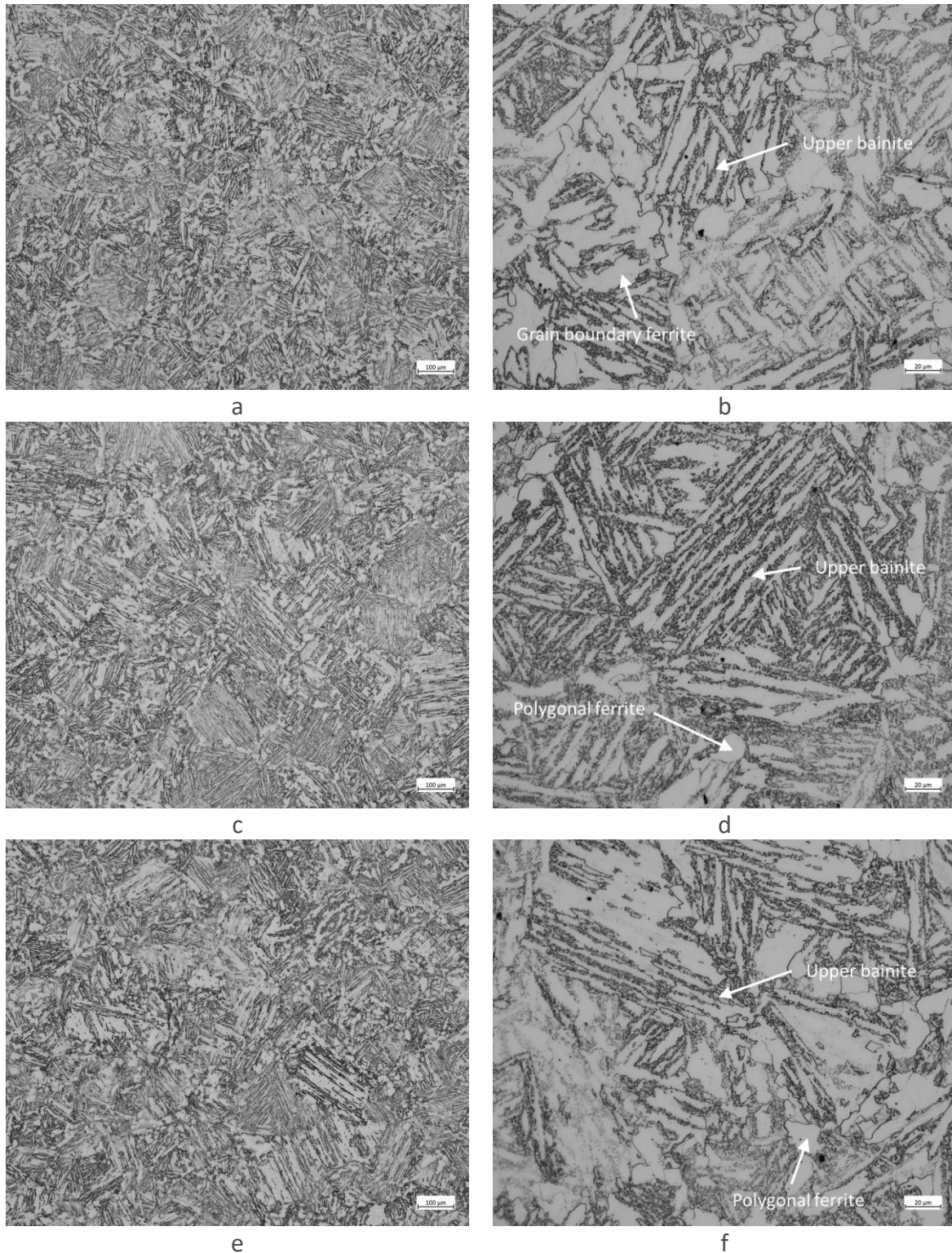
Figure 14. The microstructure of Model steel A is mainly upper bainite. Small islands of grain boundary ferrite and polygonal ferrite is present. The orientations are (a, b) x, (c, d) y and (e, f) z.

Model steel B

The microstructure of Model steel B consists of lower bainite and upper bainite. Lower bainite is the dominant microstructure. The microstructures of orientations x, y and z are shown in Figure 15. No ghost lines are present in the microstructure. All the orientations show similar microstructure and the rolling direction cannot be determined.

Increasing Ni-content increases the hardenability by forming finer microstructure and needle-like structure. Increase in Ni-content decreases the start and final temperatures of bainite and martensite phase transformation. This could explain why Model steel B has also lower bainite in the microstructure but Model steel A has not.

a

b

c

d

e   f
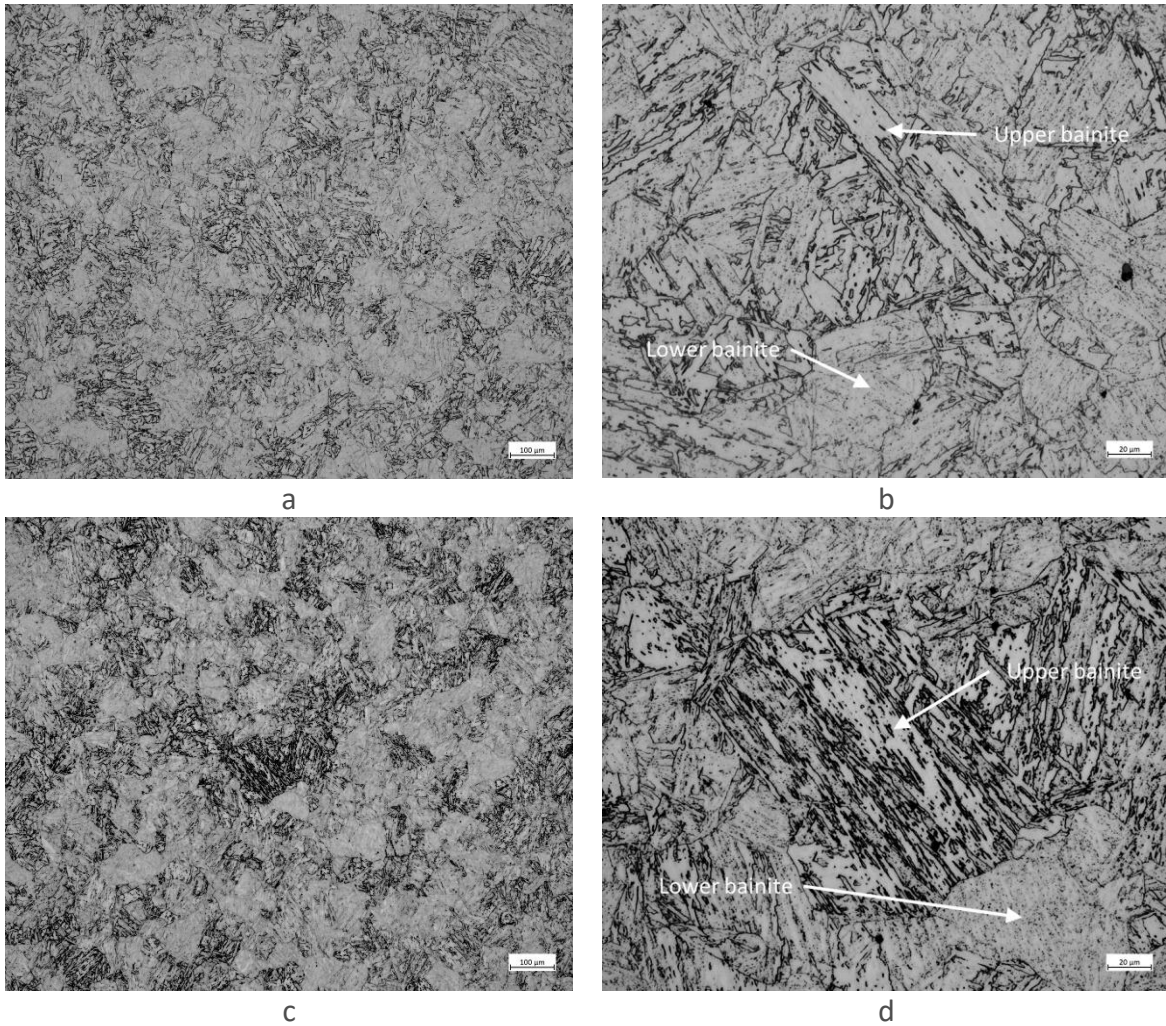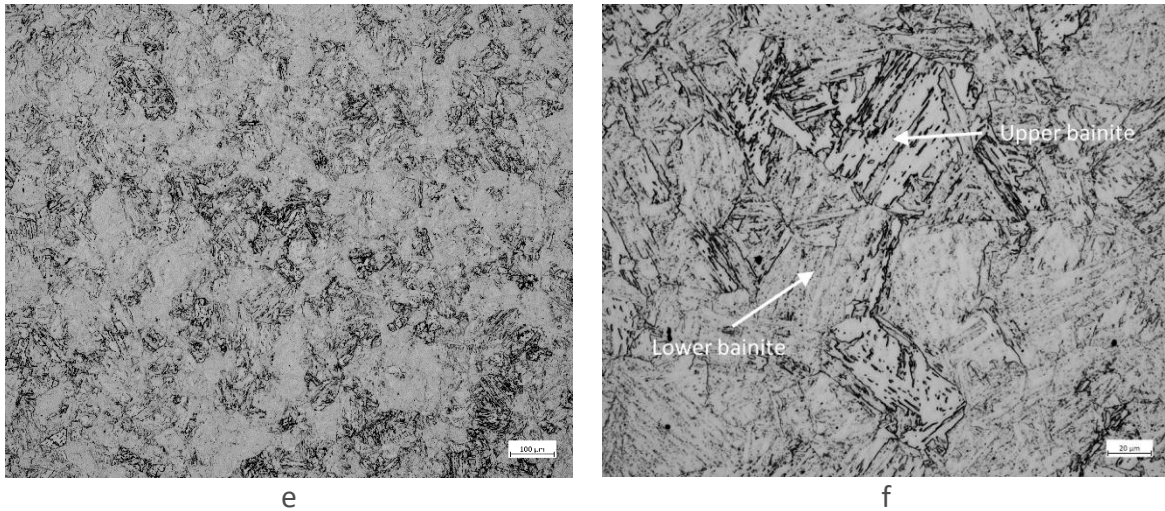
Figure 15. The microstructure of Model steel B consists of lower bainite and upper bainite. The orientations are (a, b) x, (c, d) y and (e, f) z.

Model steel C

The microstructure of Model steel C is quite similar as Model steel B. The microstructure consists of lower bainite and upper bainite. Lower bainite is the dominant microstructure. The microstructures of orientations x, y and z are shown in Figure 16. No ghost lines are present in the microstructure. All the orientations show similar microstructure and the rolling direction cannot be determined.

a   b
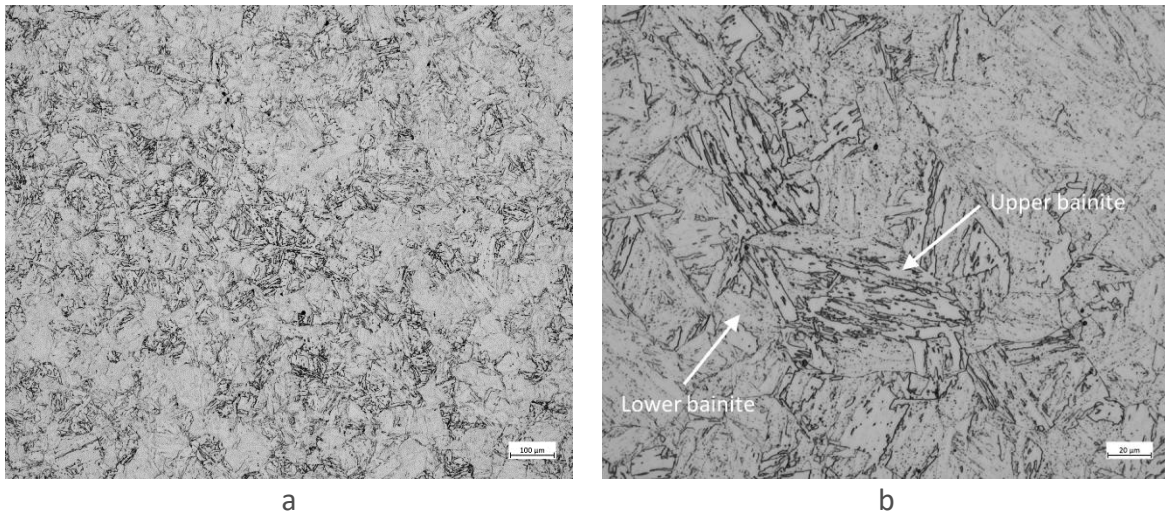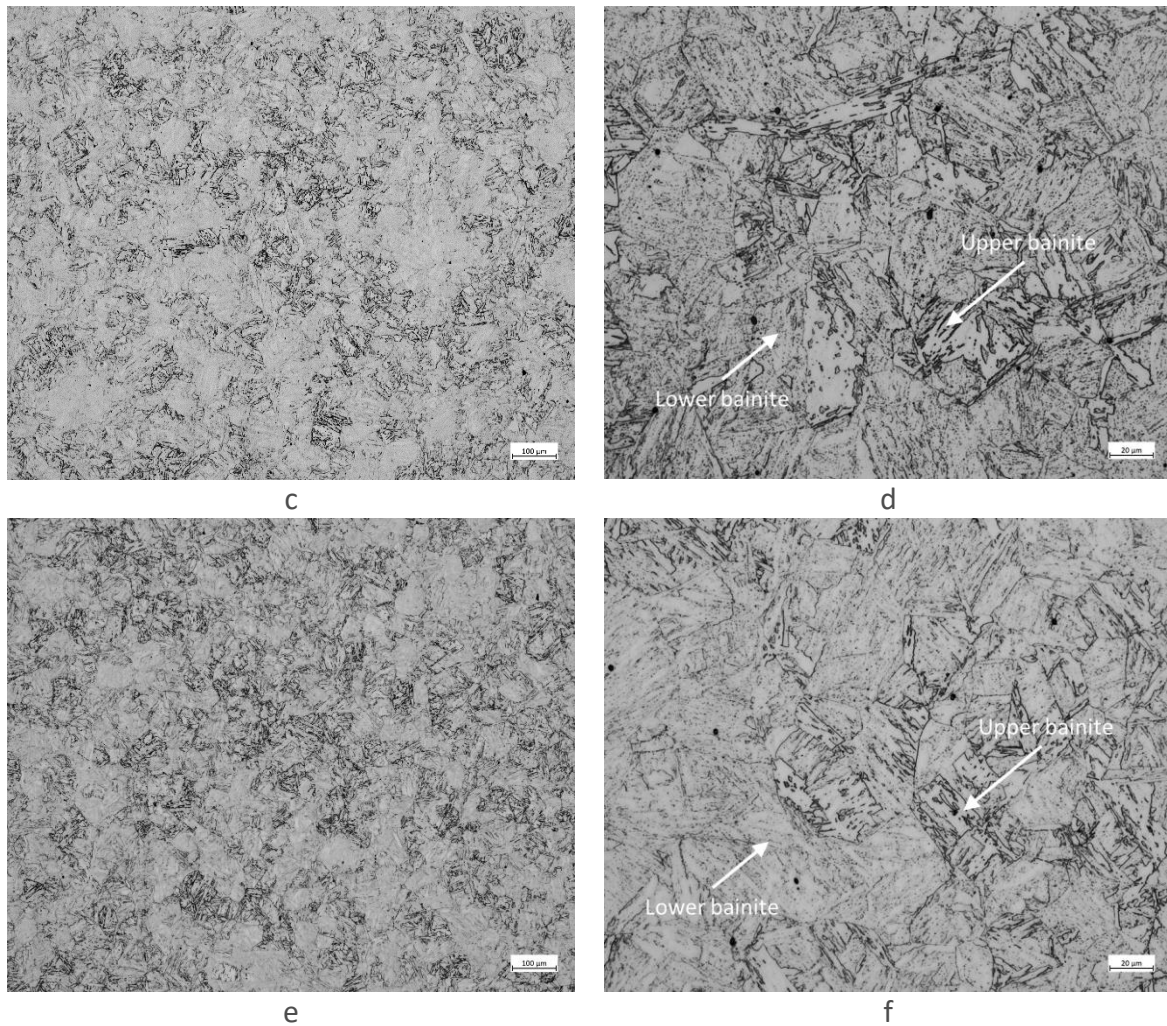
Figure 16. The microstructure of Model steel C consists of lower bainite and upper bainite. The orientations are (a, b) x, (c, d) y and (e, f) z.

Model steel F

Lower bainite is the dominant microstructure in Model steel F. Upper bainite is also present. The microstructures of orientations x, y and z are shown in Figure 17. The laths of upper bainite are long due to larger prior austenite grain size, which allows lath to grow.

Weak ghost lines are present in orientations y and z, see Figure 18. Orientation x has no ghost lines. This also means that rolling direction can be concluded. Orientation x is L-T. However, orientations y and z are very similar and L-S and T-S cannot be determined. Elongated MnSs in the same direction as the ghost lines can be seen.
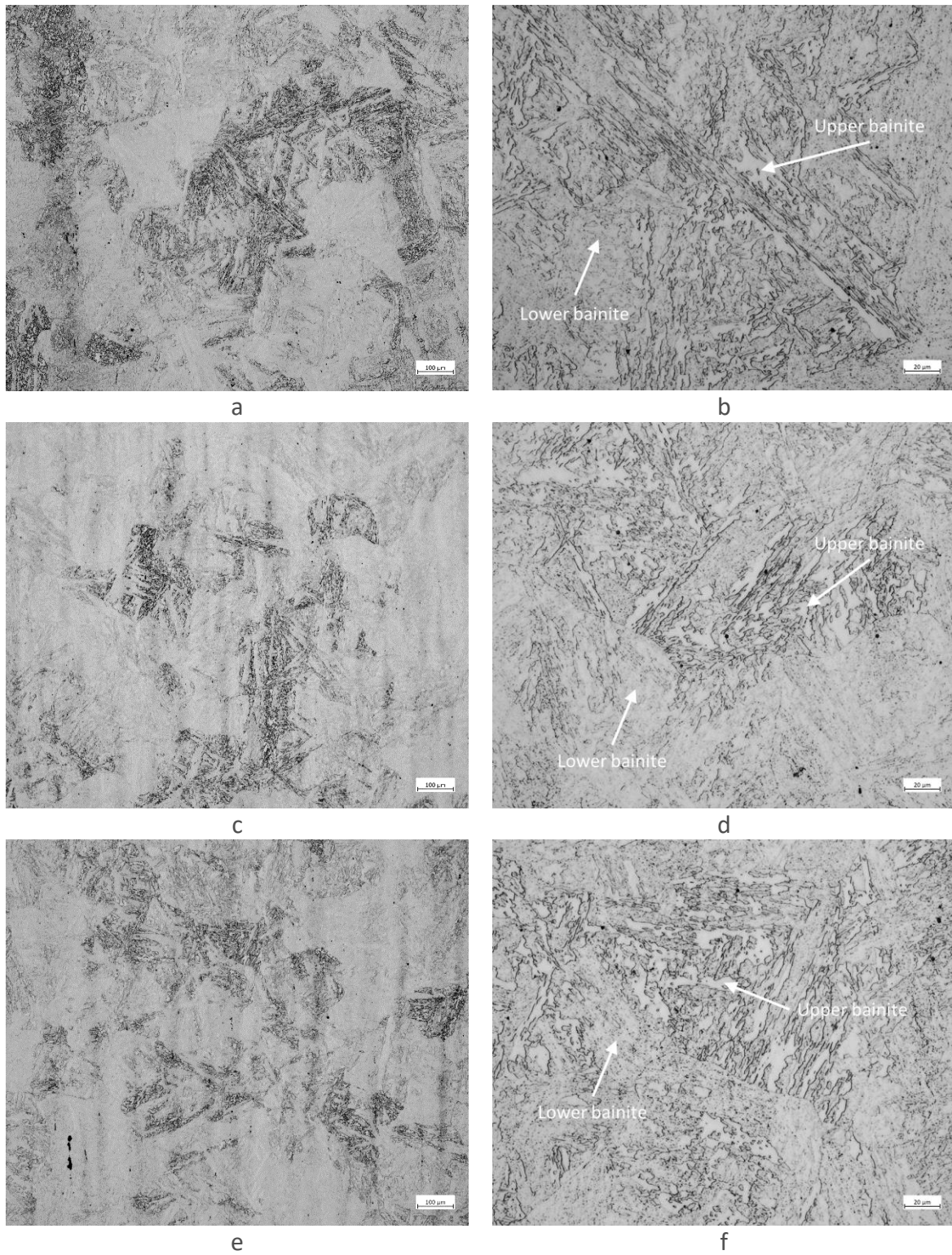
Figure 17. The microstructure of Model steel F consists of lower bainite and upper bainite. The orientations are (a, b) x, (c, d) y and (e, f) z. Weak ghost lines can be seen in orientations y and z.
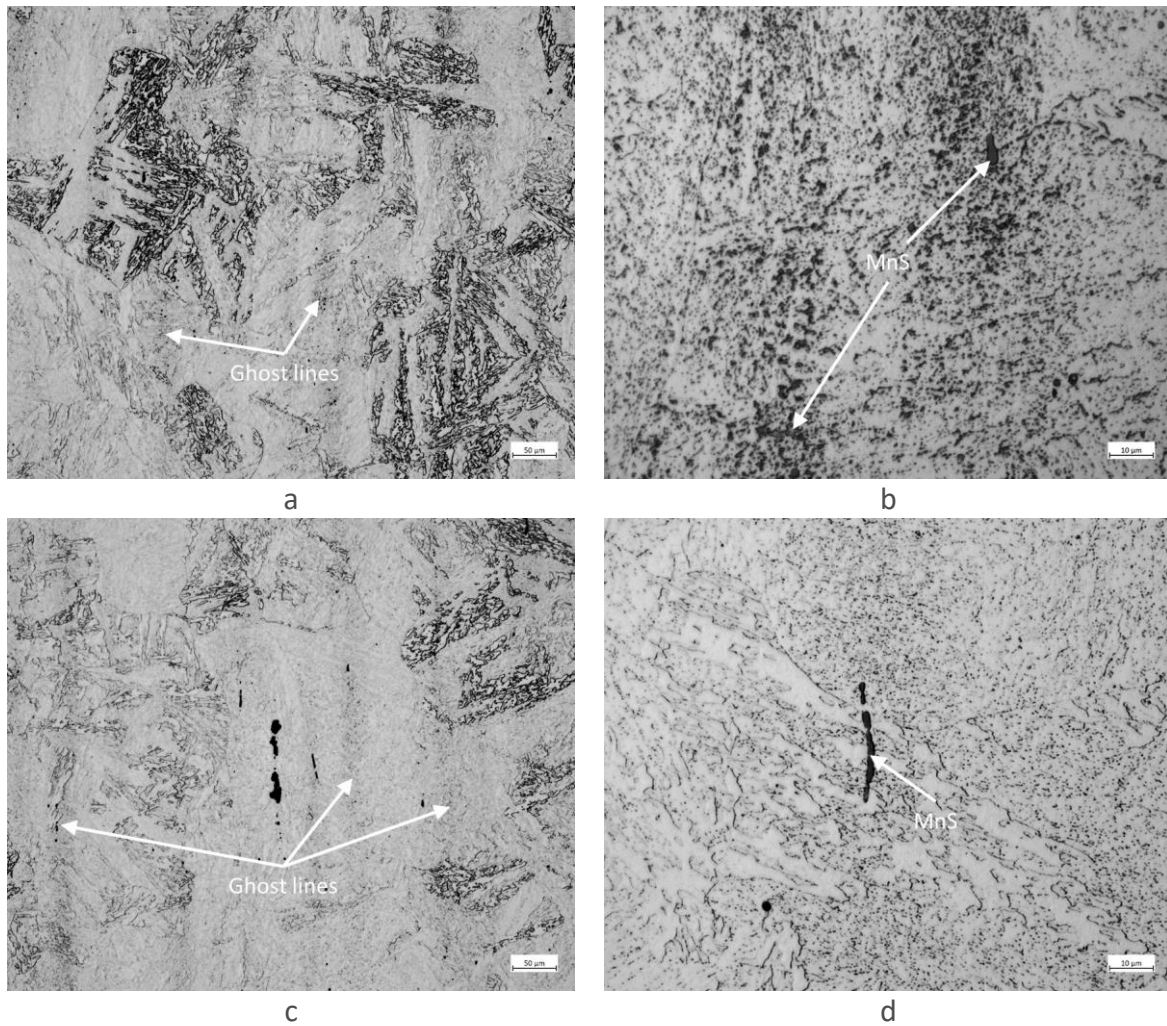
Figure 18. Weak ghost lines in orientations (a, b) y and (c, d) z in Model steel F. Elongated MnSs are present in the ghost lines.

Model steel G

The distribution of lower bainite and upper bainite is quite even in the microstructure of Model steel G, see Figure 19. The grain size of prior austenite is smaller if compared to Model steel F and the laths of upper bainite are shorter. Very weak ghost lines may be seen in orientation z, which would suggest similar rolling direction as in Model steel F.
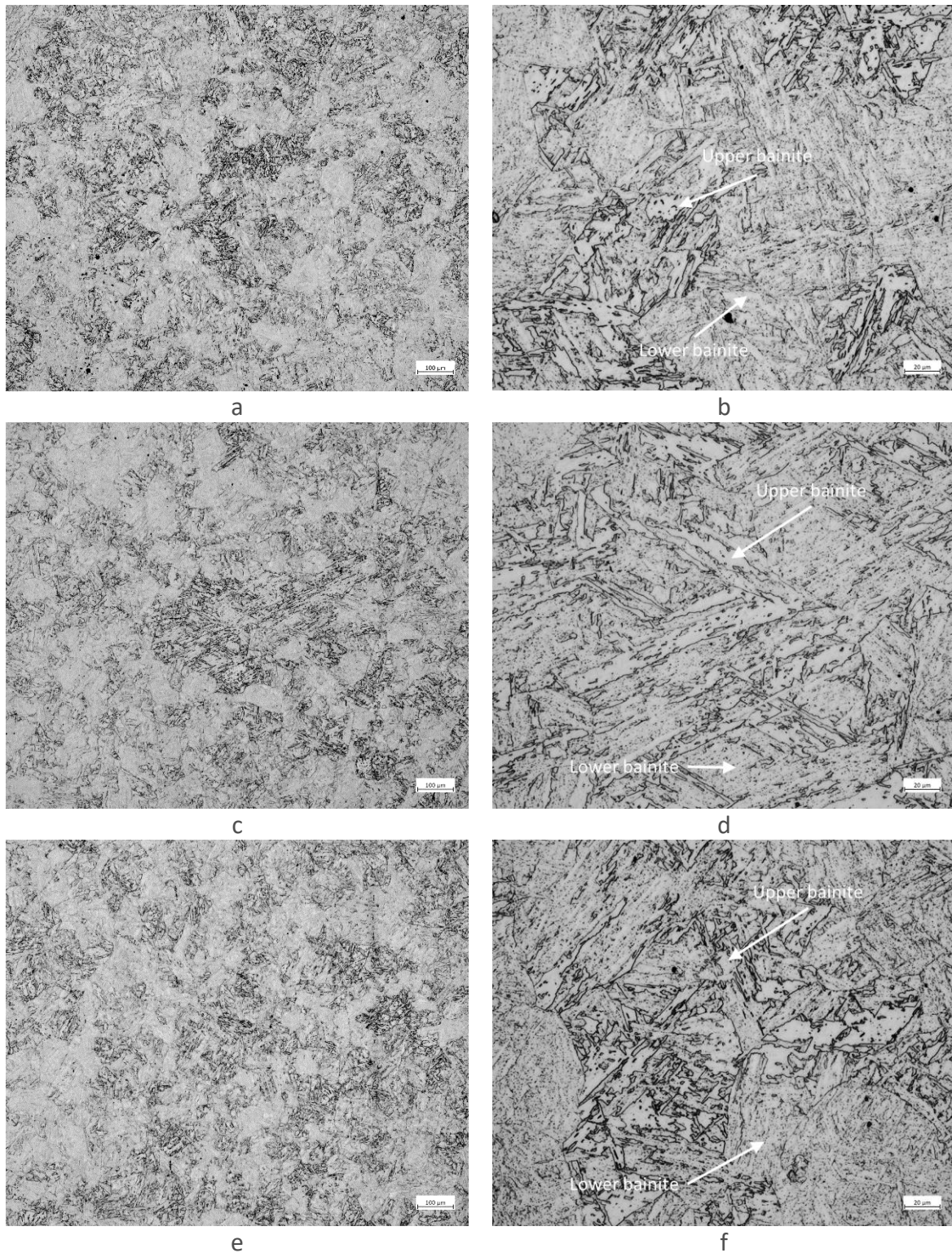
Figure 19. The microstructure of Model steel G consists of lower bainite and upper bainite. The orientations are (a, b) x, (c, d) y and (e, f) z.

Model steel H

Similar to Model steel G lower bainite and upper bainite are quite evenly distributed in the microstructure of Model steel H. The microstructure is presented in Figure 20. The prior austenite grain size is large and the laths of upper bainite are long.

Weak ghost lines are present in orientations y and z, shown in Figure 21. The appearance of orientations is the same as in Model steel F and orientation x, which has no ghost lines, is L-T. Orientations y and z are very similar and L-S and T-S cannot be determined. Elongated MnSs can be seen in the ghost lines.
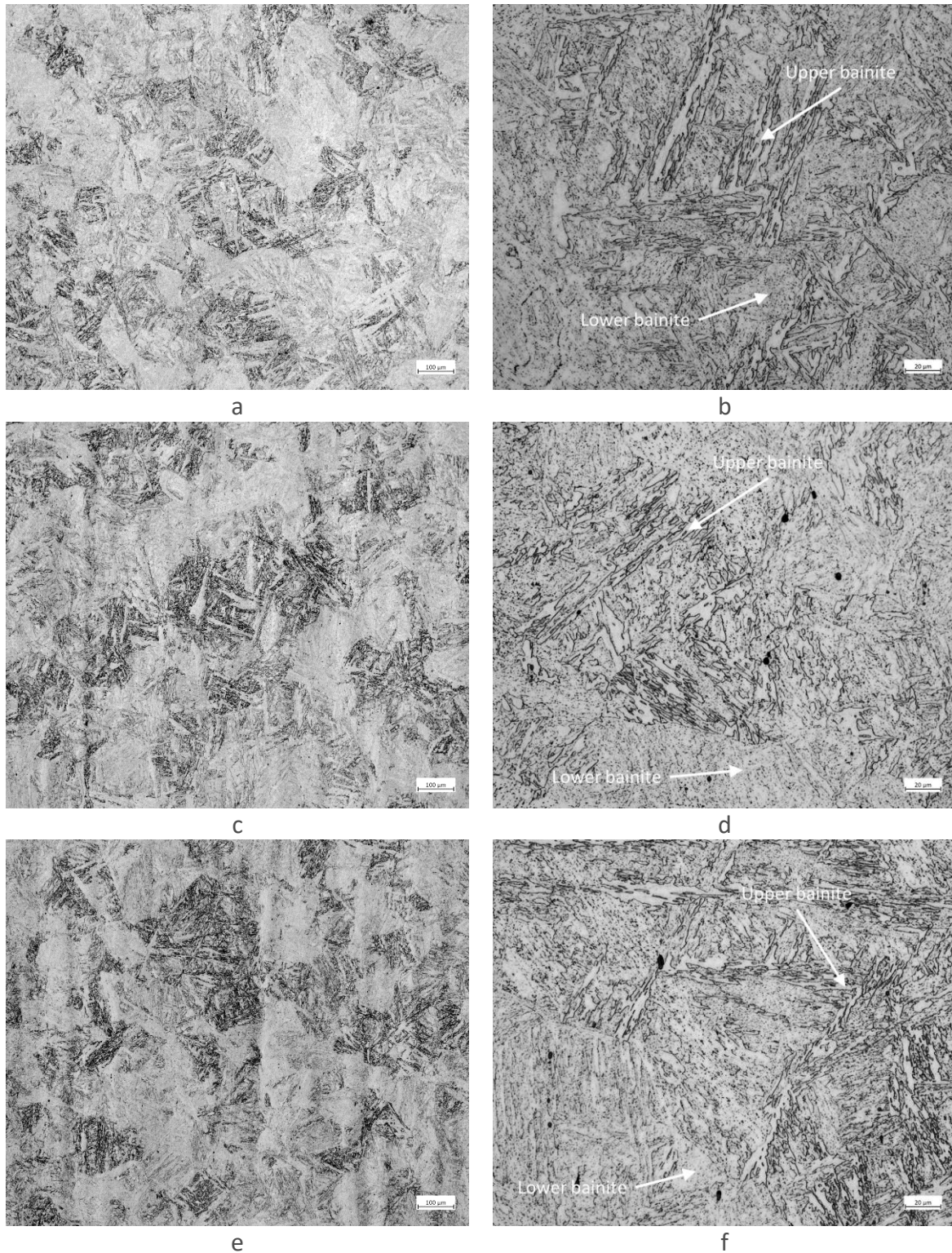
Figure 20. The microstructure of Model steel H consists of lower bainite and upper bainite. The orientations are (a, b) x, (c, d) y and (e, f) z. Weak ghost lines can be seen in orientations y and z.
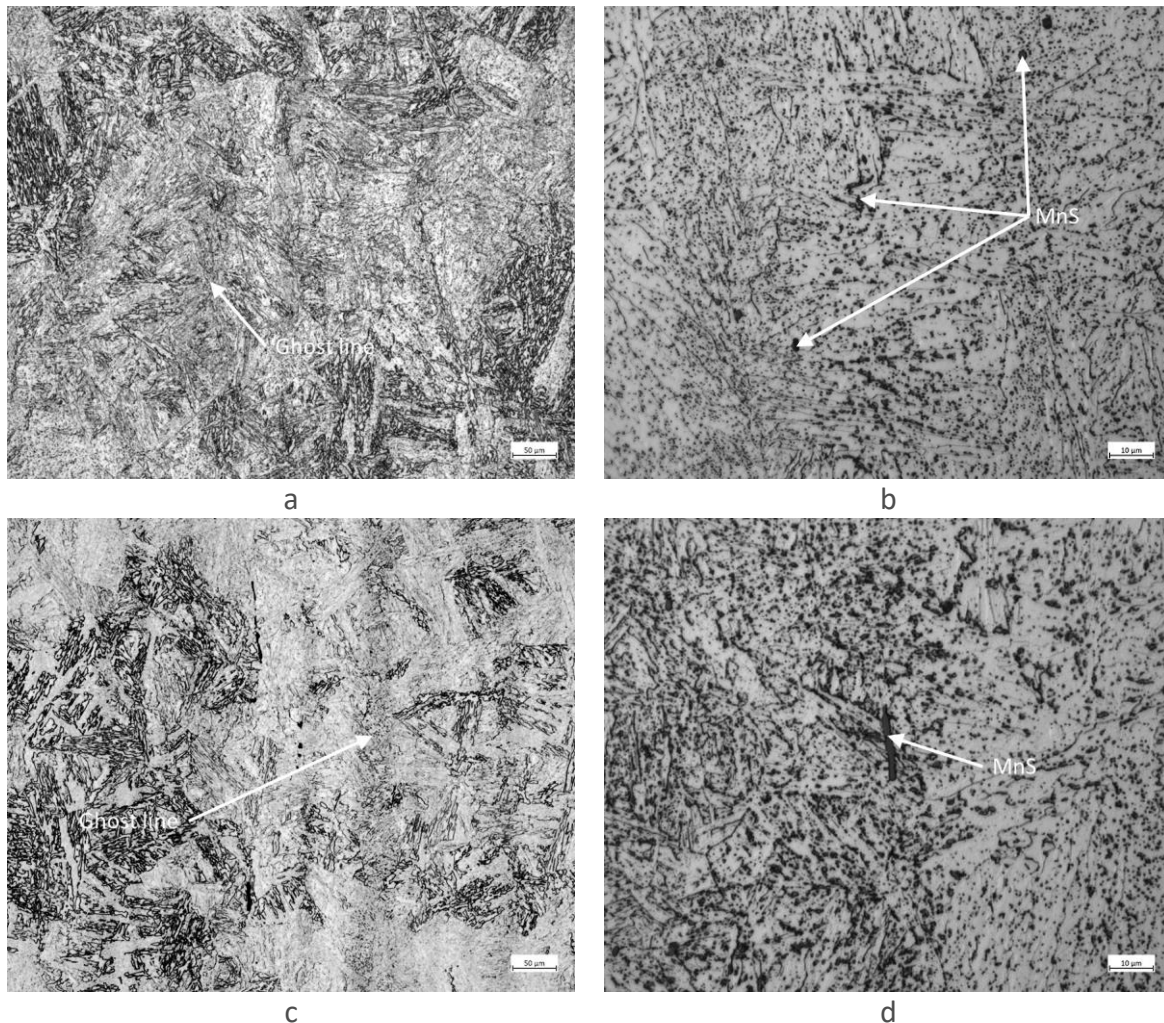
Figure 21. Weak ghost lines in orientations (a, b) y and (c, d) z in Model steel H. Elongated MnSs are present in the ghost lines.

4.1.1. Hardness

A Struers Durascan 80 hardness tester was used for HV10 hardness measurements. Hardness was measured from specimens AC26, BC26, CC26, FC21, GC21 and HC21 from three orientations. The results are presented in Table 4.

Typically, the increase of Ni-content increases hardenability. Model steel A has very low Ni-content but higher hardness than that of Model steels B and C. In addition to Ni, other elements like C, Mn, Cr and Mo also increases hardenability. Model steel A has slightly higher contents of Mn, Cr and Mo compared to model steels B and C, which may explain the higher hardness of Model steel A. The influence of increasing Ni-content from 1% to 2% on hardness cannot be seen.

Model steels F and H are showing similar hardness. The main differences in the chemical composition are lower Ni- and Si-contents and higher Mn- and Cr-contents in Model steel F compared to Model steel H. Model steel G has lower Si-content and higher Mn-content

compared to Model steel H. Cr-, Ni- and Mo-contents are similar, however, the hardness of Model steel G is higher. This could be explained by smaller grain size of Model steel G.

Specimen	Orientation	HV10	No. of indentations
AC26	x	230 ± 3	36
AC26	y	248 ± 5	24
AC26	z	247 ± 5	24
BC26	x	213 ± 2	36
BC26	y	214 ± 2	24
BC26	z	213 ± 2	24
CC26	x	208 ± 2	36
CC26	y	214 ± 2	24
CC26	z	213 ± 2	24
FC21	x	202 ± 3	6
FC21	y	203 ± 2	4
FC21	z	204 ± 1	6
GC21	x	215 ± 1	6
GC21	y	216 ± 2	4
GC21	z	217 ± 1	6
HC21	x	201 ± 2	6
HC21	y	199 ± 1	4
HC21	z	201 ± 2	6

Table 4. HV10 Hardness and number of indentations of specimens AC26, BC26, CC26, FC21, GC21 and HC21 measured from three orientations (x, y, z).

4.2. Scanning Electron Microscopy

The microstructure of the six model steels have been studied by SEM at CIEMAT previously to (S)TEM analysis to have a general overview of the microstructure and thus validate TEM results according to the available transparent region to electrons in each particular case.

Figure 22 shows SE images of the materials at different magnifications. At lower magnification the only difference observed is a refinement of the microstructure in the case of B, C and G materials that was previously reported in the OM results, but there are not differences in the chemical composition shown in Table 2 that can explain this refinement. Another difference observed is the microstructure of A model steel where there are ferritic grains islands along with bainitic laths. In this case, the difference can be related with the absence of Ni and a low amount Mn. Both are gamma stabilizers, so their absence promotes the presence of alpha phase. The volume fraction of ferritic grains has been measured in different representative areas of the material, being the mean value (13±1) %. As regards precipitates, in the detail shown for each material, coarser precipitates in general appears aligned at grain boundaries and smaller ones homogeneously distributed within grains. In the case of A model steel the

volume fraction of coarse precipitates placed at grain boundaries seems to be lower compared with the rest model steels.
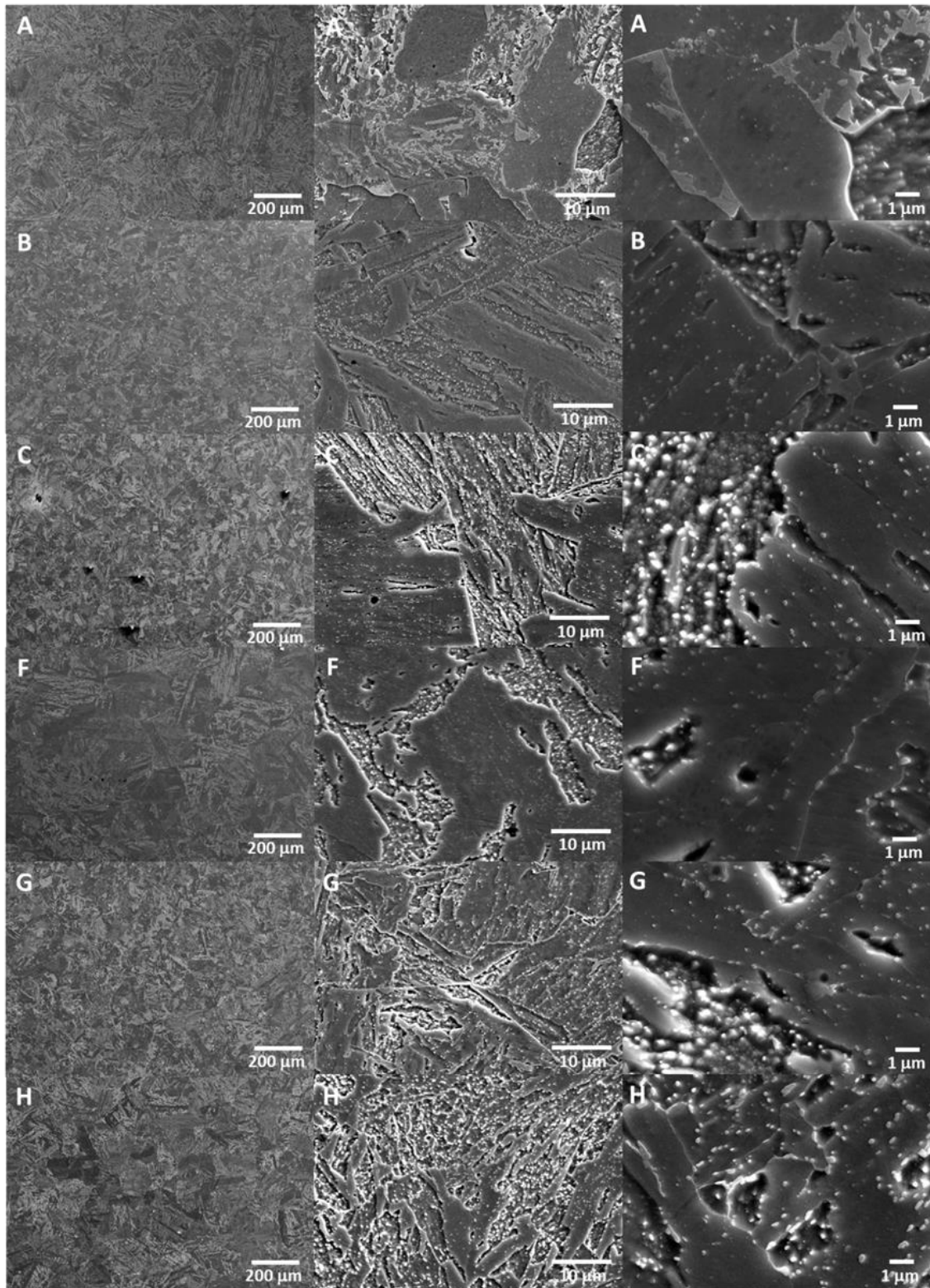
Figure 22: Secondary electron images of A, B, C, F, G and H model steels at different magnifications.

Quantification of precipitates has been carried out employing at least 10 images of random areas for each material and using the software JMicrovision. Only precipitates with a size above 10 nm have been measured since below this value were not easy to obtain a proper measure. Therefore, this quantification includes coarse carbides and small vanadium precipitates identified by EDS. The results are shown in the charts of Figure 23 and are summarized in Table 5. The mean size of precipitates is slightly smaller for G model steel with a higher density of precipitates. Lower densities were obtained for A and C model steels. In all the materials, excluding A model steel, it is possible to distinguish two peaks that correspond to families of precipitates with different sizes. But only in the case of C model steel, it was possible to split both families in the graph.
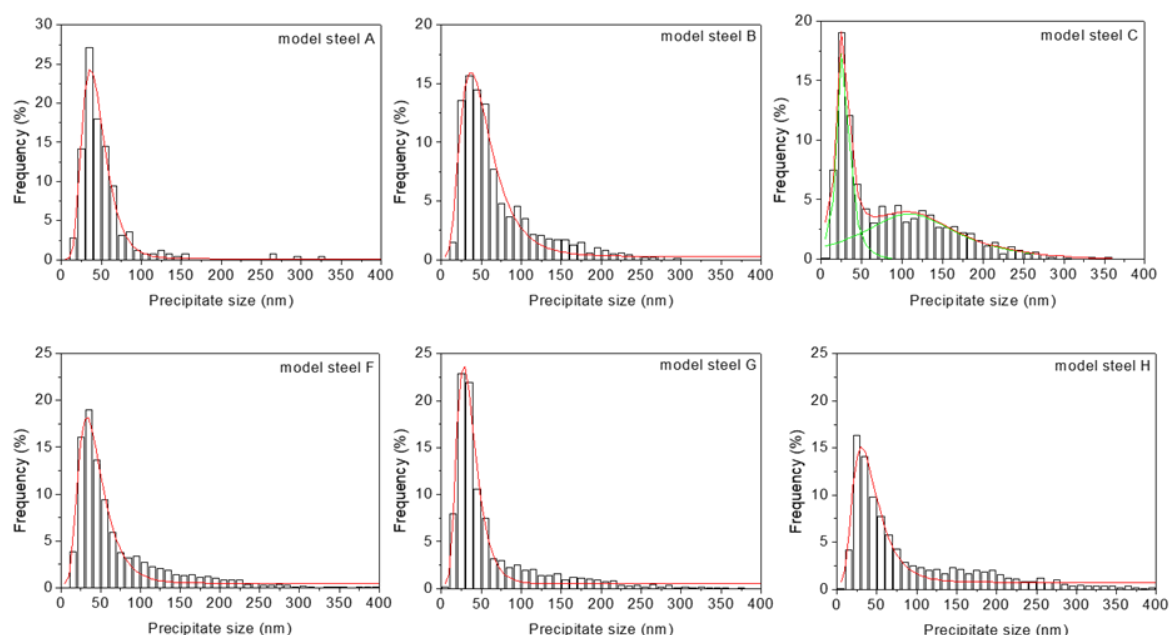
Figure 23: Precipitate size evolution of A, B, C, F, G and H model steels.

Model steel	Mean size* (nm)	Density (10^{12} m^{-2})
A	42±1	4±2
B	48±1	9±3
C	28±1 - 109±7	4±1
F	40±1	6±2
G	33±1	12±2
H	39±2	7±1

*minimum size corresponds to 10 nm

Table 5: Precipitates size and density of A, B, C, F, G and H model steels.

The results of HZDR regarding SEM study for the 6 studied model alloys (A, B, C, F, G and H) are shown in Figure 24. While model alloys B, C, F, G and H exhibit a typical lath bainite structure, in model alloy A there appear to be enclosed areas that resemble ferrite islands.
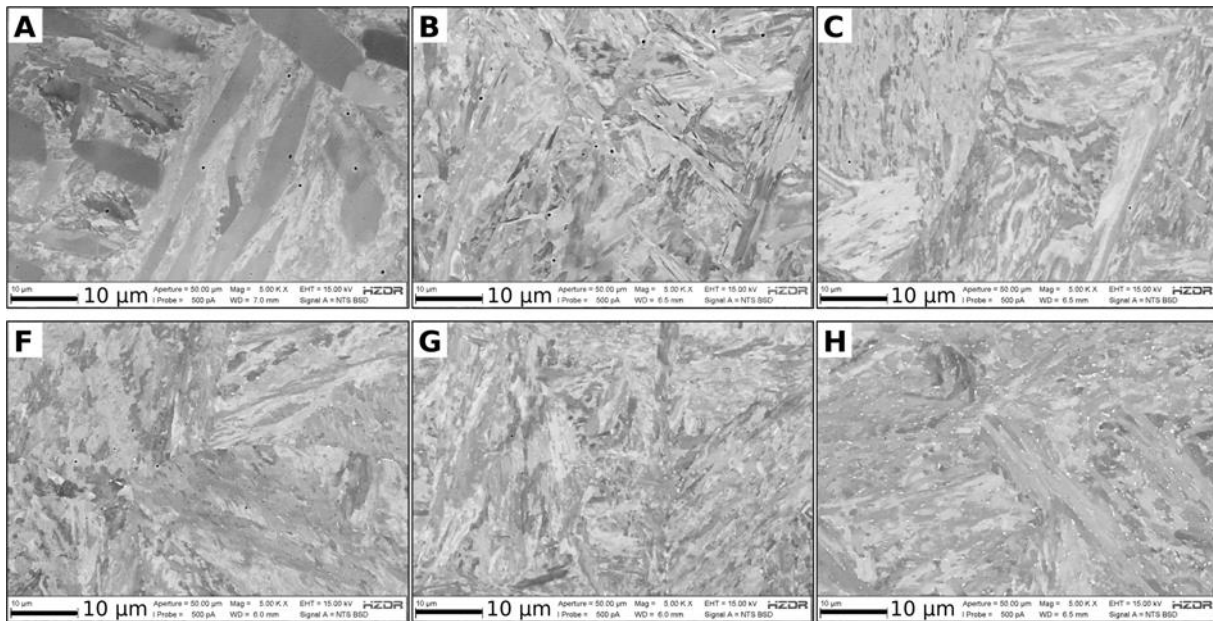
Figure 24: Representative BSE micrographs of model alloys A, B, C, F, G and H.

4.2.1. EBSD results of A, B, C, F, G and H model steels

For sake of a better general overview, the EBSD mappings presented in Figure 25 to Figure 27 show only a subset (one quarter) of the original mapping dimensions. The summary of the main results is provided in Table 6.
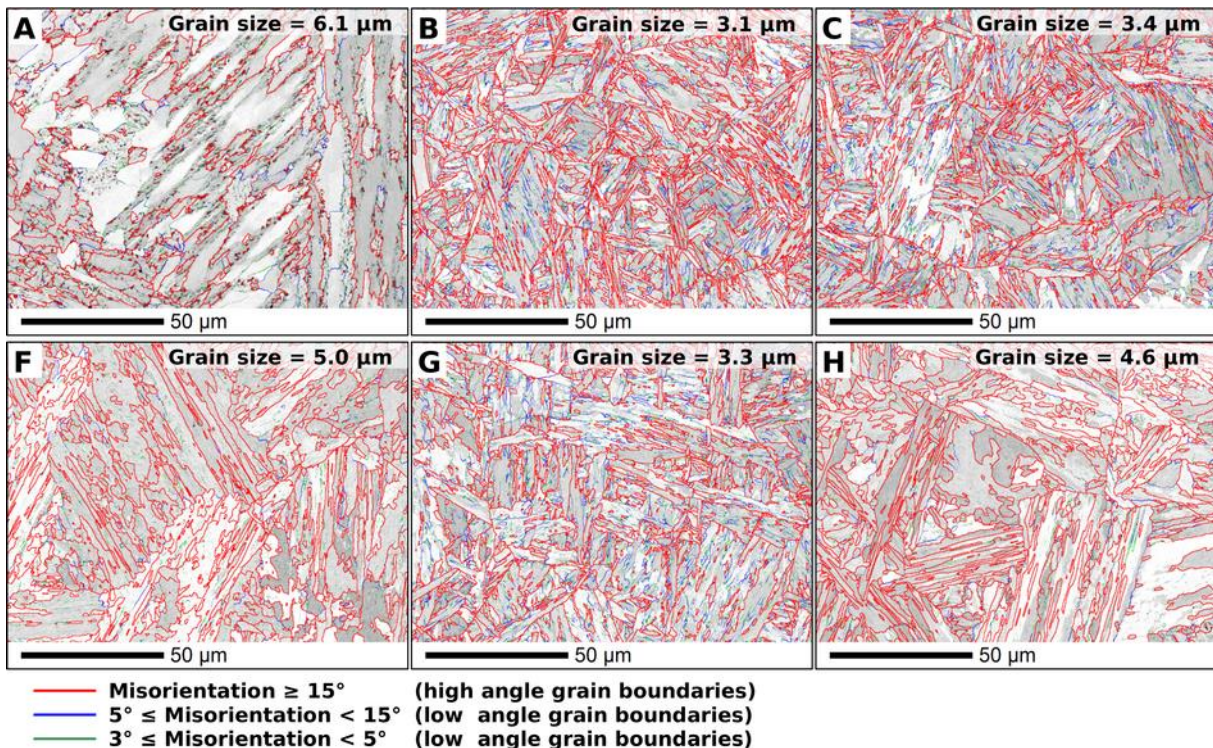
Figure 25: EBSD mappings demonstrating the grain boundaries.
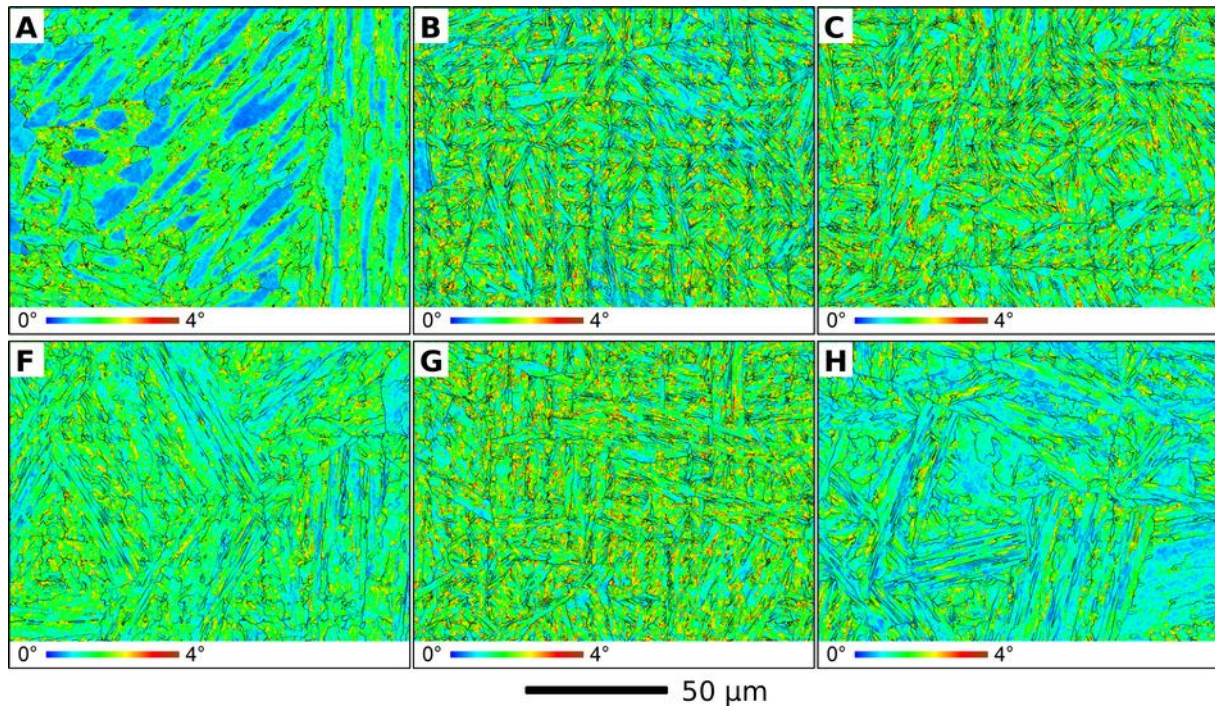
Figure 26: EBSD kernel average misorientation (KAM): The average misorientation between an individual measurement point X and a specified neighborhood is calculated. The neighborhood is defined by a square (area of interest) of 7 × 7 points, with point X being in the center of this square. Furthermore, the area of interest is limited to points, which belong to the same grain as does point X. Scale bar is the same for all mappings.
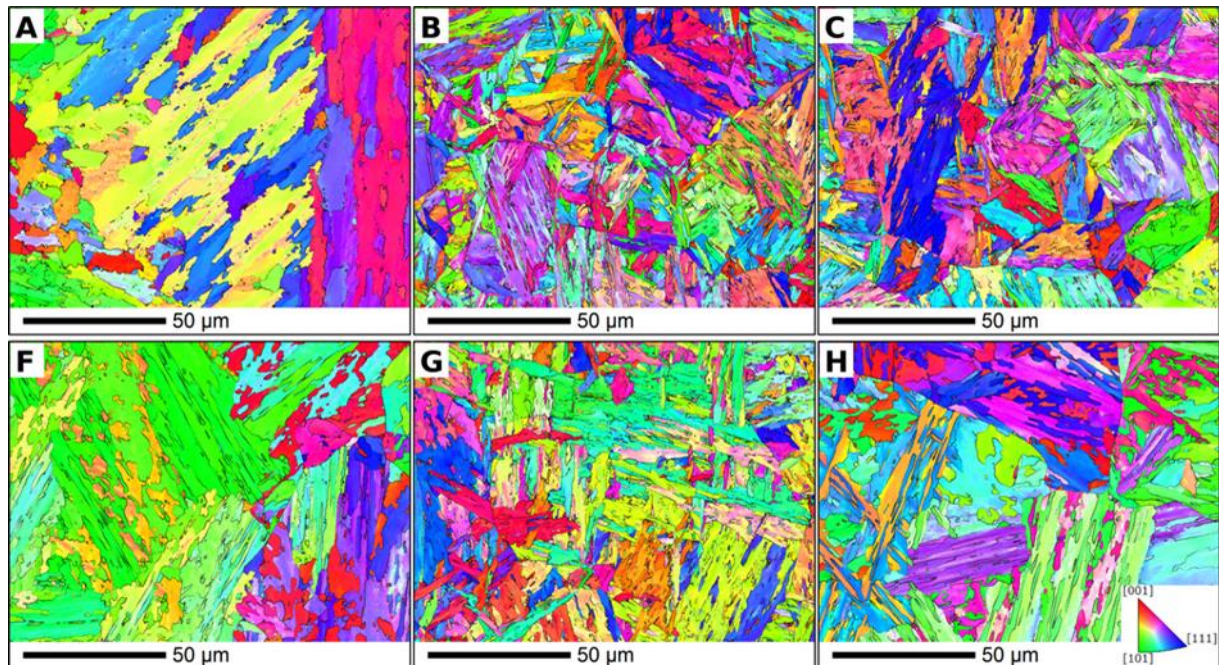
Figure 27: EBSD inverse pole figure (IPF) mappings for the samples normal direction.
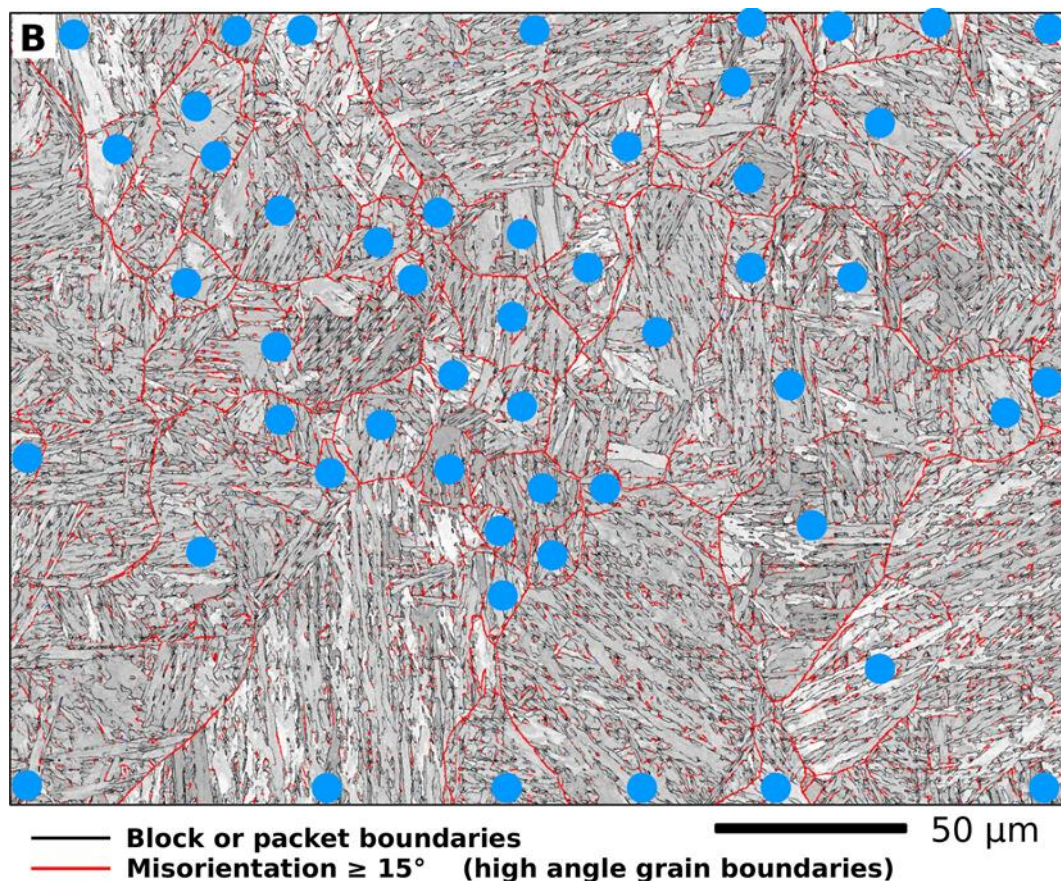
Figure 28: Prior austenite grain reconstruction by EBSD using alloy B as example. Each blue spot marks an austenite grain before the bainitic transformation.

Model Alloy	A	B	C	F	G	H
Step size [nm]	200	200	200	200	200	200
Mapped area [mm²]	0.059	0.059	0.059	0.059	0.059	0.059
Original indexation rate [%]	95.7	99.2	99.5	99.7	99.5	99.6
Indexation rate after data correction [%]	100.0	100.0	100.0	100.0	100.0	100.0
Total amount of altered data points [%]	5.3	1.3	0.9	0.5	0.9	0.7
Number of grains in EBSD mapping: total (including grains with less than 5 pixels)	6734	10010	8449	3580	9047	4109
Number of grains in EBSD mapping: after filter	1971	7858	6427	2972	7007	3590
Average grain size [μm]	**6.1**	**3.1**	**3.4**	**5.0**	**3.3**	**4.6**

Grain boundaries with 5° ≤ MOA*< 15° [%]	20	29	36	9	37	10
Grain boundaries with MOA*≥ 15° [%]	80	71	64	91	63	90
Prior austenite grain size [µm]	> 200?	40	42	89	46	97
Number of austenite grains in EBSD map	≈ 1?	47	42	10	36	8

Table 6: Summary of main EBSD measurement parameters and results.

Figure 25 demonstrates the grain boundary structure of the model alloys. The presence of the ferritic islands of model alloy A is confirmed by a lack of grain boundaries inside those areas. Accordingly, Figure 26 (kernel average misorientation) indicates a lower dislocation density in these islands. However, when correlating Figure 25 (grain boundaries) and Figure 27 (inverse pole figure mapping) for model alloy A, obviously, these ferritic islands are not separated by any grain boundary to the adjacent bainite microstructure as they have a similar orientation. Thus, their origin is given by the bainitic transformation and not by independent nucleation.

In contrast to model alloy A, alloys B, C, F, G and H exhibit a lath bainite microstructure. When compared to the alloys F and H, the steels B, C and G exhibit a smaller grain size and a pronounced presence of small angle grain boundaries that may be explained by different preferred variant selections during the bainitic transformation.

The EBSD data was used to analyze the grain boundaries with respect to the bainitic transformation orientation relationship. An example is given in Figure 28 using model alloy B. If a grain boundary corresponds to a bainitic transformation orientation relationship (within a tolerance threshold set to 3.5°), it has to be a block or packet boundary and is colored in black, while the remaining grain boundaries are given in red. Thus the remaining red colored boundaries are not block nor packet boundaries, but have to be prior austenite grain boundaries in Figure 28. In order to accommodate the strains during the bainitic transformation, in reality, the bainitic transformation orientation relationship is not sharp and exhibits a significant orientation spread (of order of at least 2°-3°). Thus, a precise distinction is often impossible for every single boundary segment and thus, Figure 28 obviously contains mistakes. However, the resulting image is enough to anticipate the shapes of prior austenite grains. Each area of a prior austenite grain is manually marked with a blue spot in Figure 28. Subsequently, the number of prior austenite grains was counted and the prior austenite grain size determined (Table 6). This procedure was applied for the other model alloys. The absolute number of prior austenite grains is rather low in model alloys F and H, but enough to provide an estimate for the prior austenite grain size. However, in the case of model alloy A, no prior austenite grain boundaries could be determined with certainty. It is suspected that for alloy A the whole EBSD mapping area originates from one single prior austenite grain and thus, only the lower limit of the prior austenite grain size can be estimated to about 200 µm or larger.

For model alloys B, C, F, G and H there is a correlation between a larger prior austenite grain size and the measured EBSD grain size according to the definition.

A clear trend between grain size, prior austenite grain size and the alloying composition cannot be found. However, as a general remark it can be stated, that small changes of alloying elements lead to significant changes in the microstructure. An explanation for this observation may be found in a change of the α-γ transition temperature of a steel as well as variant selection changes during the bainitic transformation, which may be sensitive to changes in composition.

SEM EBSD summary of A, B, C, F, G and H model steels

1. Model steel A (absence of Ni) results in an inhomogeneous bainitic microstructure. The interior of the largest bainite lathes exhibit reduced KAM values and a lack of low angle grain boundaries, resembling embedded ferrite. In most cases these ferrite islands are not separated by grain boundaries to the surrounding bainite and have the same orientation.

2. Steels B, C, F, G and H have a lath bainite microstructure.

3. In comparison to F and H, steels B, C and G exhibit a smaller grain size and a pronounced presence of small angle grain boundaries, thus indicating different preferred variant selection during the bainitic transformation.

4. EBSD data indicates noteworthy differences in the prior austenite grain size, with larger austenite grain size generally leading to larger block/packet size (= grain size).

4.2.2. Fractography of Model steels A, B and C

The fracture surfaces of Model steels A, B and C were characterized after the first fracture toughness testing round before the reconstitution. In total, 14 fracture surfaces were inspected. Examples of the initiation sites of Model steel A, B and C, including overview and large magnification images, are presented in Figure 29.

All Model steel A specimens initiated very close to the pre-fatigue crack tip. Typically, the fracture initiated from the middle of a large grain. The main initiators were not very clear since particles were not present.

Model steel B specimens also initiated very close to the pre-fatigue crack tip except specimen BC23, which had over 1 mm of ductile crack growth before brittle fracture initiation. Similar to Model steel A, the main initiators were not clear.

The main initiation sites of Model steel C specimens were 180 - 520 µm from the pre-fatigue crack tip. Two specimens reveal a particle as an initiator, one debonded with a size of 1.9 µm and one broken with a size of 2.0 µm. The initiators of other specimens were unclear.
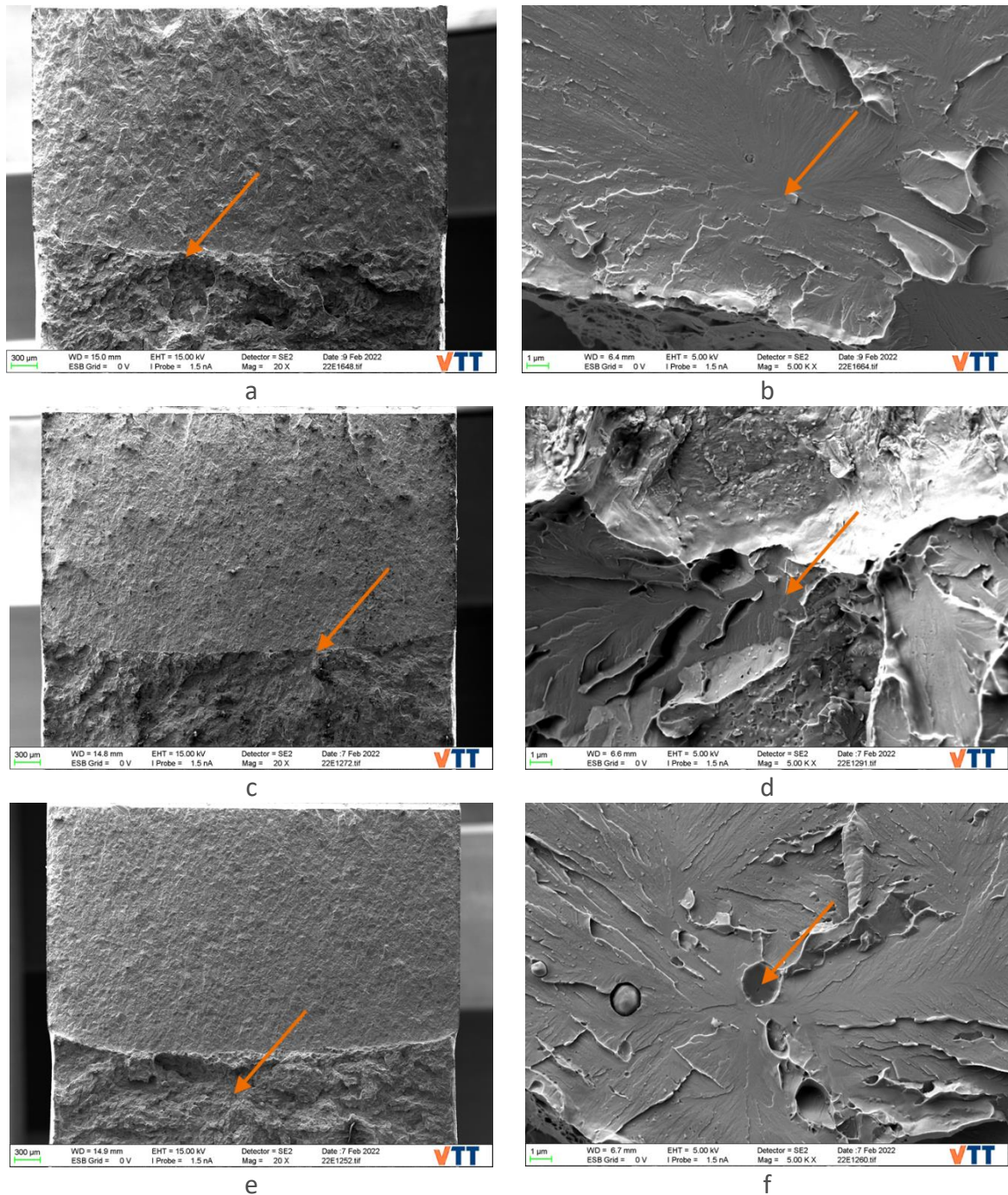
Figure 29: Overview and large magnification images of (a, b) AC26, (c, d) BC26 and (e, f) CC26 fracture surfaces. SEM secondary electron images where the initiation sites are marked with arrows.

The distance of initiation sites from pre-fatigue crack tip shows a correlation to the fracture toughness as shown in Figure 30 where the size of the ductile crack growth is included. Specimen BC23 can be seen as an outlier with the size of ductile crack growth over 1 mm.

A better correlation is also seen when the size of ductile crack growth has been removed from the distance, see Figure 31. This distance is the measured from the end of ductile crack growth to the initiation site. Especially Model steels A and C are showing linear elastic behaviour. Model steel B has initiated very close to the ductile crack growth regardless the K_{JC} value.
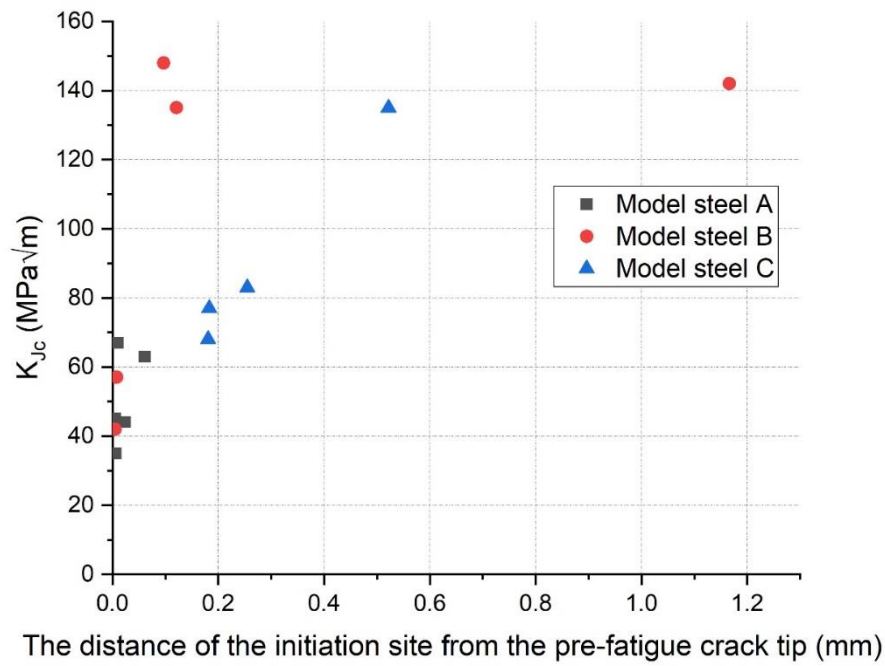
Figure 30: The distances of initiation sites from pre-fatigue crack tip of Model steels A, B and C.
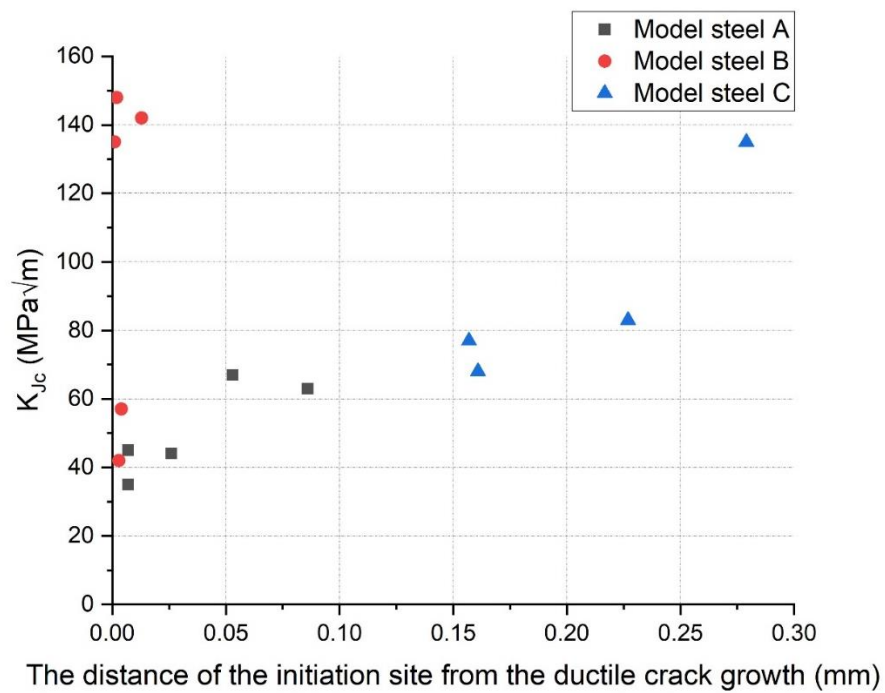
Figure 31: The distances of initiation sites from ductile crack growth of Model steels A, B and C.

4.2.3. Equilibrium diagrams of K, L, M and N model steels

To understand the following diagrams a summary of the fabrication routes included in the Technical Report: "Origin and Manufacturing of the LYRA-10 Specimens" is included:

The steels were fabricated according to the following route: casting, forging, hot rolling at 1180 ºC and subsequent thermal treatments for obtaining microstructures composed by a mixture of martensite and bainite. Afterwards, the steels plates were further heat treated with the aim of obtaining the same strength levels for all grades, with yield strength $R_{p0.2} =$ 550 ± 30 MPa. The treatments performed consisted of (1) isothermal treatment at 640 ºC for 10 h, in air atmosphere, followed by (2) austenitization at 940 ºC (grade K) or 900 ºC (grades L, M and N), with holding time of 20 min and subsequent water quench and (3) a final heating stage of the as-quenched microstructures at 640 ºC, in air atmosphere, for holding times of 12 h (grades K and L), 10 h (grade M) and 20 h (grade N).

Figure 32 contains isopleths of the equilibrium diagram calculated for the steels grades K, L and M; Figure 33 shows the results obtained for grade N. An important difference between the two diagrams is that for grade N, at 1.9 weight % Ni, a field containing α (ferrite), γ (austenite) and carbides M7C3 and MC exists between ~ 600 ºC and 690 ºC. Hence, for grade N, it is likely that the final heating stage at 640 ºC for 20 h consisted of an intercritical annealing, instead of tempering. The diagrams displayed in Figure 32 and Figure 33 were calculated for simpler chemical compositions, which contain only C and the main metallic alloying elements, not accounting for the effect of Si, Cu and impurities in the phase transition temperatures. Hence, experimental techniques like dilatometry are needed to properly characterize the temperatures at which phase transformations occur in the steels. Besides austenite (γ) and ferrite (α), microconstituents that can be present in the model steels are the ξ carbide, which is rich in Fe (~ 55 mass %) and in Mo (~ 38 mass %); the M7C3 carbide, rich in Fe when at temperature range of ~200 ºC to 700 ºC; the MC carbide (89 mass % Mo and 11 mass % C); the M3C2 carbide, rich in Cr; a Ni-rich phase (FCC) and a Fe-Ni FCC phase that can be considered as Ni-enriched austenite, formed by approximately 50 mass % Fe and 50 mass % Ni. The latter can be found in the equilibrium diagram calculated for steel grade N (Figure 33).
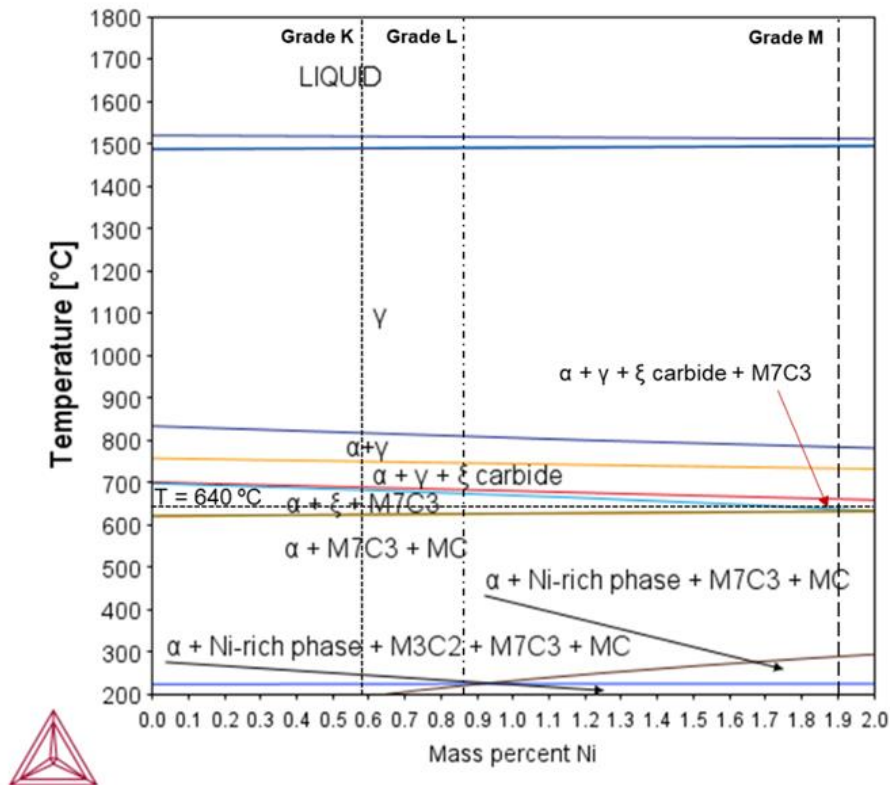
Figure 32: Isopleths of the Fe-Ni equilibrium diagram calculated for steels grades K, L and M.
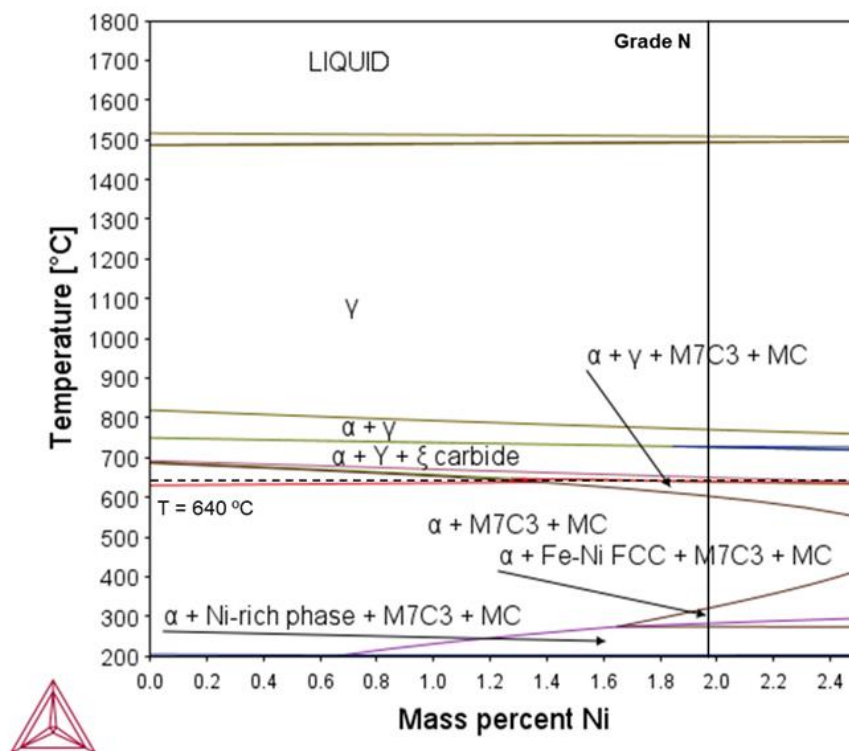
Figure 33: Isopleths of the equilibrium diagram calculated for steel grade N.

4.2.4. SEM of K, L, M and N model steels

In Figure 34, the secondary electrons micrographs indicating the matrixes of the four model steels in the un-irradiated condition can be viewed. All steels were observed in sections parallel and perpendicular to the rolling direction (Figure 2). No difference in grain morphology was observed for the two cross-sections and, therefore, the images shown here correspond to the section parallel to the rolling direction. In grades K and L the matrix is composed of a mixture of bainite and tempered martensite. In addition, a first qualitative observation indicates that the average grain size in grade K is smaller than in grade L. The microstructures of grades M and N exhibit qualitative larger grain sizes than grades K and L, and also are more complex. It is possible to observe in grades M and N a mixture of large ferrite grains (indicated in Figure 34), bainite and martensite; retained austenite has also been detected using optical microscopy (not shown in this work). For grade N, based on the equilibrium diagram displayed in Figure 33, the final heat treatment carried out at 640 ºC for 20 h corresponded to an intercritical annealing step: during this treatment, a fraction of the microstructure obtained after water quench from 900 ºC (martensite), was re-transformed into austenite and another fraction of the microstructure was tempered. Upon air cooling to room temperature (moderate cooling rate), the austenite will decompose into ferrite, bainite and carbides, explaining the heterogeneous microstructure seen in Figure 34 (grade N). It is likely that the same happened to grade M, during the same heat treatment, given the position of the compositional line in the equilibrium diagram of Figure 3 and the also heterogeneous microstructure seen in Figure 34 (grade M). Further investigation using dilatometry is necessary to explain the microstructures seen in grades M and N.
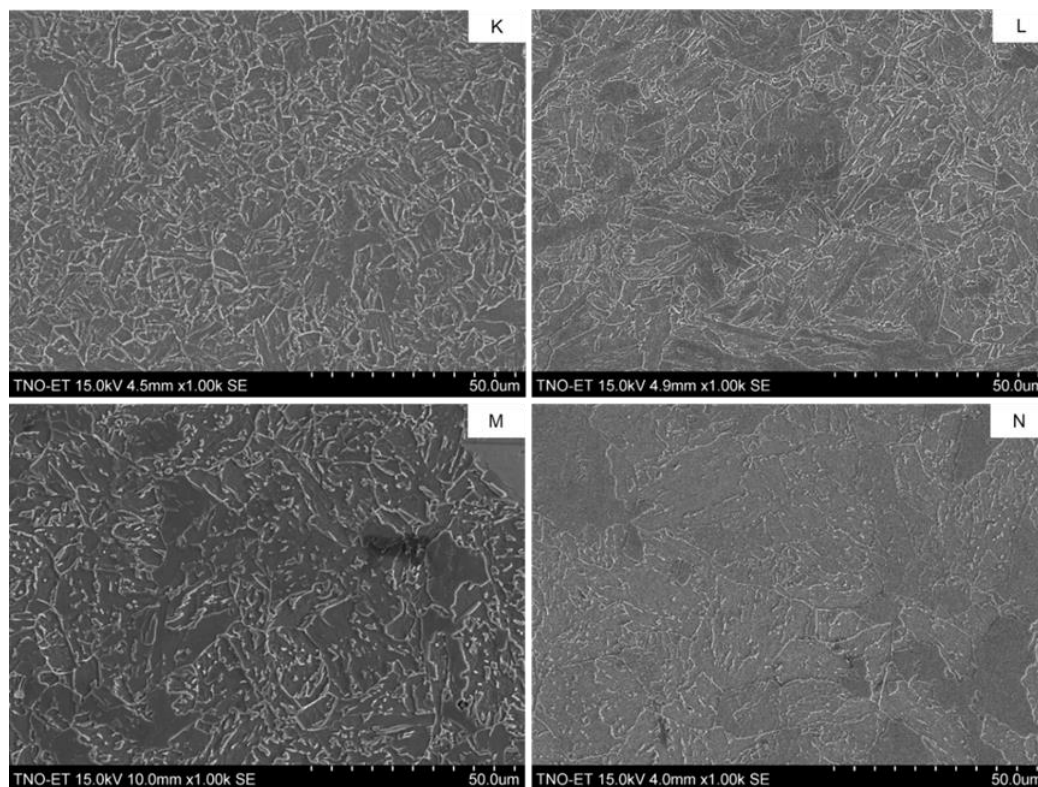
Figure 34: Secondary electrons images of the model steels grades K, L, M and N, in the un-irradiated condition. Magnification: 1000 X; etchant: Nital 2%.

In Figure 35, the microstructures of the model steels can be seen in more detail. For grades K and L, fine precipitates (bright features) are clearly seen along lath/grain boundaries; for grade M, no precipitates are observed and for grade N a small fraction of precipitates can be seen along grain boundaries (indicated by yellow arrows). The equilibrium diagram displayed in Figure 32 predicts the formation of ξ carbide and M7C3 at 640 ºC, for Ni contents of grades K and L; for grade M, it also suggests the formation of γ. The equilibrium diagram in Figure 33 shows that, for the Ni content of grade N and at 640 ºC, the material is going through a transition from M7C3 + MC carbides to ξ carbide. Therefore, all grades should contain precipitates in the microstructure, and it is unclear why grade M does not present a (detectable) fraction of precipitates.
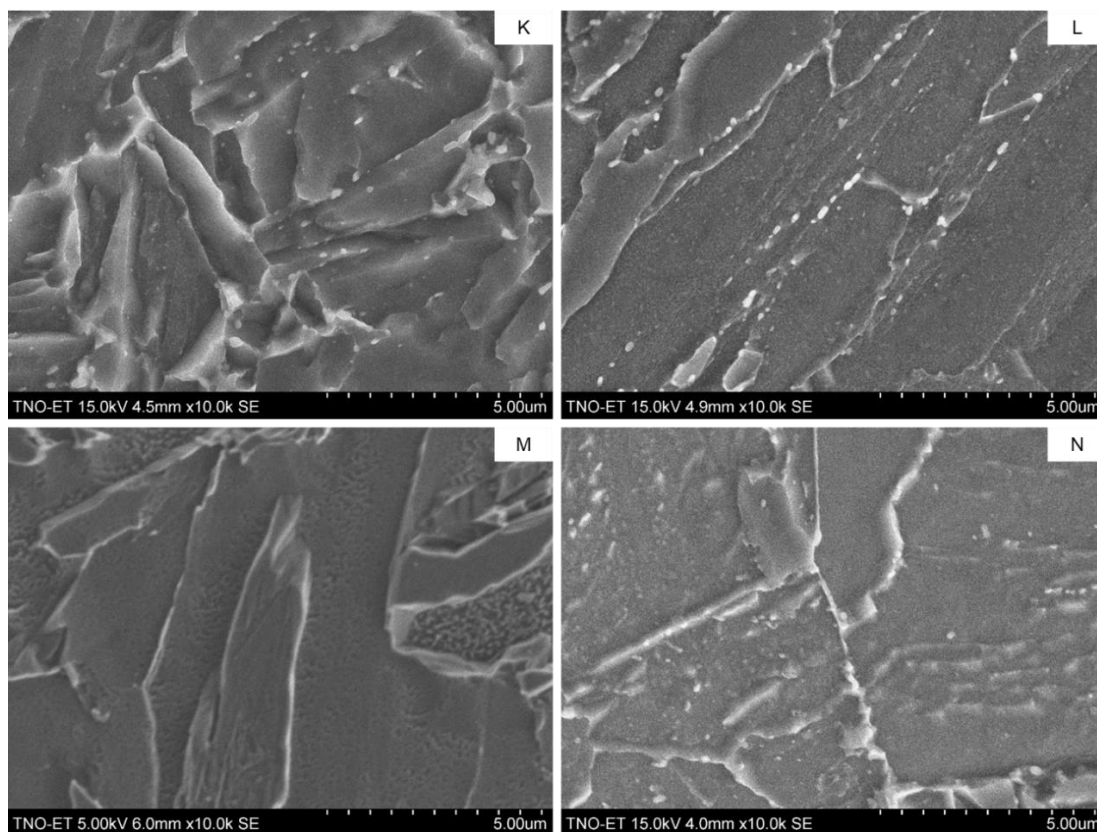
Figure 35: Secondary electrons micrographs of model steels grades K, L, M, N, in the un-irradiated condition, showing in more detail the matrix structure and fine carbides (grades K, L and N). Magnification: 10000 X; etchant: Nital 2%.

Summary of K, L, M and N model steels characterization

The preliminary microstructural characterization results obtained for steel grades K, L, M and N, using SEM and TEM (described in the corresponding section) show sufficient agreement with the Thermo-Calc predictions, except for steel grade M, with its absence of precipitates. For all grades, dilatometry measurements are necessary to characterize the temperatures at which phase transformations occur.

Grades K and L have similar microstructures, composed of tempered martensite, bainite and two types of precipitates: ξ carbide and likely M7C3 (more EDS measurements are needed to confirm the nature of the Fe-rich precipitates seen in Figure 58).

The microstructures of steels grades M and N are more complex, composed of a mixture of ferrite, bainite and martensite and, only for grade N, fine precipitates. The volume fraction of precipitates in grade N is qualitatively lower than the observed in grades K and L; further EDS measurements are needed to characterize these particles and overall quantification of particles will be carried out, in all steel grades. Optical microscopy analysis (not presented here) has shown the presence of retained austenite in grade M, which can be expected in this kind of material.

The microstructure seen in Figure 34 and the equilibrium diagram in Figure 32 suggest that a low volume fraction of austenite was formed during the heat treatment at 640 ºC for 12 h. Cooling to room temperature, in air, leads to austenite decomposition into ferrite, bainite, possibly a fraction of martensite and to the retention of austenite. Hence, the final microstructure of steel grade M is composed of the latter microconstituents and tempered martensite and bainite, which were previously formed during water quench, after austenitization at 900 ºC.

4.3. Transmission Electron Microscopy

All the model steels have been analysed by CIEMAT by (S)TEM and energy dispersive X-ray spectroscopy (EDS) maps have been also performed to study the different families of precipitates present in the materials.

Model steel A

Bright Field (BF) images of the microstructure of A model steel are shown in Figure 36. Figure 36 (a) shows a ferritic grain in the centre of the image surrounded by bainitic regions. Dislocation density change from ferritic grains to bainitic laths, being lower in the former case. Therefore, considering that dislocation density change from grain to grain, a mean value was estimated for ferritic grains, being $(1.4\pm0.1) \times 10^{14} m^{-2}$ and another one for bainitic grains, being $(2.5\pm0.2) \times 10^{14} m^{-2}$. A detail of the dislocation structure within bainitic grains is shown in Figure 36 (b). A fine distribution of small precipitates has been observe within grains (Figure 36 (c)). The size distribution of these precipitates is shown in Figure 36 (d), being the mean value (6.3 ± 0.1) nm with a density around $(1.6\pm0.3) 10^{21}$ m^{-3}.
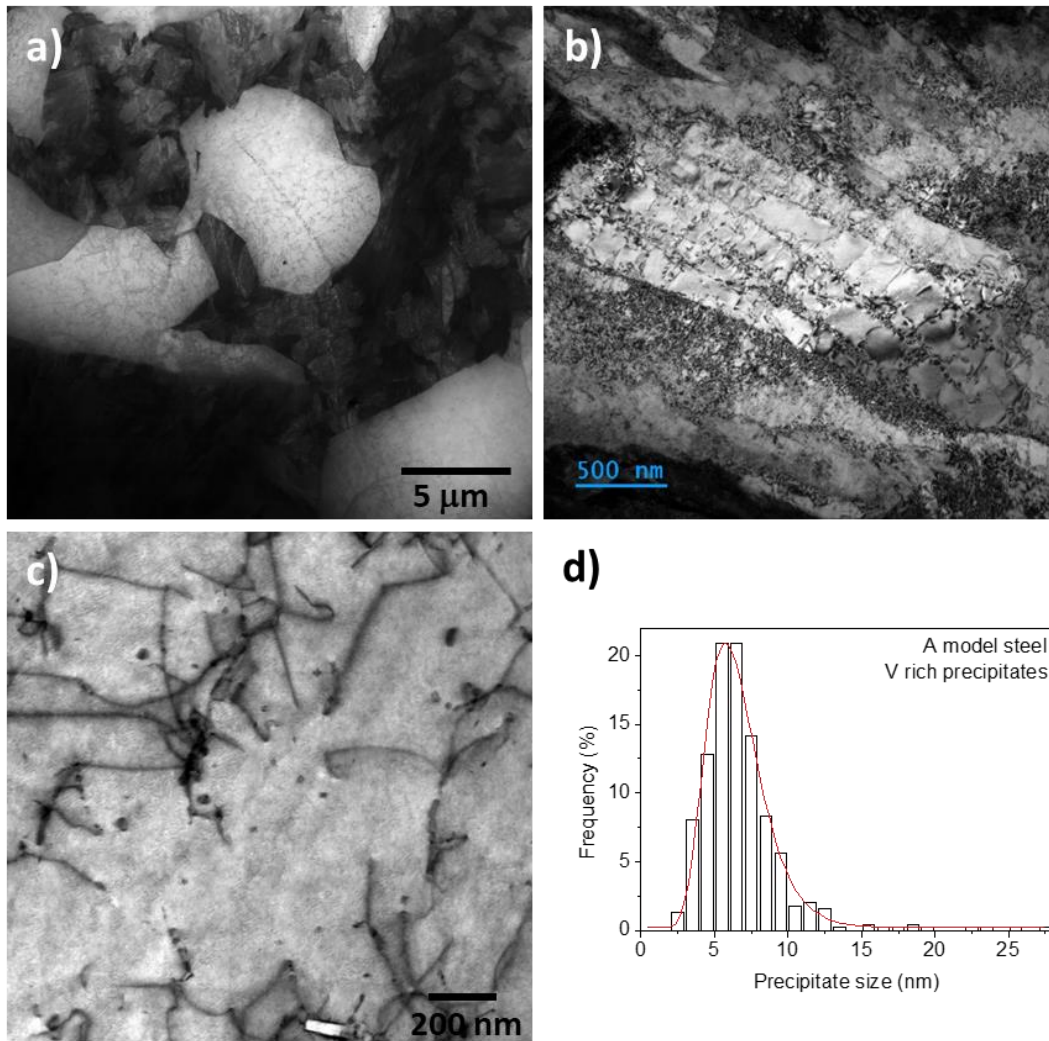
Figure 36: Bright Field (BF) images of a) ferritic grain surrounded by bainitic structure, b) dislocations within bainitic structure, c) Al (needle shape precipitates) and V rich precipitates (small disc shape precipitates) and d) dislocation structure within a ferritic grain.

Chemical mapping using EDS analysis confirms that the small precipitates within grains corresponds to V rich precipitates (Figure 37). Al was also detected and has been associated to contamination during fabrication process since there is no Al in the chemical composition of the material (Table 2).
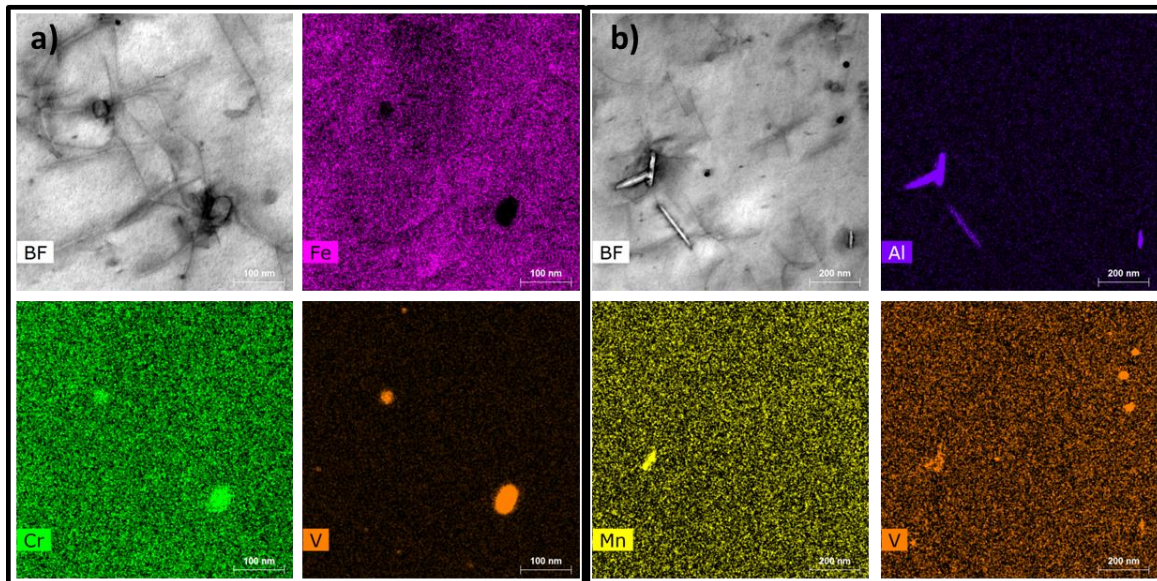
Figure 37: EDS maps of a) a region with V rich precipitates and b) a region with Al precipitates (needle shape) and V rich precipitates.

Additional characterization of model steel A were carried out at VTT. The STEM-BF images and STEM-HAADF images in Figure 38 reveal the mixture of ferrite and upper bainite. Both phases contain huge amount of dislocation network and the dislocation density in bainite phase is much higher than in ferrite phase. Additionally bainite phase shows variety of strain field contrast which well separated them from ferrite phase. The shape of ferrite grains depends on the shape of surrounded bainite, ranging from plate, round to polygonal. It is noted at the thin area that two kinds of small holes occurred due to particles dropped out during eletropolishing. Small round shape holes correspond to small precipitates and large irregular holes to small bainite variants.
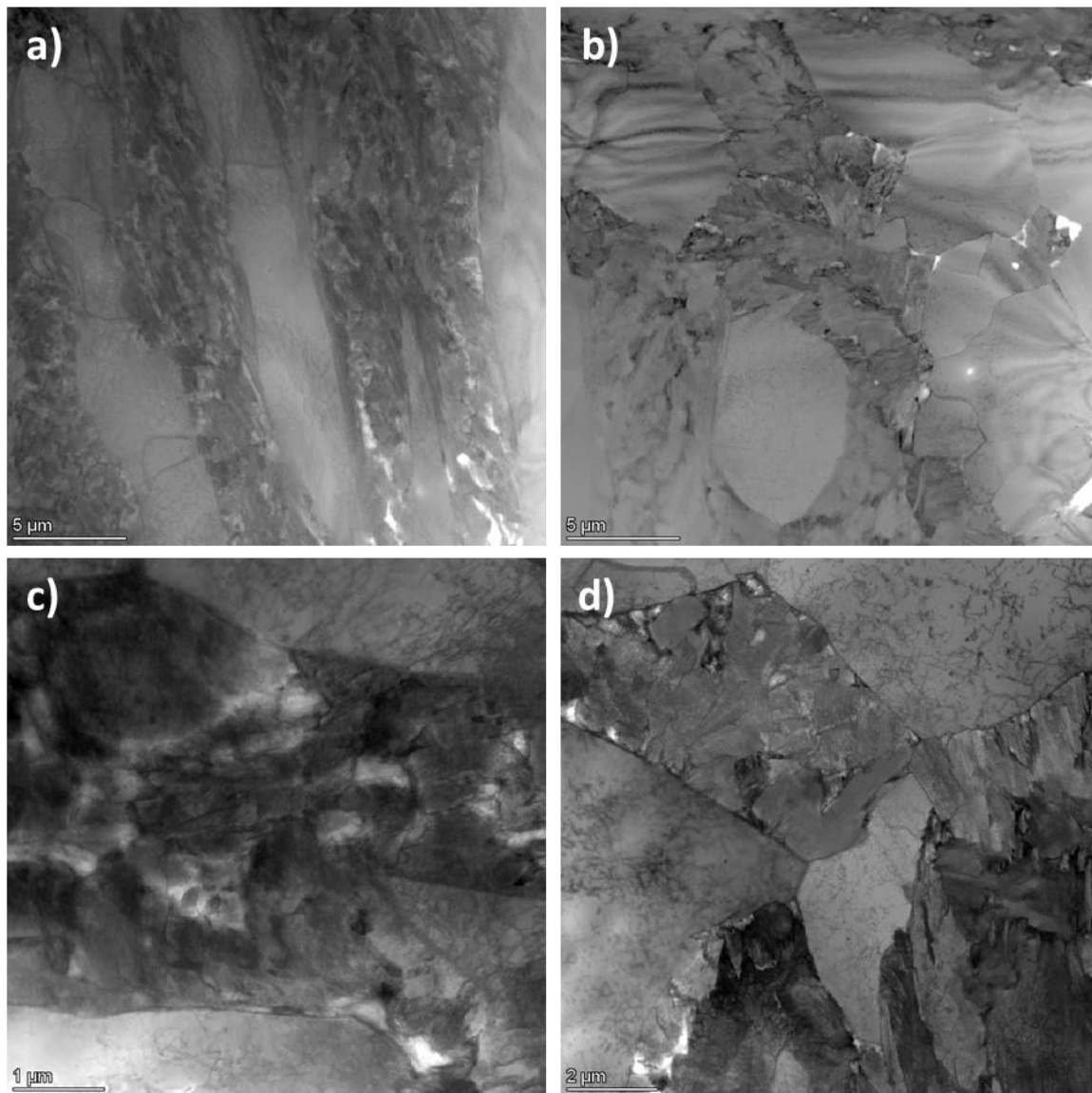
Figure 38: The mixed ferrite and upper bainite in different appearance in specimen AC26. (a,c) STEM BF image and (c,d) STEM HAADF image with inverse contrast.

Carbides are not commonly present at boundaries between both bainite and ferrite or bainite laths in this sample. However, one relatively large M_3C carbide plate was imaged in Figure 39 with its SAED pattern indexed along ZA [153] of M_3C. EDX mapping in Figure 40 confirms that it is a carbide plate. Furthermore, vanadium elemental map shows clearly the V-rich nano-sized precipitates. The largest nano-sized V-rich precipitate also contains N, but the small ones are hardly visible in N map maybe due to its low x-ray emission. The small round holes at thin areas are the locations of those relatively large V nitride particles, which were polished out during electropolishing process.
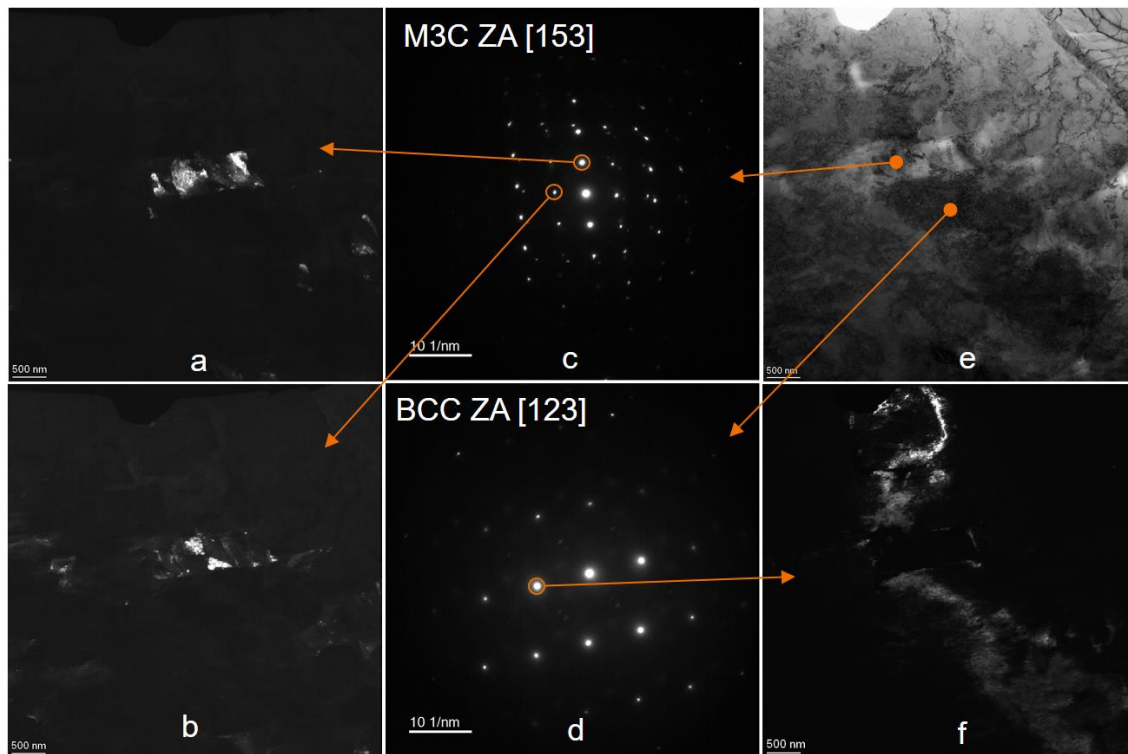
Figure 39: M3C carbide between bainite variant. (a, b) DF images from correspond reflection in (c), (c) SAED of M3C carbide along ZA [153]; (d) SAED of bainite variant along BCC ZA [123] below M3C carbide; (e) carbide between bainite lath with ferrite phase in right corner ; (f) DF of bainite from reflection (d).
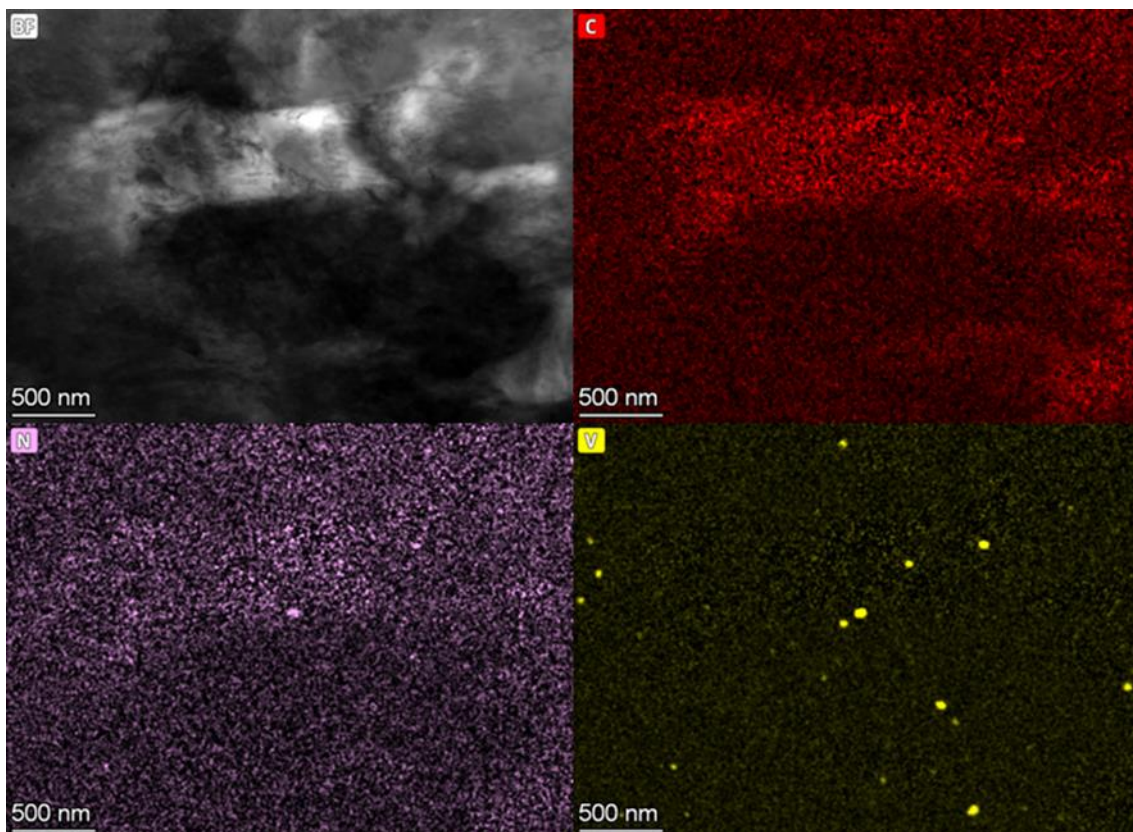
Figure 40: EDX map shows carbide and nano-sized V-rich precipitates.

Model steel B

Weak Beam Dark Field (WBDF) and BF images of B model steel are shown in Figure 41. Lath width has been estimated employing images as the one shown in Figure 41 (a), being the mean value (302±9) nm. Figure 41 (b) shows the presence of small precipitates that correspond to V rich precipitates as EDS confirms, not only within grains, but also placed at lath boundaries. The size of this precipitate has been estimates being the mean value (7±1) nm, in the same order than those observed in the case of A model steel. Finally image as the one shows in Figure 41 (c) were employed to estimate the dislocation density that in the case of B model steel corresponds to $(2.1\pm0.3) \times 10^{14}$ m^{-2}.
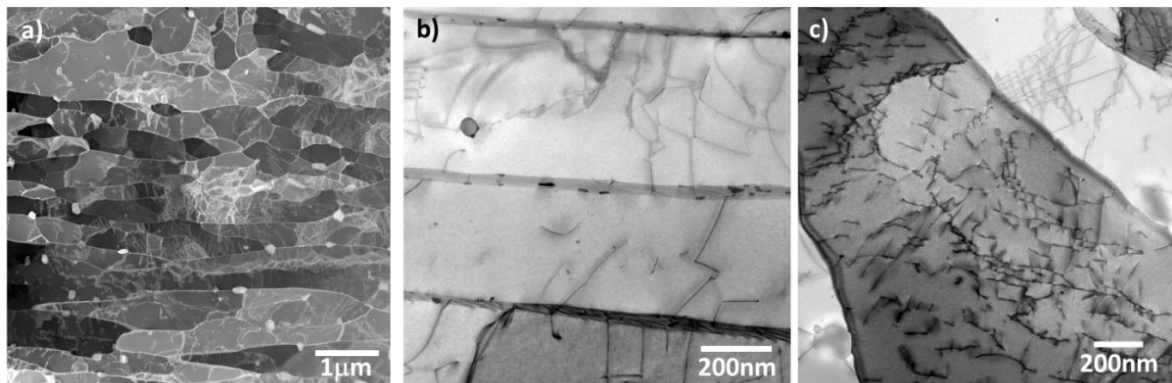
Figure 41: a) Weak Beam Dark Field (WBDF) image of the lath structure, b) BF image of a detail of the lath boundaries with small V rich precipitates and c) a detail of the dislocation structure within laths.

EDS analysis are shown in Figure 42. Coarse Cr carbides with Mn and Mo has been detected normally placed at grain boundaries. Those placed at primary austenitic grain boundaries (PAGBs) are coarser since diffusion process are favoured. Small V precipitates has been also detected. Again coarser ones are place at grain boundaries.
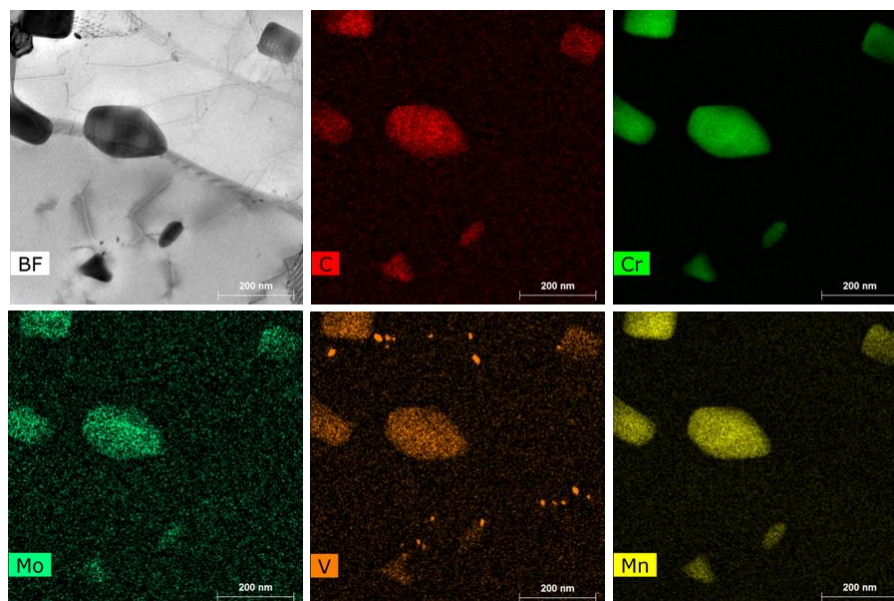
Figure 42: EDS maps of a region were coarse carbides and small V precipitates has been detected.

An example of each family of precipitates detected by EDS is shown in Figure 43. Figure 43 (a) shows a Cr carbide with Mo, Mn and V in their composition and Figure 43 (b) an example of the V rich precipitate.
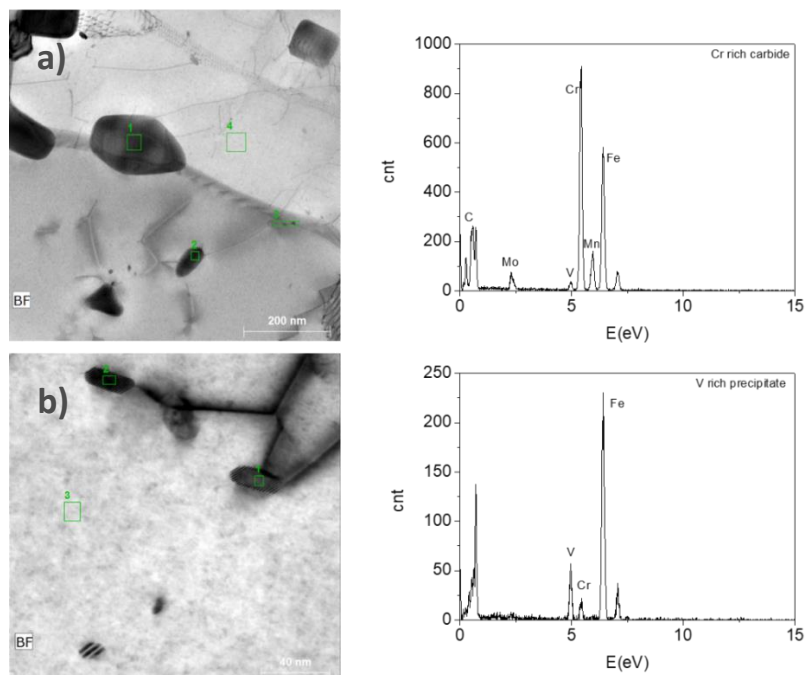
Figure 43: Examples of qualitative EDS analysis for a) a Cr rich precipitate and b) a V rich precipitate.

Additional characterization of model steel B were carried out at VTT. Both in normal TEM and STEM images the microstructure of BC26 exhibits a complete lower bainite structure, in which different packets of bainite formed from previous austenite grains, shown in Figure 44 (a,c). Bainite contains large density of dislocations and exhibits strong strain field contrast. Fine carbides are well visible both at bainite lath boundary and inside lath. The white spots in left corner of Figure 44 (a,c) are holes left by dropped out carbides during eletropolishing. In the TEM BF image of Figure 44 (d), the dark area is one lath tilted to ZA [111] showing high density of dislocation entangles. Even though there are carbides inside lath, the diffraction pattern show only BCC lattice, most likely due to small nano-size of carbides.
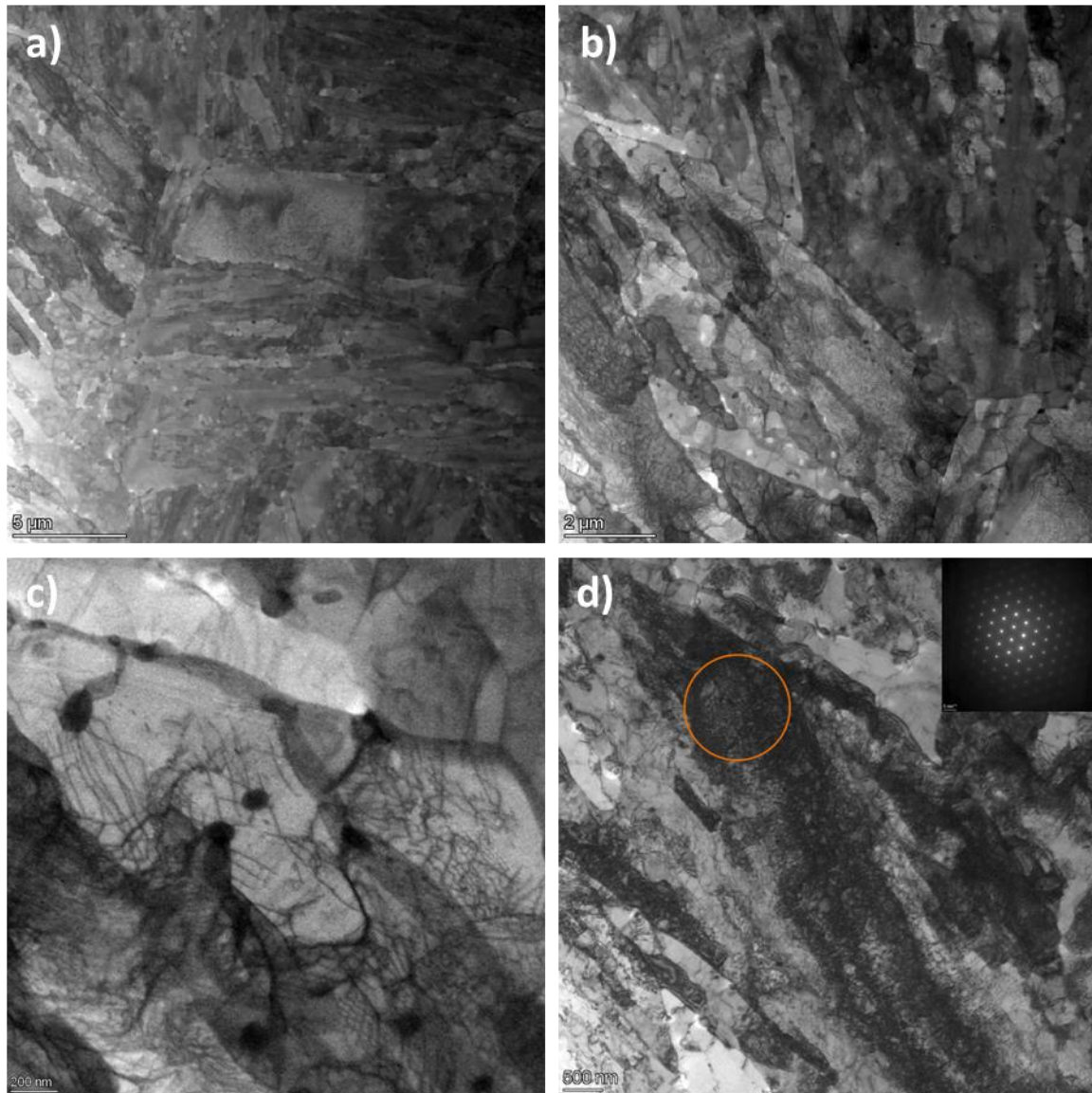
Figure 44: (a,b,c) STEM BF images of lower bainite, (d) TEM BF image and inset is SAED pattern of circled area which shows BCC lattice along ZA [111].

The EDX map of Figure 45 shows complex carbides distributions in lower bainite. The majority of carbides are Cr dominated which also contain Mo, Mn and V, and they locate both along lath boundary and inside lath with either a round shape or elongated needle shape. The elongated Cr carbides are preferred laying along lath boundary. Inside lath, there exist small nano-size and round shaped carbides that are Mo dominated Mo-Cr carbides. Similar to AC 26 large amount of V-rich particles exist and some of them are VN widely spread in the matrix. It is worth to note that one particular MnS particle was found next to lath boundary in the middle of image.
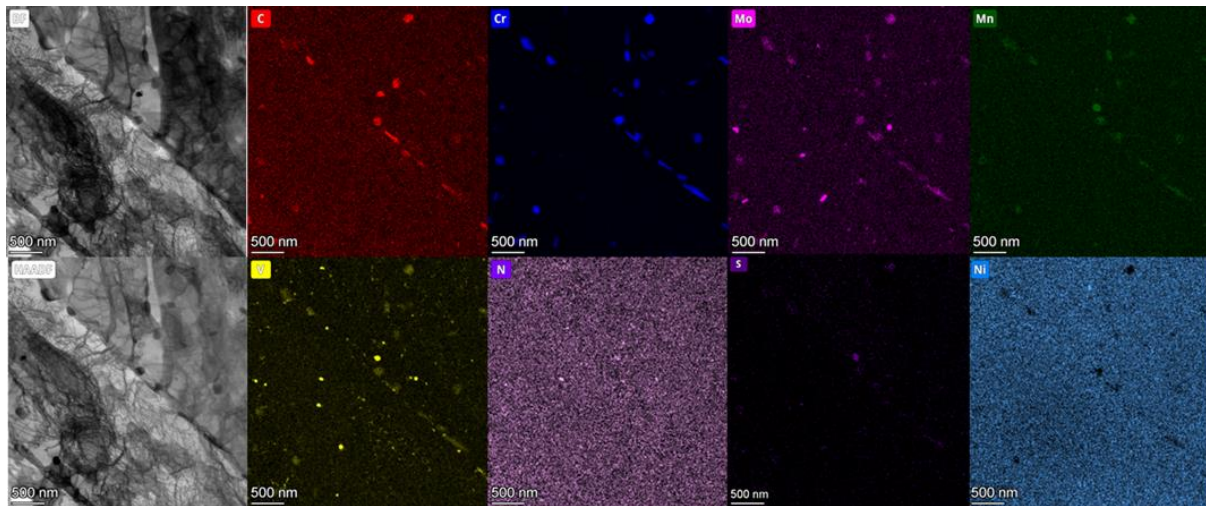
Figure 45: EDX map revealing Cr dominated carbides along bainite lath boundary and Mo dominated carbides mostly inside lath, and V riched particles and that VN are widely spread in matrix. One MnS particle in the middle of image was detected.

Model steel C

The microstructure of C model steel is shown Figure 46. The same grain structure that the one described for B model steel has been observed in this case (Figure 46 (a) and (b)). Lath width has been measured obtaining a mean value of (355±18) nm. In this case there is a slightly increase in the dislocation density, $(3.5\pm0.5) \times 10^{14}$ m^{-2}, compared to A and B model steels. V rich precipitates have been also observed preferably placed within grains and at bainitic lath boundaries. The mean size in this case is slightly higher, (9.8±0.6) nm (Figure 46 (c)).
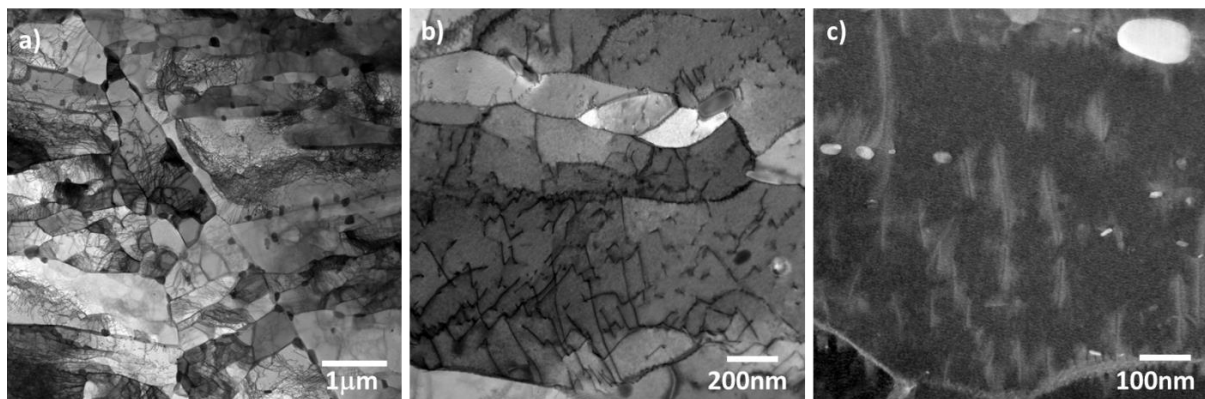
Figure 46: a) BF image of the microstructure of C model steel, c) detail of the microstructure and c) WBDF image of precipitates at grain boundaries and within grains.

EDS results show the presence of the same precipitates analysed in A and B model steels. Coarse carbides placed at grain boundaries and V rich precipitates within grains and at grain boundaries (Figure 47).
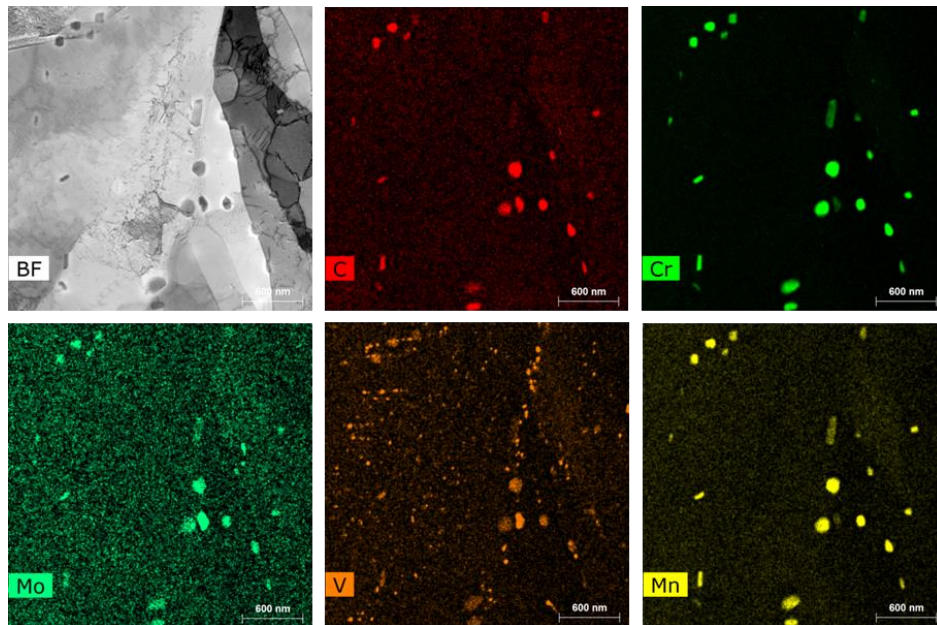
Figure 47: EDS maps of a region were coarse carbides and small V precipitates has been detected.

Additional characterization of model steel B were carried out at VTT. Steel CC26 has a very fined lower bainite structure with subunit size as small as about only 100 nm, shown in Figure 48 (a,b). Similar as BC26, bainite phase consists of large amount of dislocations and images show strong strain field contrast. Large amount of carbides decorated along lath boundaries. Only very small amount of carbides found inside bainite laths. The SAED pattern from one lath show only BCC lattice along ZA [111].
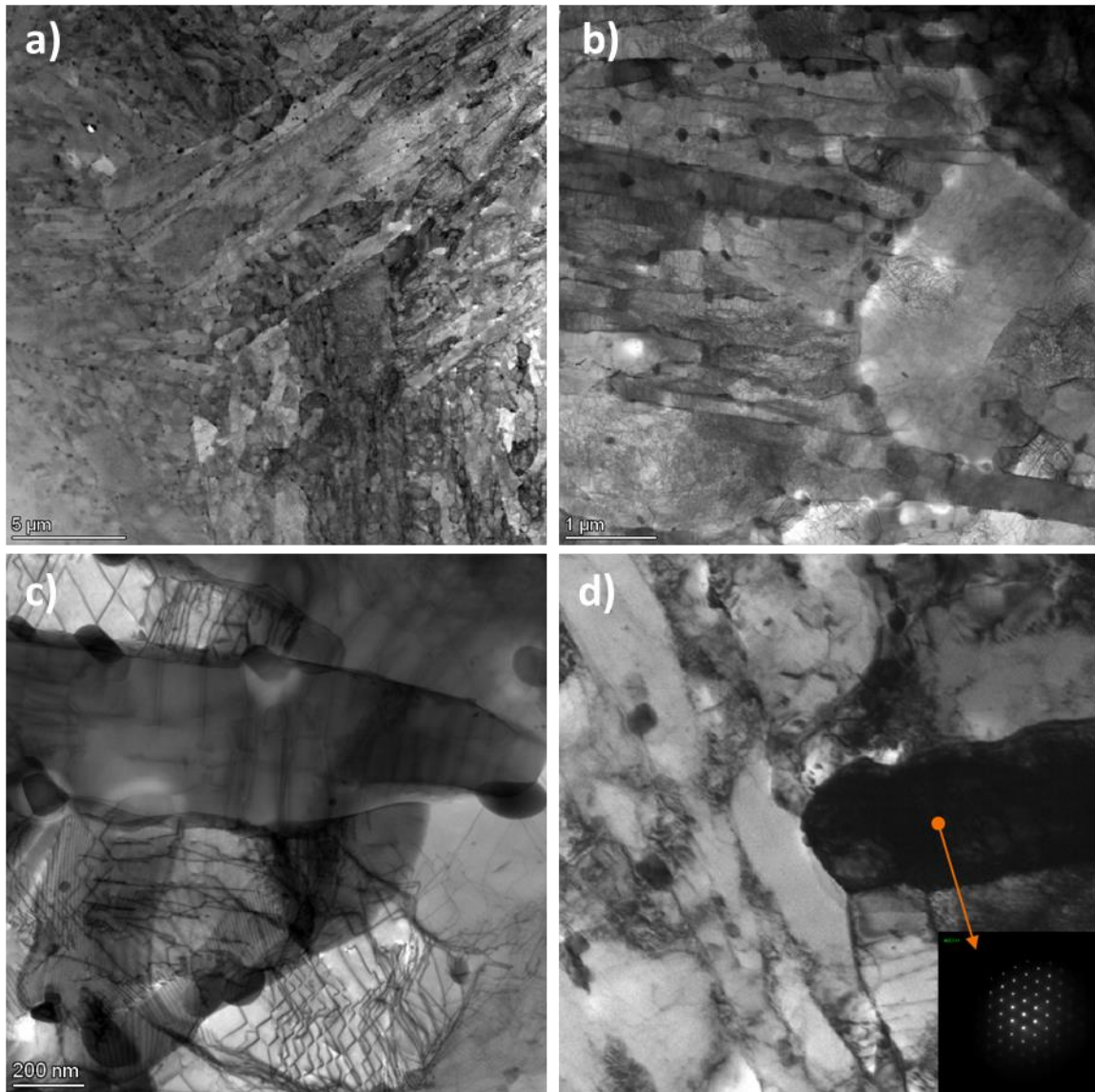
Figure 48: Lower bainite (a) STEM HAADF image with inverse contrast; (b) and (c) STEM BF images; (d) TEM BF and SAED pattern from one bainite lath.

EDX map reveals carbides distribution, with almost all carbides preferably locating along lath boundaries, shown in Figure 49. Relatively large size carbide are Cr dominated which contains Mo, Mn and V, and small size carbides are Mo dominated containing Cr and V. Most of carbides are round shape. Almost all Cr dominated carbides with elongated stick shape lay along lath boundaries and the elongated Mo dominated carbides are usually found inside laths. Vanadium rich particles has a higher population than carbides, and they also show a preferred location at lath boundaries. However, the number of VN particles in CC26 are less than AC26 and BC26.
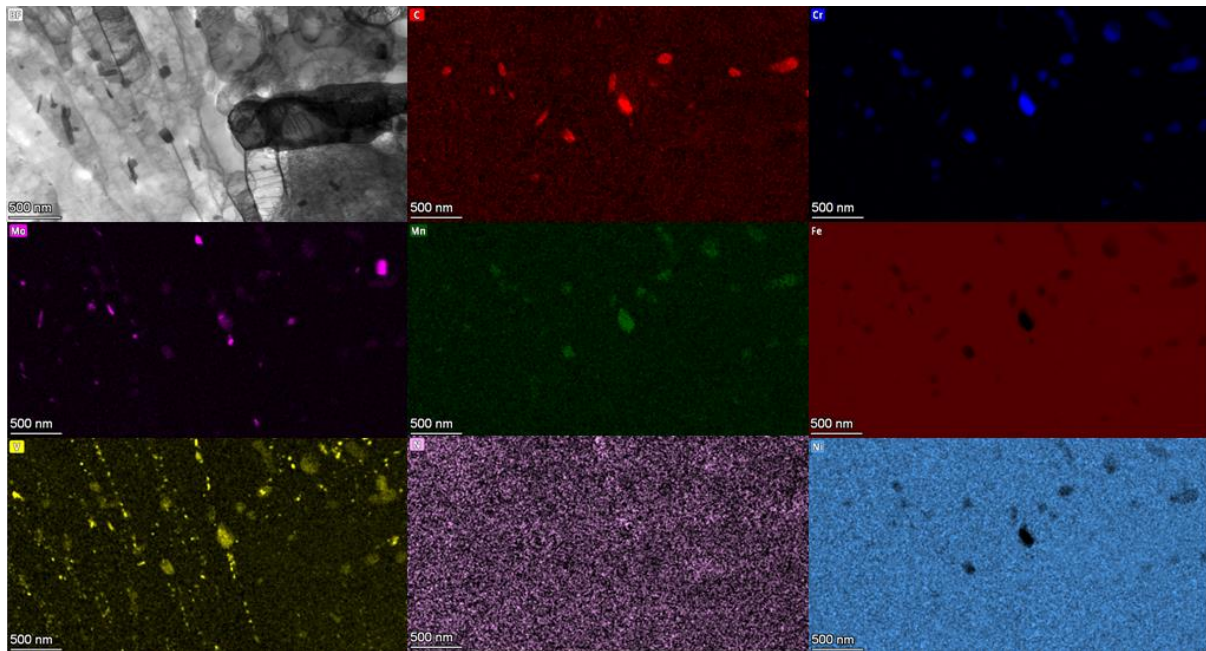
Figure 49: EDX map shows Cr dominated and Mo dominated carbides and V-rich particles preferably laying along lath boundaries.

Model steel F

Bright field composition of images of F model steel is shown in Figure 50 (a). Elongated grains with a high dislocation density coexist with more or less equiaxial grains with a lower dislocation density. Coarse precipitates observed in Figure 50 (b) appear in general placed at grain boundaries and triple points. Last image, Figure 50 (c) shows a detail of subgrains with low dislocation density that was estimated to be $\rho_{disloc} = (1.4 \pm 0.2) \times 10^{14}$ m^{-2}. Finally, the width of the bainitic grains was also estimated with the TEM images, being the mean value (471±13) nm, thicker that those measured for B and C model steels. Small V precipitates were observed occasionally within grains and slightly more frequently at grain boundaries. A mean size value was estimated being (8±2) nm.
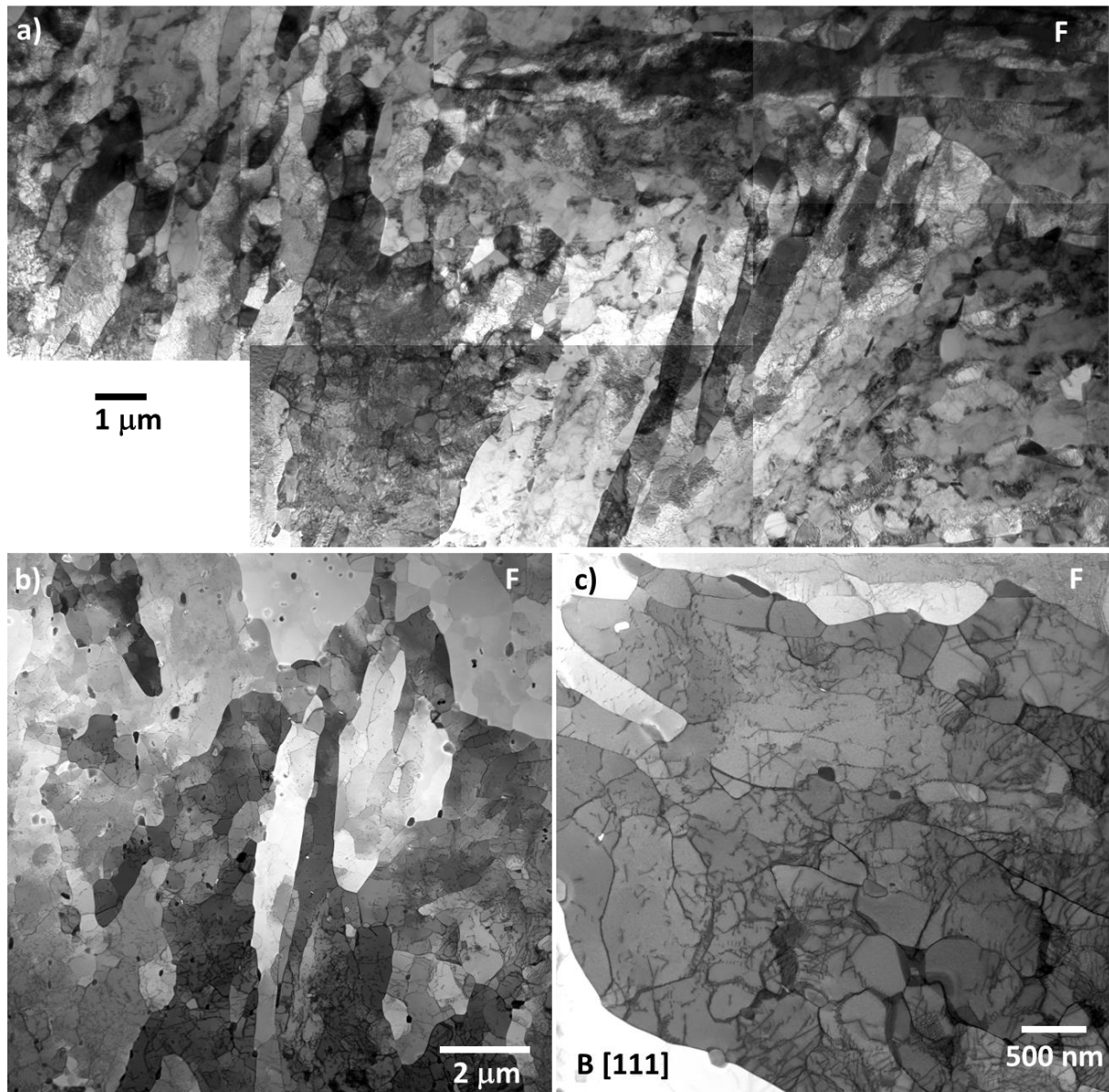
Figure 50: a) Bright field composition of images of F model steel, b) detail of grain structure and distribution of coarse precipitates and c) detail of dislocations and subgrains with B[111] orientation.

Chemical mapping using EDS was done in different regions of the material (Figure 51). This qualitative analysis shows that coarse precipitates are mainly Cr rich carbides with Mn, Mo and V and the small precipitates, no visible in the bright field image, are identified as V rich precipitates. As has been explained above, these precipitates appears mainly at grain boundaries and no within grains as in the previous studied model steels and as can be seen in the corresponding V map.
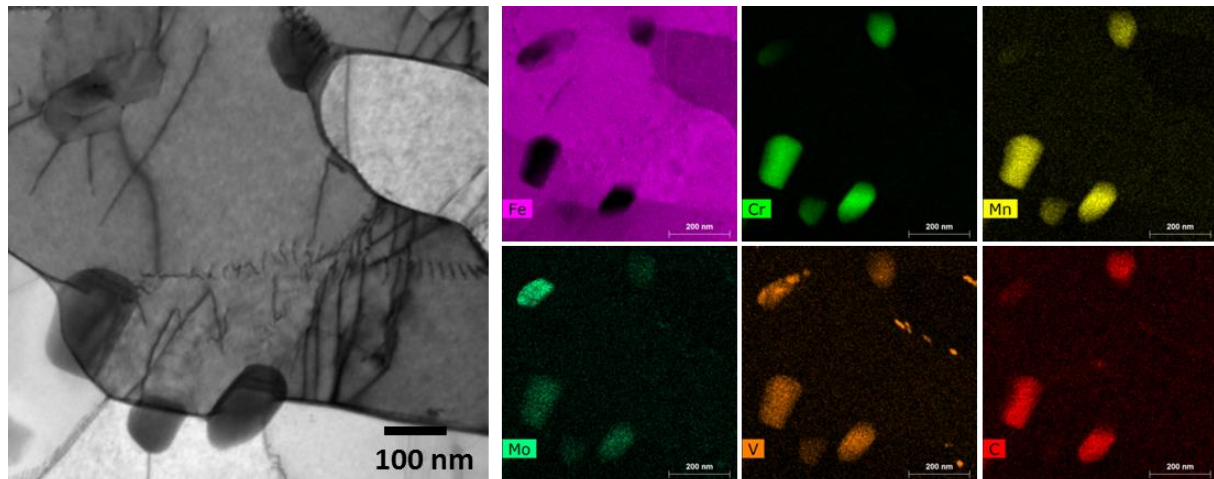
Figure 51: EDS map of a region with different families of precipitates.

Model steel G

Bright field images of G model steel are shown in Figure 52. Elongated grains were observed with a similar orientation within the same PAG (Figure 52 (a)). The width of these grains has been measured in images like the one shown in Figure 52 (a), being the mean value (361±15) nm. A higher dislocation density is observed (Figure 52 (a)) compare with F model steel (Figure 50 (b)). The mean value calculated is ρ_{disloc} = (3.3 ± 0.7) x 10^{14} m^{-2}, similar to the one observed for B and C model steels. A distribution of small precipitates was observed within grains (Figure 52 (b) and Figure 52 (c)) that act as pining points for dislocations. The V rich precipitates size distribution is indicated in the chart shown in Figure 52 (d), being the mean value (7.9±0.3) nm.
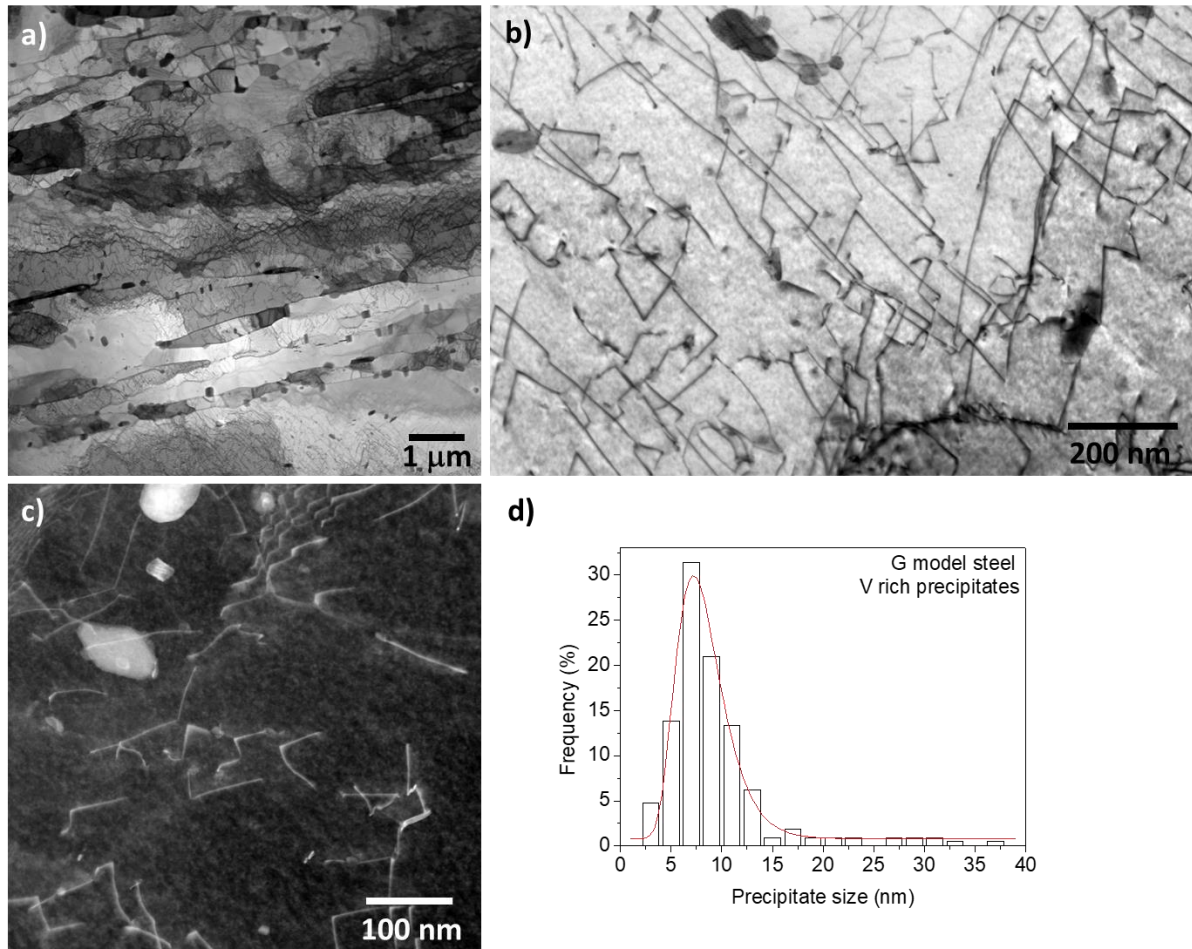
Figure 52: BF images of a) dislocation distribution within bainitic grains, b) precipitates and dislocation distribution, c) WBDF image of a detail of V rich precipitates within grains and d) V rich precipitates size distribution.

Chemical mapping using EDS was done in different regions of the material. An example is shown in Figure 53. As in the other model steels we can see that small precipitates corresponds to V-rich precipitates and the coarse ones (Cr, Mn) rich carbides and Mo rich carbides.
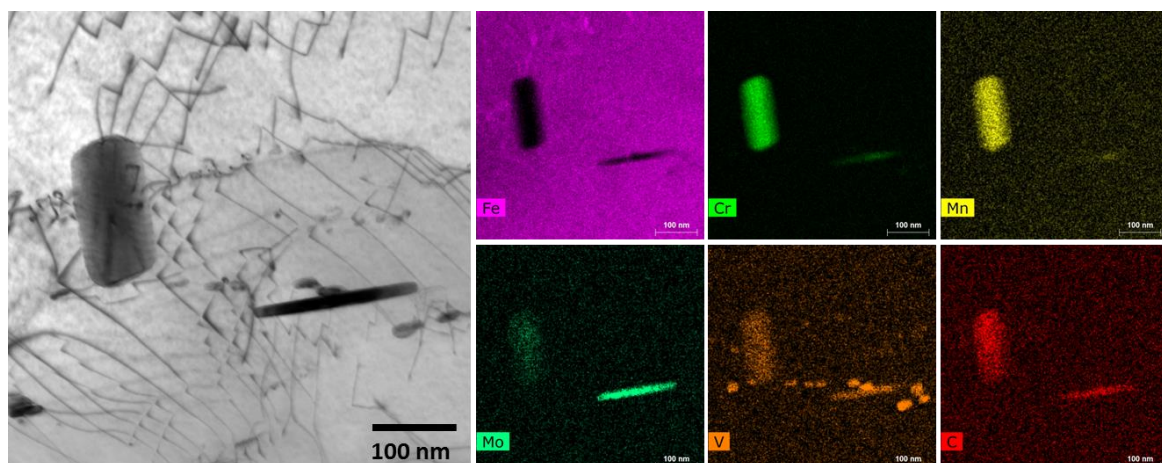
Figure 53: EDS map of a region with different families of precipitates.

Model steel H

The microstructure of H model steel is very similar to the one observed for F model steel. Bright field images are shown in Figure 54. Elongated grains coexists with more or less equiaxial grains. The dislocation density (Figure 54 (b)) estimated in this case has a value of $(1.7\pm0.2) \times 10^{14}m^{-2}$, a similar value to the one obtained for F model steel. Regarding lath width, a value of (436 ± 23) nm has been measured, again similar to F model steel. Regarding V rich precipitates, the mean size value estimated is slightly higher than for the others model steels, (13 ± 1) nm. The presence of Cu rich particles can lead to measurements errors.
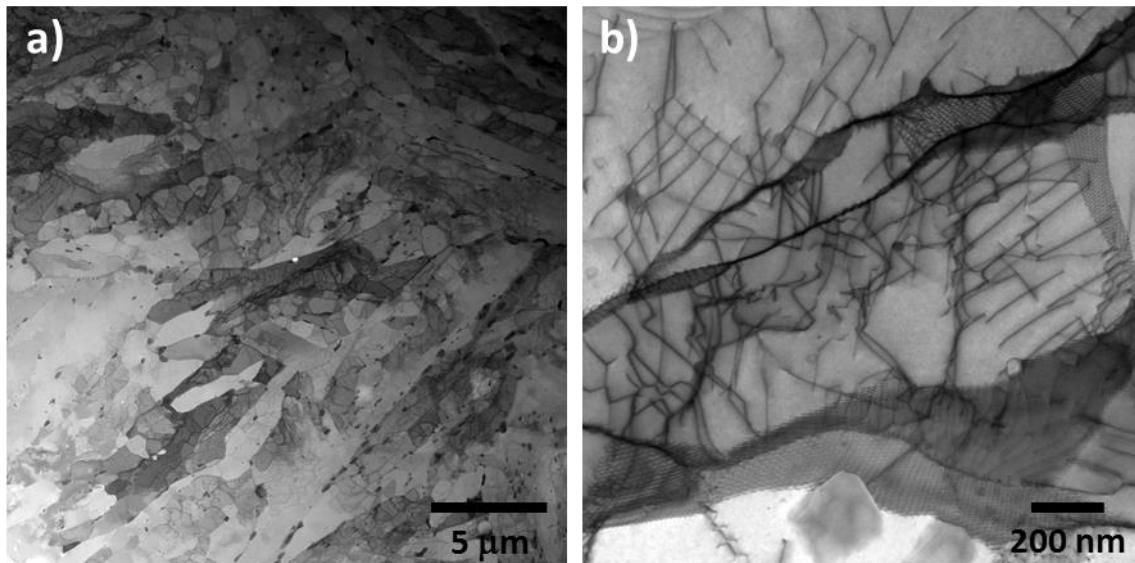
Figure 54: Bright field images of a) general microstructure of H model steel and b) dislocation distribution and precipitates within grains

As in the case of previous analysis of other model steels, EDS results indicate the presence of coarse carbides enriched in Cr, Mo and/or Mn as well as the presence of small V precipitates within grains and grain boundaries (Figure 55 (a)). However, in H model steel apart from Al precipitates that were also detected in A model steel, Cu rich precipitates were observed within grains (Figure 55 (b)) that were not observed previously in the other model steels.
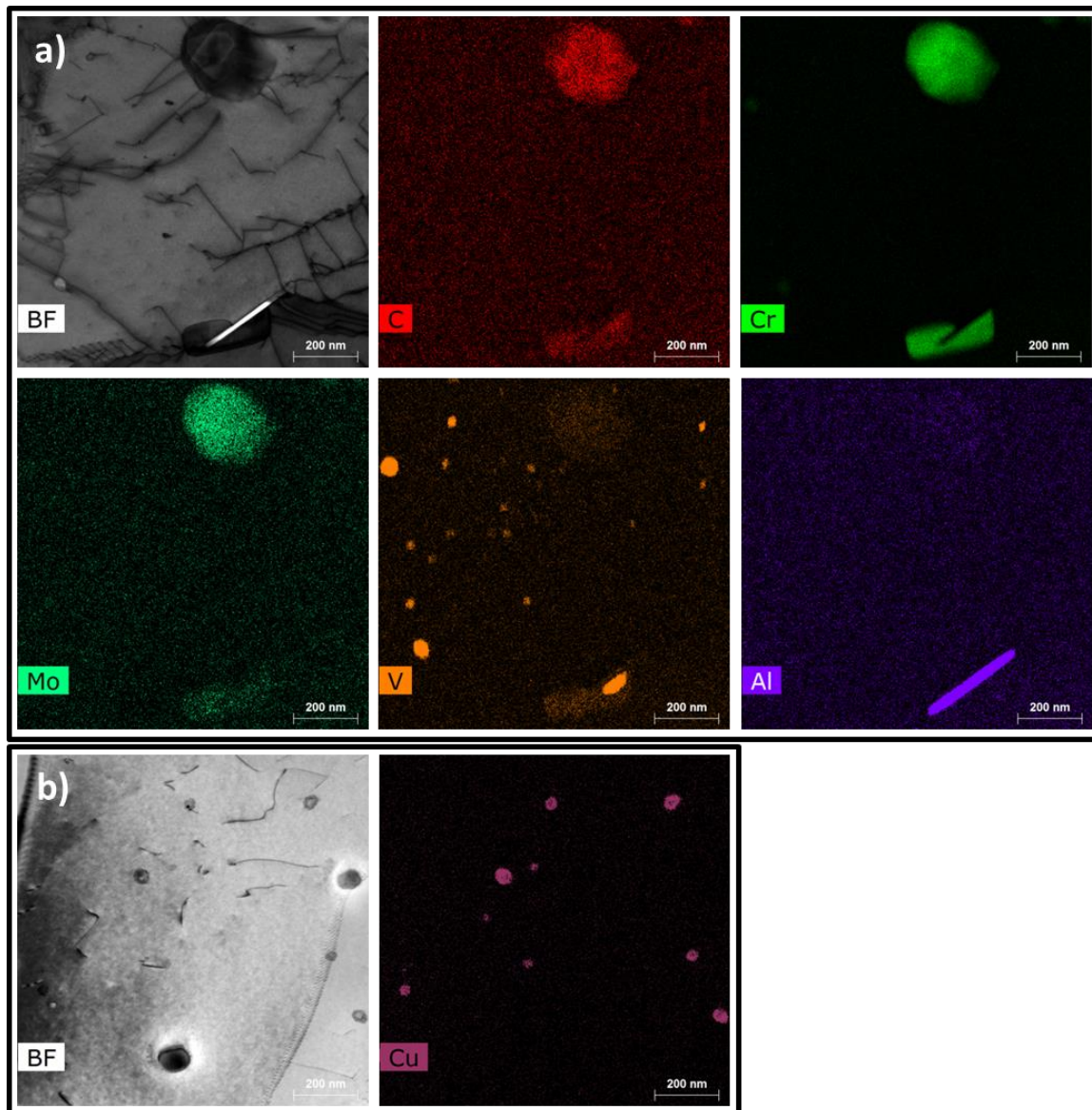
Figure 55: EDS maps of a) a region with coarse carbides, V rich precipitates and an Al needle and b) a region with Cu rich precipitates within grains.

TEM Summary

Finally, in Table 7 there is a summary of the measurements made in each model steel.

Elongated grains with a high dislocation density coexist with more or less equiaxial grains with a lower dislocation density. In the case of model steels ferritic grains were also observed. Dislocation density is slightly lower for A, F and H model steels. All the measurements have been done with grains oriented on zone axis [110]. The evolution of lath width seems to follow the same tendency than dislocation density. Thicker laths correspond to lower values of dislocation density.

Model	Lath width (nm)	Dislocation density ($10^{14} m^{-2}$)	V-rich precipitates size (nm)
A	-	F: 1.4±0.1/B: 2.5±0.2	6.3±0.2
B	302±9	2.1±0.3	7±1
C	355±18	3.5±0.5	9.8±0.6
F	471±13	1.4 ± 0.2	8±2
G	361±15	3.3 ± 0.7	7.9±0.3
H	436±23	1.7±0.2	13±1

Table 7: Summary of the principal results of the analysis.

Regarding precipitates, coarse carbides enrich in Cr, Mn and/or Mo have been detected as well as small V-rich precipitates. The amount of coarse precipitates placed at grain boundaries is much lower in A model steel that in the other materials.

Model steels K, L, M and N

This study has been carried out by NRG. Figure 56 contains bright-field images obtained with the TEM that show in more detail a fine lath-martensitic structure containing precipitates.
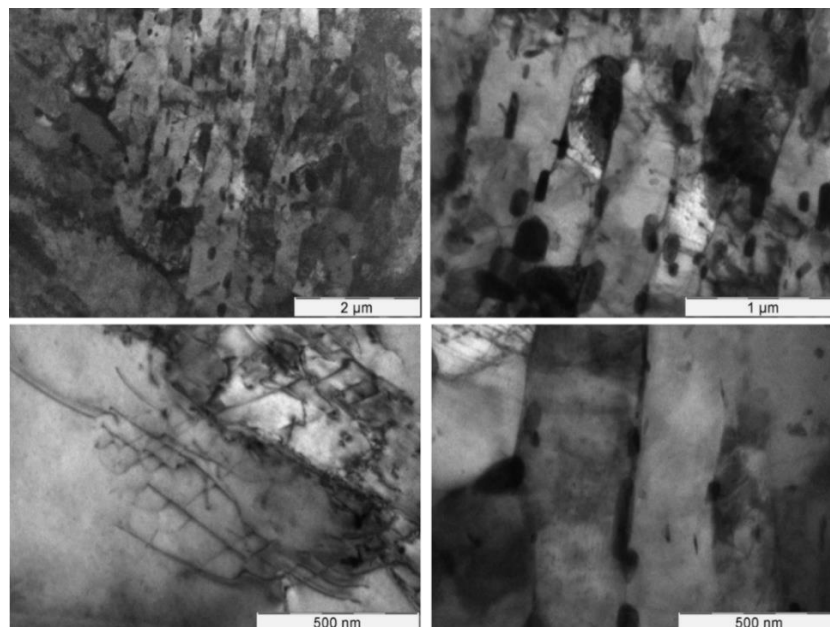
Figure 56: Bright field micrographs of model steel grade K in the reference, un-irradiated condition, (a) and (b) showing a fine lath structure, (c) dislocations and (d) detail showing precipitates (dark features) located preferentially at lath boundaries. The precipitates can also be seen in (a) and (b).

The chemical composition of the precipitates present in grade K, in the un-irradiated condition, was analyzed using the EDS system in the TEM and representative results can be seen in Figure 57, Figure 58 and Table 8, Table 9. The steel grade L has also been analysed by TEM and the results are similar to the obtained for grade K, here presented. The TEM used for this work operates at 120 kV, with a tungsten filament and, therefore, its resolution is limited. The precipitates are very fine, with dimensions ranging from 50 nm (or less) to 500 nm, and, in order to get sufficient signal from the precipitates during the EDS measurements, the smallest spot size had to be used. The acquisition time was 15 min, to increase the total number of counts. In addition, it was only possible to analyze precipitates located close to the edges of the sample hole, where the influence from the chemical composition of the matrix was minimized. Figure 57 and Figure 58 show that the precipitates are also located inside the grains.

In Figure 57 and Table 8, the two precipitates analyzed are rich in Mo and Fe, in agreement with Thermo-Calc predicted composition of the ξ carbide and with the observations of Hernandez and Gomes-Briceno (Hernandez & Gomez-Briceno, 2010) for a RPV steel with similar chemical composition. In Figure 58 and Table 9, the precipitate 1 is rich in Fe and contains Cr, Mn and Mo, resembling the equilibrium composition of M7C3 formed at high temperature (between 600 ºC and 700 ºC). The precipitate 2 seems to be of the same type of precipitate 1, but its compositional analysis is likely affected by the matrix. Points 3 and 4 have the same composition of the ξ carbide. Examination of steel grades M and N with the TEM is still ongoing.
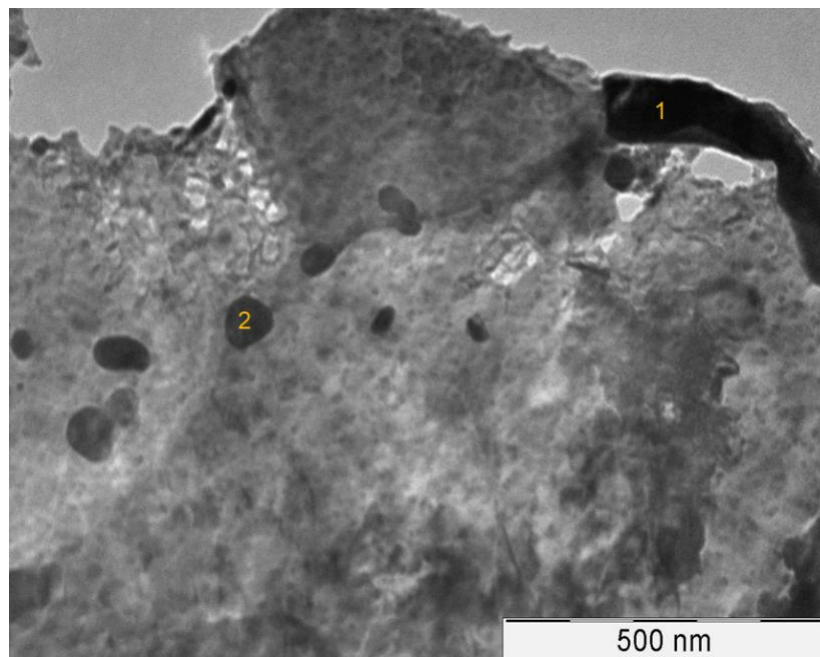
Figure 57: Bright-field micrograph of grade K in un-irradiated condition, showing precipitates.

	C	O	Al	Si	Cr	Mn	Fe	Cu	Mo
Point 1	1.2	1.9	4.29	0.39	0.95	3.35	46.71	0.90	40.43
Point 2	0.5	2.5	4.39	0.54	0.49	-	58.96	0.98	31.39

Table 8: Chemical composition of precipitates indicated in Figure 57, in weight %.
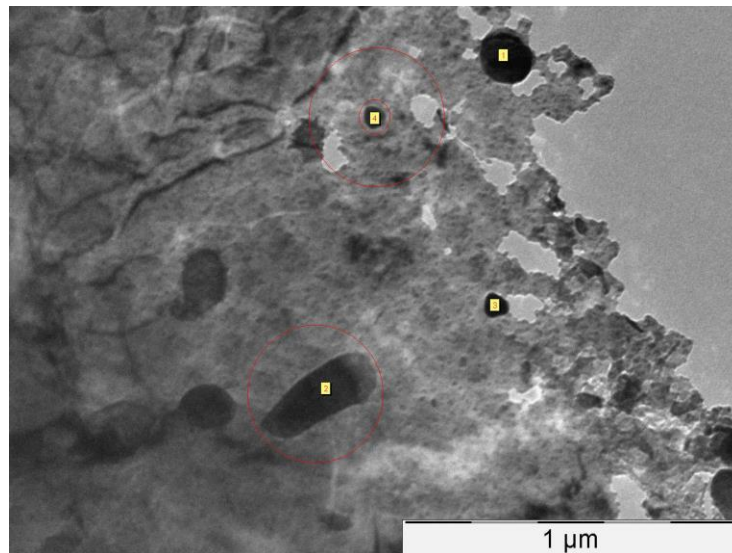
Figure 58: Bright-field image of grade K in the un-irradiated condition, showing in more details precipitates.

	C	O	Al	Si	Cr	Mn	Fe	Cu	Mo
Point 1	2.36	-	4.05	-	2.07	5.73	81.38	1.40	3.00
Point 2	1.16	-	4.07	0.27	0.59	3.06	87.99	0.85	1.63
Point 3	0.22	2.40	4.56	0.64	-	0.84	36.71	1.13	54.66
Point 4	4.68	2.90	3.90	0.46	-	0.62	51.90	1.63	33.92

Table 9: Chemical composition of precipitates indicated in Figure 58, in weight %.

4.4. Atom Probe Tomography

4.4.1. Matrix composition vs nominal composition

As it is shown later, no features were observed in unirradiated alloys using APT. Thus, the average compositions of different unirradiated alloys, measured using APT and presented in Table 10, are the matrix compositions. A comparison between the nominal and the APT (matrix) compositions is shown in Figure 59. After comparing Table 2 and Table 10 or seeing Figure 59, it is clear that the matrix is depleted in C, Mo, Mn, V, Cr, except for Alloy A. The matrix depletion of these elements can be explained by the fact that all these elements are known to precipitate into carbides. Such carbides were observed under the scanning electron

microscope (SEM). For Alloy A, the matrix and the nominal compositions almost match, which is most surprising. No observation of a reduction in the elemental content may be because of the presence of a lower carbide volume fraction in Alloy A. This needs further investigation, at a larger scale than APT.

Alloy	C	Si	Mn	Cr	Ni	Mo	V	Cu	P
A	0.1 ± 0.04	0.26 ± 0.02	0.34 ± 0.04	2.05 ± 0.14	0.03 ± 0.01	0.59 ± 0.07	0.08 ± 0.01	0.05 ± 0.01	0.01 ± 0.001
B	0.02 ± 0.01	0.25 ± 0.03	0.27 ± 0.02	1.14 ± 0.16	0.9 ± 0.05	0.51 ± 0.03	0.03 ± 0.001	0.04 ± 0.01	0.01 ± 0.001
C	0.02 ± 0.08	0.22 ± 0.01	0.28 ± 0.01	1.21 ± 0.15	1.91 ± 0.12	0.51 ± 0.03	0.05 ± 0.15	0.06 ± 0.16	0.01 ± 0.001
F	0.02 ± 0.001	0.33 ± 0.01	1.03 ± 0.02	1.33 ± 0.12	0.97 ± 0.03	0.5 ± 0.001	0.05 ± 0.001	0.05 ± 0.003	0.01 ± 0.001
G	0.04 ± 0.01	0.33 ± 0.01	1.08 ± 0.06	1.43 ± 0.13	2.02 ± 0.1	0.52 ± 0.05	0.03 ± 0.001	0.06 ± 0.001	0.01 ± 0.002
H	0.03 ± 0.01	0.52 ± 0.01	1.17 ± 0.06	1.45 ± 0.14	2.06 ± 0.25	0.33 ± 0.04	0.03 ± 0.004	0.06 ± 0.007	0.01 ± 0.004

Table 10: The APT matrix composition (wt%) of different unirradiated alloys
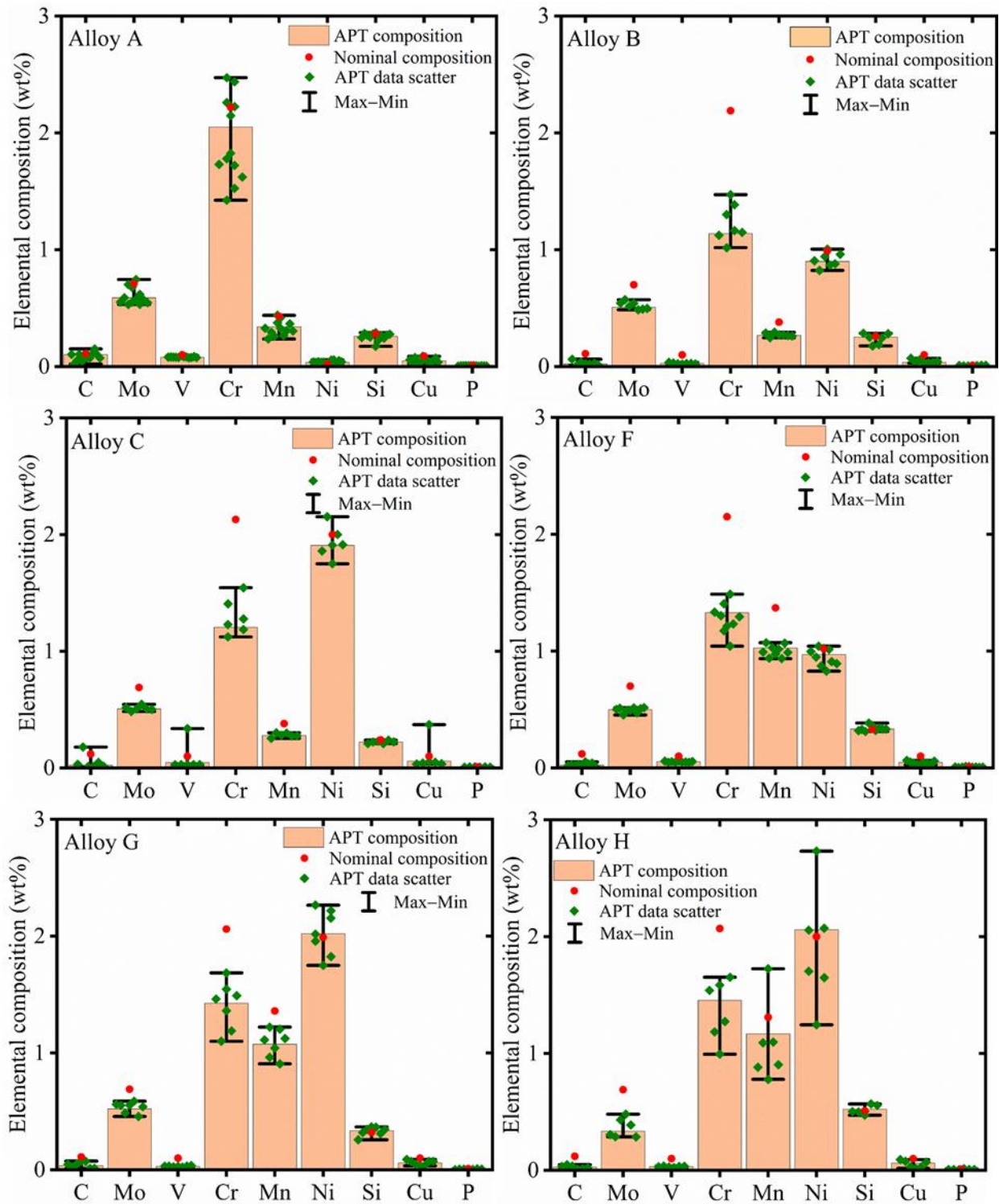
Figure 59: The figures show the bulk composition of different unirradiated alloys and the matrix composition measured by APT.

4.4.2. Atom maps

The atom maps for the unirradiated alloy A, B, C, F, G, and H are shown in Figure 60, Figure 61, Figure 62, Figure 63, Figure 64 and Figure 65, respectively. Homogenous distribution of all elements, i.e. no clustering or precipitates is observed in all unirradiated alloys. No carbides

were observed under APT analyses, which were seen under SEM. The atom maps for Mn, Ni, and Si elements were overlapped to see if there is any MNS precipitates in the materials – which is clear from the atom maps that there are no. Considering the whole volume analysed in each material, if there are such clusters/precipitates, their number density is lower than about 3×10^{21} m^{-3}.
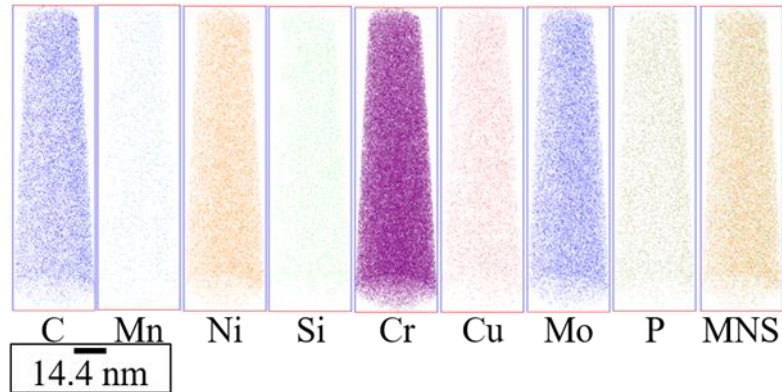
Figure 60: Atom maps for unirradiated alloy A.
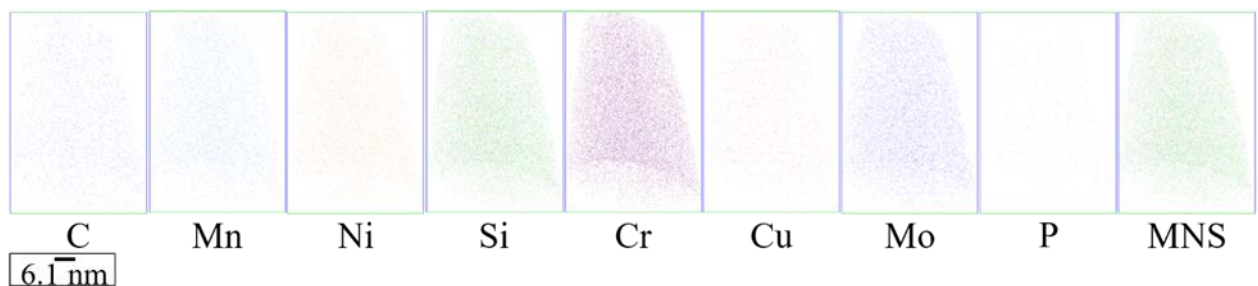
Figure 61: Atom maps for unirradiated alloy B.
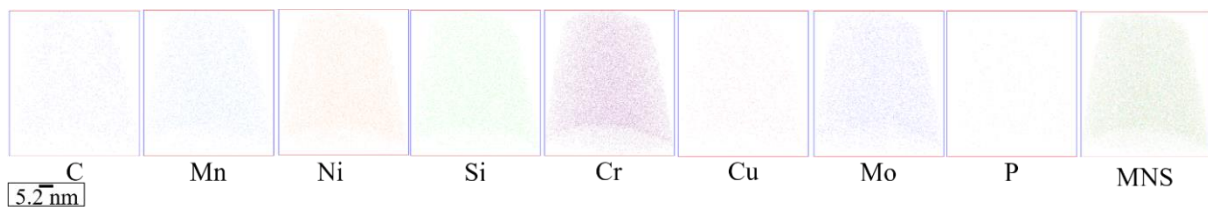
Figure 62: Atom maps for unirradiated alloy C.
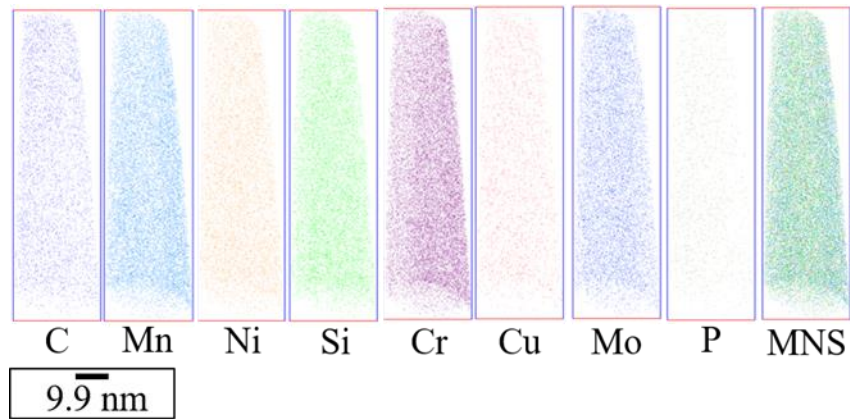
Figure 63: Atom maps for unirradiated alloy F.
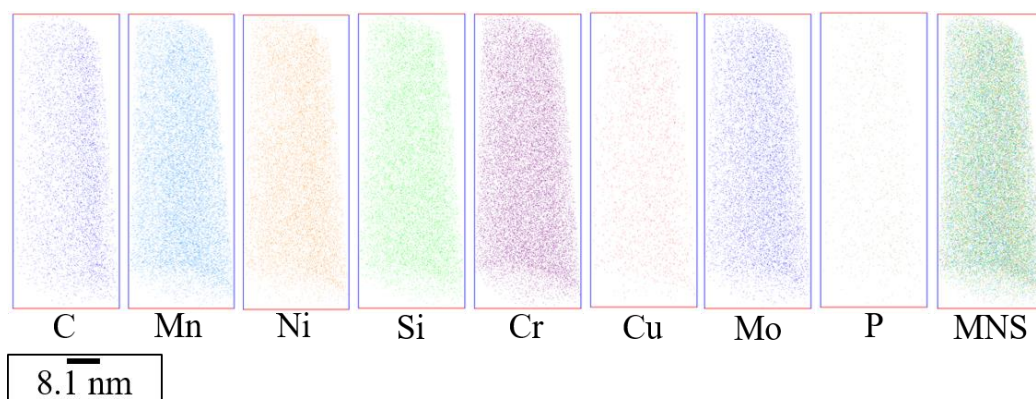
Figure 64: Atom maps for unirradiated alloy G.
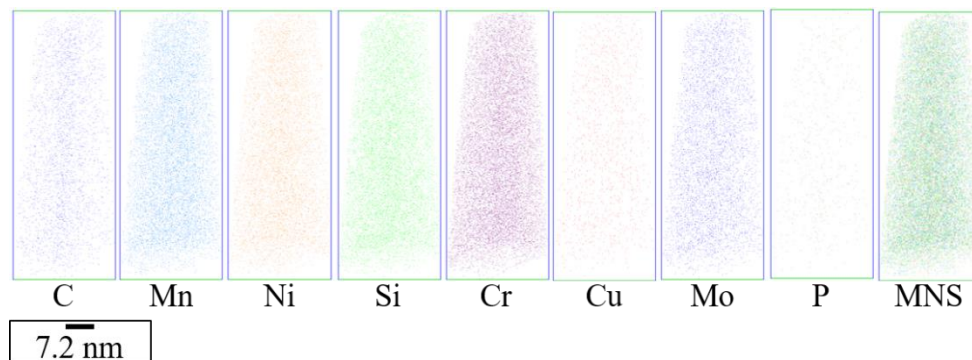
Figure 65: Atom maps for unirradiated alloy H

4.4.3. First nearest neighbor (1NN) distance distribution

To clarify whether there is any clustering in the material or it is homogenous, as observed from atom maps, experimental first nearest neighbor (1NN) distance distributions were plotted and compared with the random ones. The experimental and random distributions show the same behavior (overlapping curves) for all the elements. The results for Alloy A, B, C, F, G, and H are shown in Figure 66. Although all the elements showed similar results for measured and random distribution, only Mn, Ni, and Si distribution are shown in these figures.
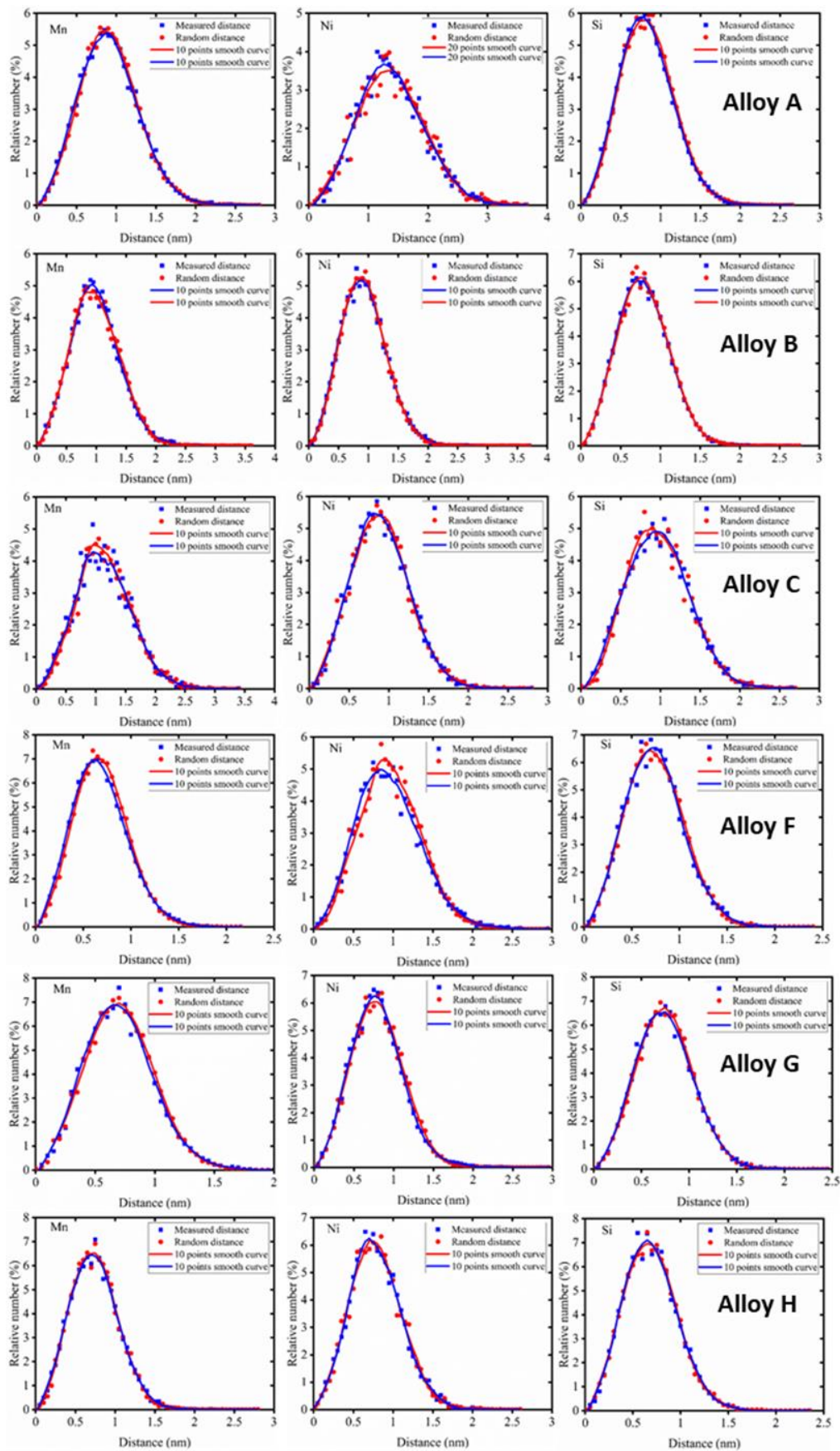
Figure 66: 1NN distance distribution for Mn, Ni, and Si elements in alloys A, B, C, F, G, and H.

4.5. Positron Annihilation Spectroscopy

The reference specimens of model steels (MS) were submitted to positron annihilation lifetime (PALS) and coincidence Doppler broadening spectroscopy measurements (CDBS). As it was mentioned before (chapter 3.5) the same geometry will be kept for irradiated and reference specimens. To provide a good reproducibility of the obtained results, all specimens were measured on two different positron lifetime setups and one CDBS setup (combined setup with one PALS).

Source contribution, important for PALS spectra evaluation, was obtained separately for two different positron sources used in the experiments. It was set as a global variable and found to be 23.3 +- 0.2 % for the source No.1 (used in the setup referred to as PALS 1) and 26.2 +- 0.1% for the source No.2 (used in the setup referred to as PALS 2 - coupled with CDBS spectrometer)

4.5.1. Positron annihilation lifetime spectroscopy (PALS)

For the evaluation of the positron lifetime spectra, LT ver.10.0 program [20] was used. In total, four sets of iterations were used independently for the unirradiated samples measured on the two different lifetime spectrometers. In the first approach, positron mean lifetime, as statistically most reliable parameter, was looked for in the fitting results of two-component spectra decompositions. In this step, the lifetimes of the two components were fixed to 120ps and 190ps, attributed to bulk + dislocations and vacancy-type point defects, respectively. Using this procedure, global fitting variance (reduced chi-squared) better than 1.05 was obtained. This corresponds to a reasonably good fit, however, obtaining of qualitative and quantitative data in terms of dislocation-type defects and vacancy-type defects is problematic in two-component decomposition, when more than one type of lattice defects is present. Nevertheless, already these results pointed to presence of dislocations in reference samples. Also, the hint of the fact that positron lifetime (trapping at defects) increases with the Ni-Mn content can be found (see Figure 67). Nevertheless, it is important to emphasize that, there are strong indications of the role of other elements in this plot. Further evaluation is needed to provide a more detailed interpretation.
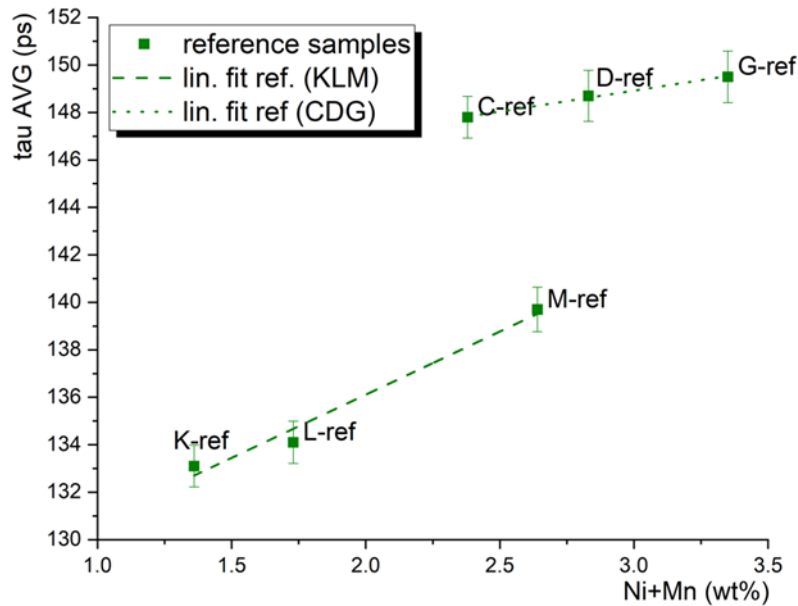
Figure 67: Positron lifetime (trapping at defects) as a function of Ni-Mn content.

In the next step, three-component fitting model was used for the spectra decomposition. In this model, the first component was attributed to defect-free material bulk (reduced according to the standard trapping model, the second component was attributed to dislocations (~150 ps) and the third component was corresponding to vacancy-type defects (~190 ps). This model is expected to be suitable for irradiated samples, where the third component will primarily describe radiation induced defects in the studied materials. This model was found to be slightly worse reduced chi squared for some samples, but this was due to more degree of freedom in the fitting, where the lifetimes were not fixed. The example of fitting model can be seen in Figure 68, where the decomposition of the positron lifetime spectra of reference MS-M sample is shown.
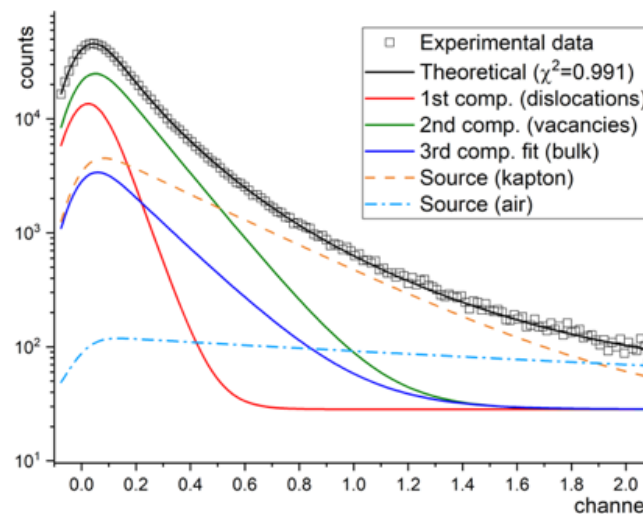
Figure 68: Decomposition of the positron lifetime spectra of reference MS-M sample.

The positron lifetimes, including the mean positron lifetime for each sample, obtained from the three-component spectra decomposition are listed in Table 11. It is important to note that

the positron mean-lifetime, which is an intensity-weighted average of τ_1 - τ_3, was found to be higher by about 16 ps in the 3-comp. decomposition model for all reference samples, as compared to 2-component model (see Figure 69). The over-estimation of the MLT value in the 2-compoment model is typical for samples with more than one defect component where the bulk component cannot be effectively separated from the component describing some shallow traps (such as dislocations).

Reference samples	Sample ID	MLT [ps]	MLT Err [ps]
τ_1 [ps]	A	124.0	2.6
	B	127.5	2.3
14.8 - 27.1	C	128.8	2.6
	D	128.3	2.3
τ_2 [ps]	E	127.6	1.4
	F	129.0	1.1
149.6 ± 0.84	G	129.1	0.7
	H	127.6	1.3
τ_3 [ps]	K	118.7	3.4
	L	120.0	3.3
200.0 ± 3.7	M	120.5	1.1
	N	117.9	2.5

Table 11: Positron lifetime values obtained from three-component spectra decompositions using two independent lifetime spectrometers.

Figure 69: The positron mean-lifetimes obtained from 2-component and 3-component fitting models for reference samples.

Since the positron lifetimes of the two defect components did not vary significantly between the fitting iterations, we estimated the number density of the defects identified in the samples. In the first case, defects with positron lifetime 146 – 150 ps were considered as dislocations, with specific positron trapping rate of 6×10^{-5} m^2s^{-1}. This value was taken from the literature as an average specific trapping rate reported for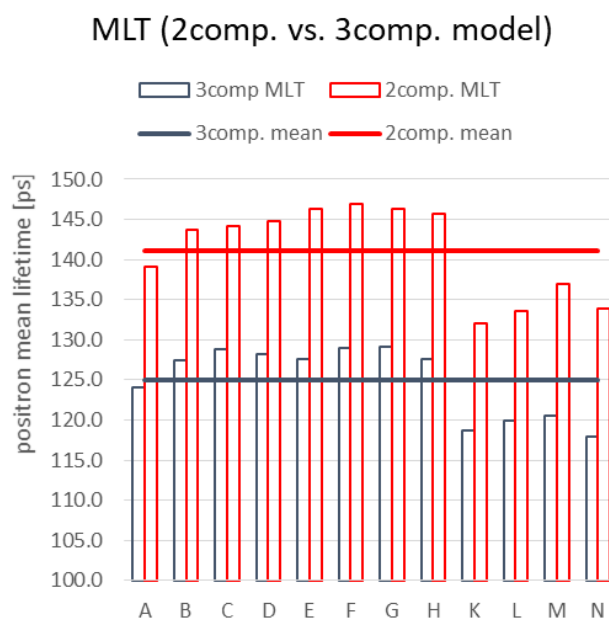 edge and screw dislocations [Dislocation studies on deformed single crystals of high-purity iron using positron annihilation: Determination of dislocation densities [21]. As can be seen in the Figure 70, the four model steel K, L, M and N show a slightly lover dislocation density in unirradiated state.
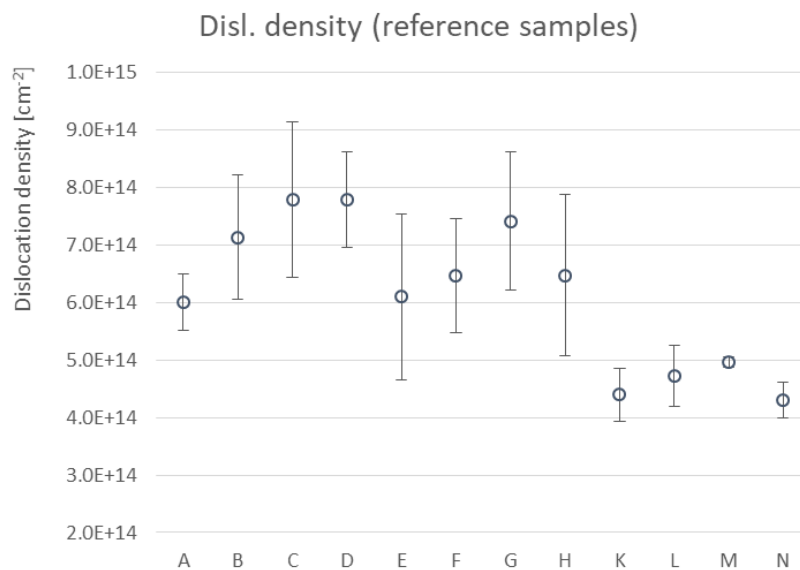
Figure 70: Estimated dislocation density obtained from positron lifetime spectra of reference samples.

For the further quantitative analysis of the radiation induced vacancy-type defects, the specific trapping rate for monovacancies in iron (1.3×10^{-14} m^3s^{-1}) was used. The results shown in the Figure 71 are calculated with this specific trapping rate, although the obtained positron lifetime values enable to consider small vacancy clusters. With positron trapping coefficient being linearly dependent on the cluster size up to ~10 vacancies, we can expect the resulting number density to be n-times smaller for a cluster of n-vacancies. Nevertheless, the n is not expected to be higher than 2 – 4 and no dependency on the chemical composition of the steel was observed in the fittings of the data. It is important to note, however, that the lifetime of the defect components was set as a global free parameter, so one value was being determined for all samples. In the unirradiated samples, the vacancy component couldn't be clearly distinguished in the RPV steels (K, L, M, N) and low-alloyed MS-A steel. This suggests the concentration near or below the resolution of the PALS technique in terms of monovacancies in Fe, which is ~ 8.5×10^{21} m^{-3} (0.1 appm) [22].
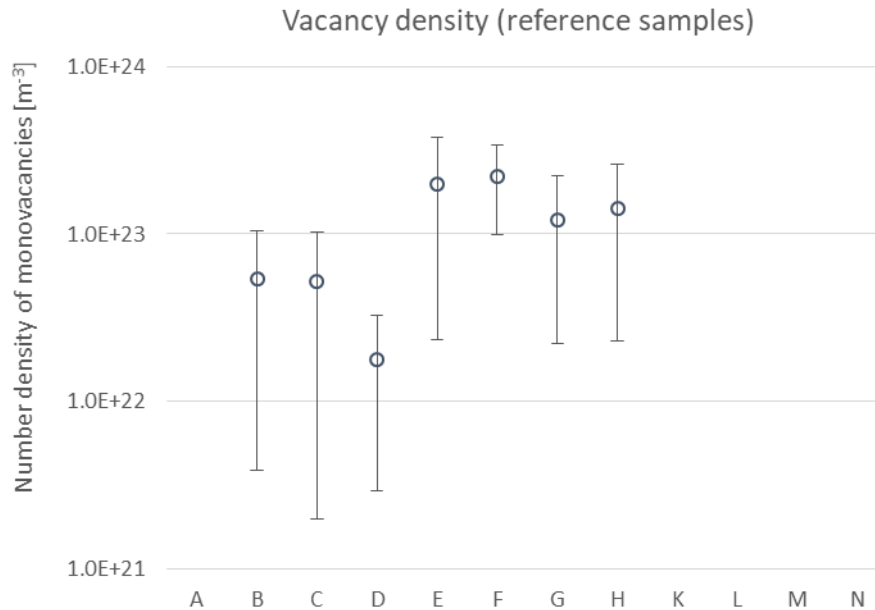
Figure 71: Estimated (mono)-vacancy density obtained from positron lifetime spectra of reference samples.

We would like to underline the fact, that the positron lifetime data presented in this work are average values obtained from two independent positron lifetime spectrometers using two different 22Na-bases positron sources prepared in our laboratories. The error bars presented have been obtained as a standard deviation of two positron lifetime measurement of each from the 12 samples. The results shown indicate a very good reproducibility of the PALS data and demonstrate the important role of this technique in the post-irradiation examination (PIE) of nuclear structural materials.

4.5.2. Coincidence Doppler broadening spectroscopy (CDBS)
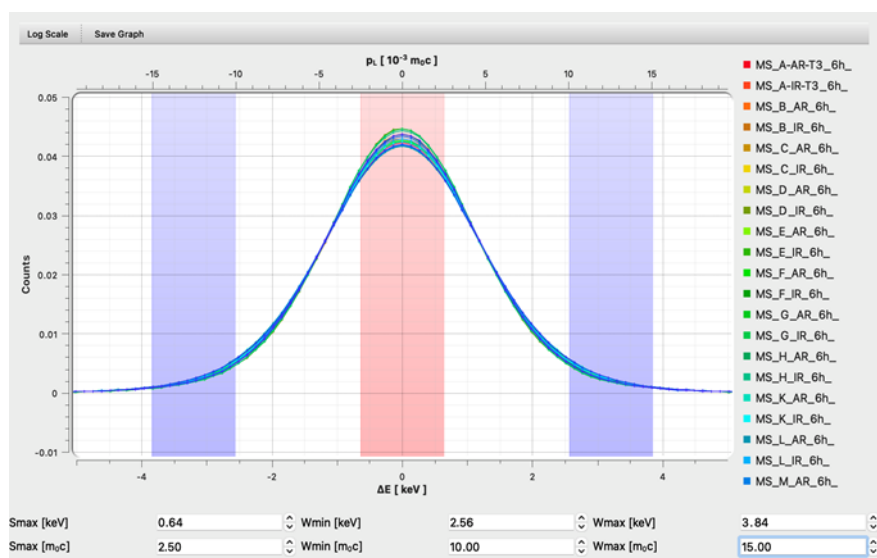
Figure 72: Screenshot from the CDB Tools software used for CDBS data treatment [19]

The reliability of the so-far presented results can be further supported by the results of the CDBS measurements (see Figure 72). Numerous previous experiments published on irradiated steel samples demonstrated an excellent correlation between the positron mean lifetime and Doppler broadening S-parameter, which represents the annihilation with valence/free electrons and increases with positron trapping at defects. Figure 73 shows similar correlation for our reference PALS and CDBS data.
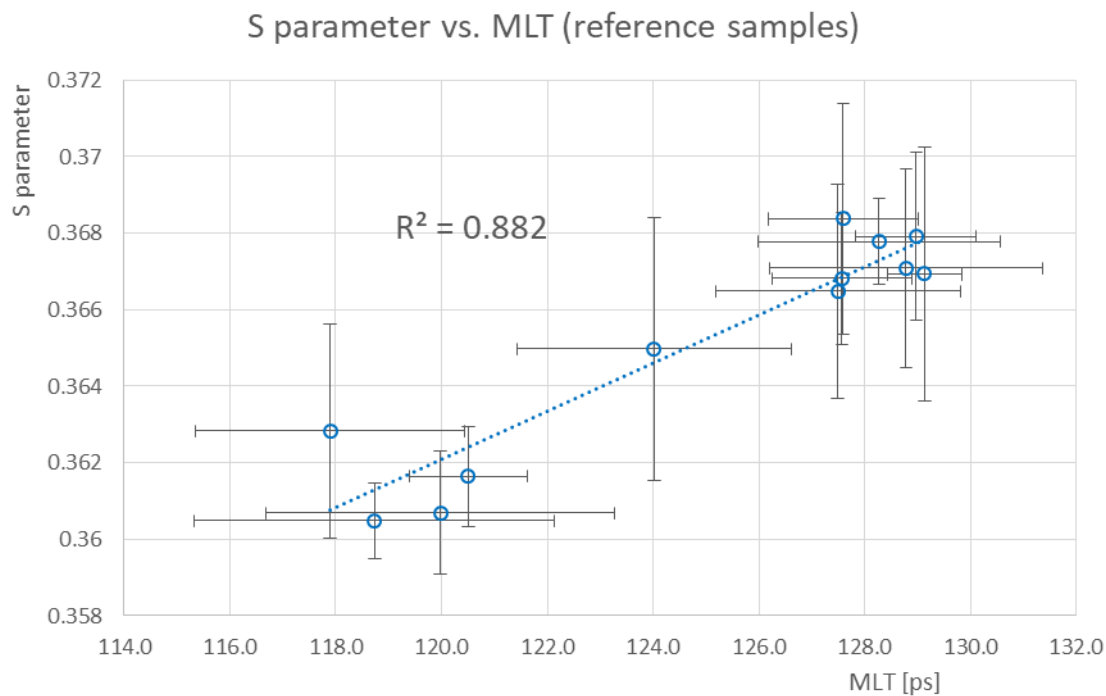
Figure 73: S parameter vs. positron mean lifetime, obtained from reference samples data.

Similarly, the DBS W-parameter, which represent the annihilation with core electrons, was found to have a reasonably good correlation with the positron lifetime of the first component τ_1. As shown in the Figure 74, the reduced bulk lifetime component τ_1 describing delocalized positrons reasonably correlates in the reference samples with the W-parameter obtained on these samples. This correlation justified the trapping model used and validate the values of the τ_1 which was obtained independently for each sample.
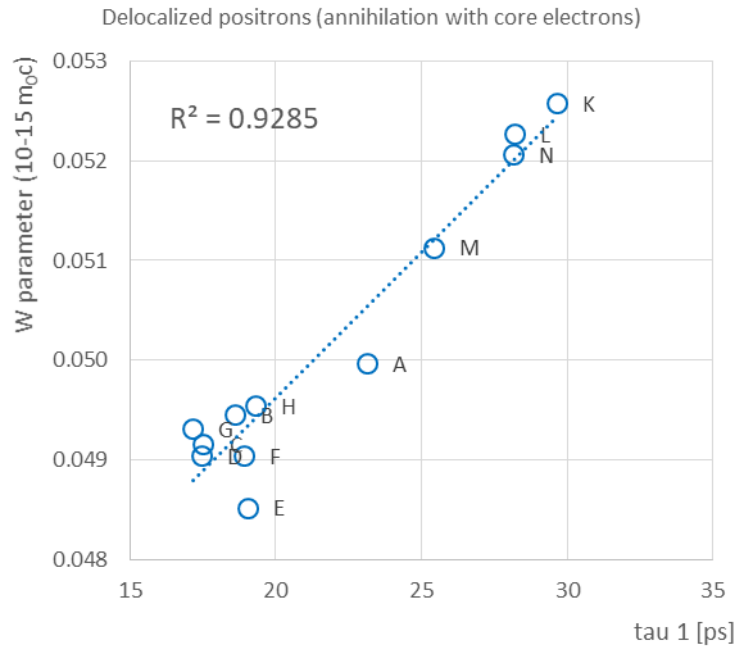
Figure 74: W parameter vs. reduced bulk-lifetime component obtained for reference samples.

The choice of momentum ranges of the W parameter was considered in the evaluation of the CDBS data. Figure 75 compares two different selections of the range, namely the "conventional" range 15-25 m_0c and slightly reduced range 10-15 m_0c. Since the high-momentum data are rather scattered (exhibiting large error bars) and complicates the interpretation of the CDBS results, we decided to further evaluate the W parameter obtained with the reduced momentum range.
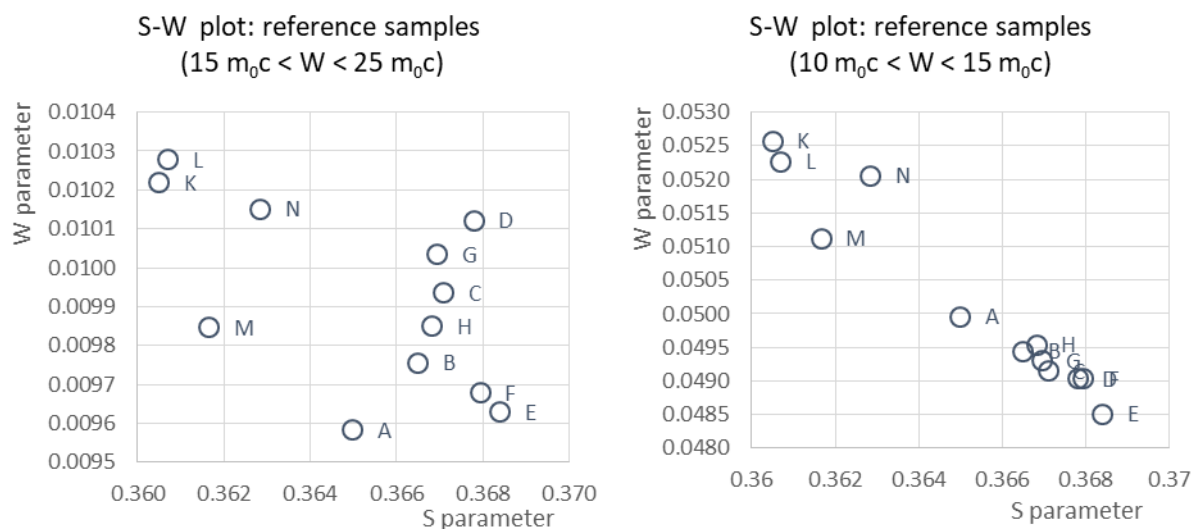
Figure 75: Comparison of S-W plots for two different momentum ranges of the W parameter.

The effect of chemical composition on the microstructure of the studied materials was also investigated using the shape of momentum curves. Figure 76 shows relative momentum curves obtained for all reference samples as a ratio to the MS-A sample with lowest content

of alloying elements. What can be distinguished in the spectra are two major bands of the A-H and K-N momentum lines, respectively. From the chemical composition point of view the major difference between the two groups of samples is the chromium content. As discussed above, there is an obvious difference between the positron trapping in these groups in both dislocation density and concentration of point defects. The distinctions between the corresponding CDBS momentum curves are therefore likely a consequence of the microstructural defects. Due to the low Cr affinity comparing to Fe, the preferential trapping of positrons on Cr-associated nano-features is likely negligible.

Figure 76: CDBS momentum curves of the irradiated samples relative to low-alloyed MS-A sample.

The role of chromium in the behavior of radiation-induced point defects can be eventually investigated by comparing the S or W parameter as a function of Cr content for reference samples. Such comparison (Figure 77) suggests that the Cr affects the formation of the initial microstructure of the studied model steel.
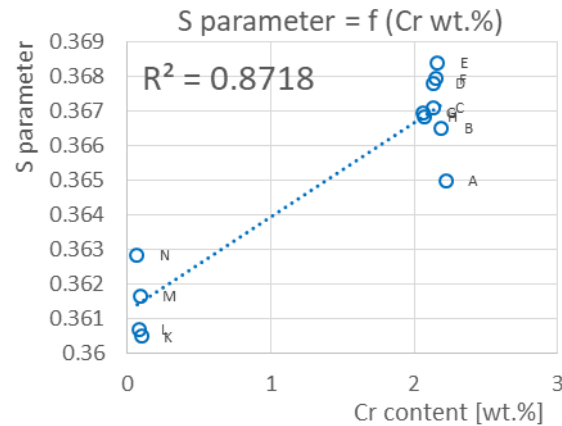
Figure 77: A comparison of S parameter vs. Cr content in reference model steel samples.

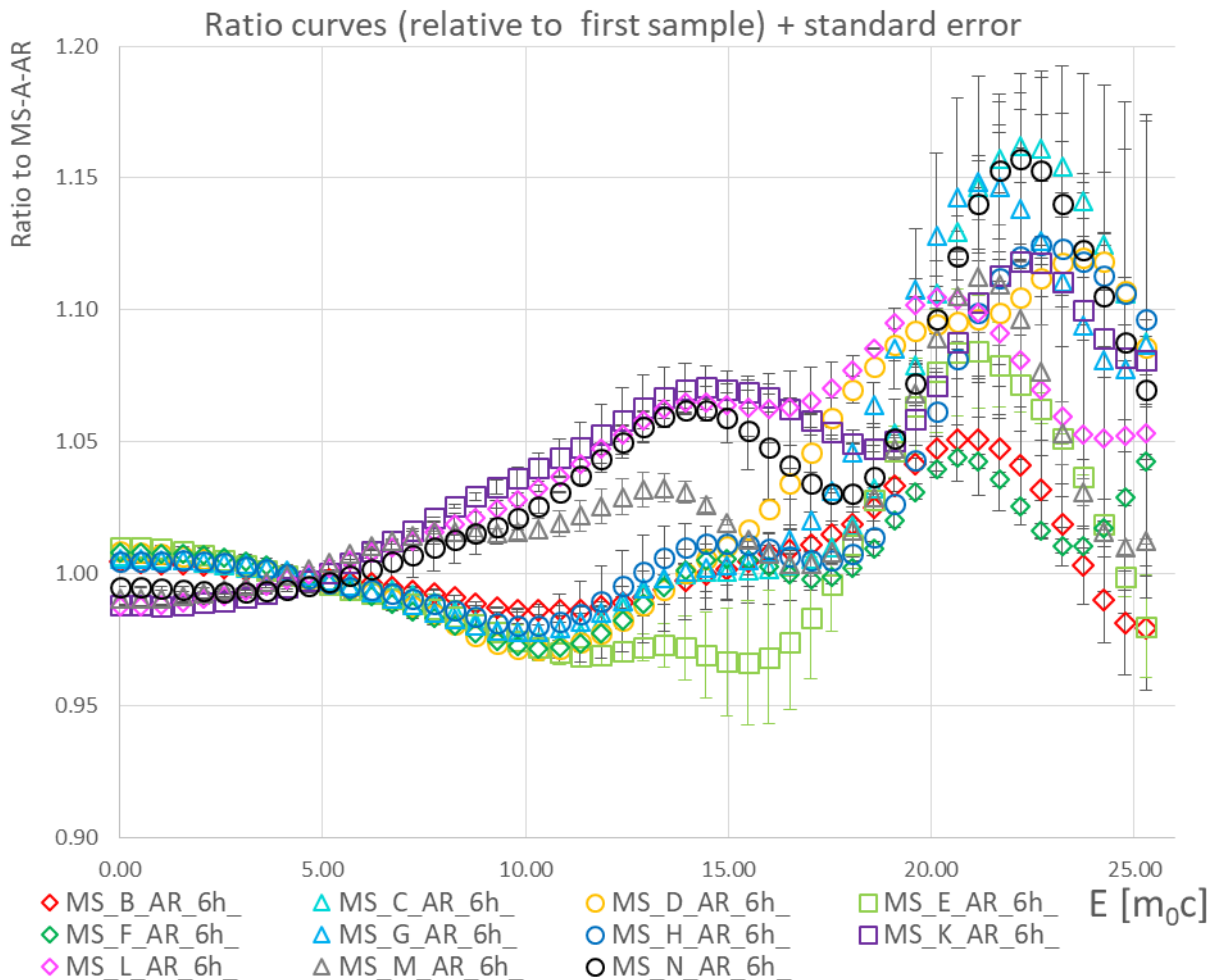Based on the current knowledge of the radiation and thermal-induced processes in the RPV steels, we assume that the production, but mostly the survival rate, of the radiation-induced vacancies will be strongly affected by the formation and growth of precipitates. If the vacancies are associated with the interfaces of these precipitates, the trapping (positron lifetime, S parameter) but also the W parameter shall be depending on the content of precipitate-forming elements such as Ni, Mn and Cu. Figure 78 shows the dependency of the W parameter on the content of these elements weighted over their positron affinity. Let us compare two sets of samples A-C and K-M, which differs in Ni. One can see a linear dependency on the given chemical factor with a small difference in the slope between the A-C and K-M line. We assume that this slope is mostly due to Cr and Mn content which composition is different in the two sample sets.
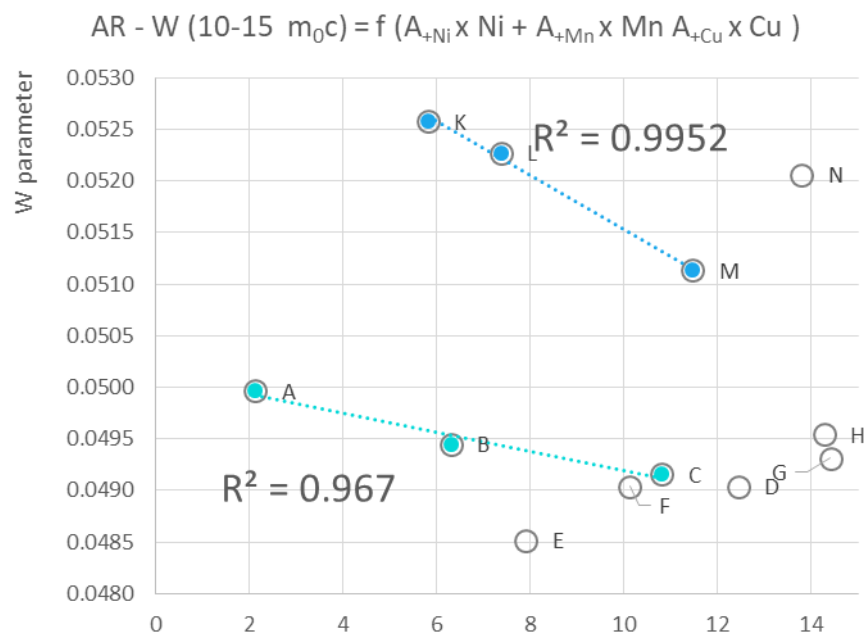
Figure 78: W parameter of reference samples plotted as a total content of Ni, Mn and Cu in wt. %, weighted over their positron affinity.

PAS summary

• The dislocations were found in reference samples, the model steel K, L, M and N show a slightly lower dislocation density in unirradiated state then the rest of the studied samples.

• The hint of the increase of the positron lifetime (trapping at defects) with the Ni-Mn content was found. But there are strong indications of the role of other elements in this trend.

• In the unirradiated samples the vacancy component couldn't be clearly distinguished in the K, L, M, N and low-alloyed MS-A steel. This suggests the concentration near or below the resolution of the PALS technique in terms of monovacancies in Fe, which is ~ 8.5 x 10^{21} m^{-3} (0.1 appm).

• The correlation between the positron mean lifetime and Doppler broadening S-parameter, as well as between τ_1 (describing delocalized positrons) and W-parameter which represents the annihilation with valence/free electrons and increases with positron trapping at defects was confirmed.

• The shape of momentum curves shows the chromium content as a major difference among the MS, suggesting that the Cr affects the formation of the initial microstructure of the studied model steel.

• From the slope of the W parameter as a function of Ni, Mn and Cu elements, weighted over their positron affinity, the Cr and Mn content seem to play an important role

• The measurements on the irradiated samples are expected reveal the effect of the vacancy-type defects sinks (such as precipitates-matrix interfaces) and contribute to the understanding of the role of certain elements on RPV material behavior.

5. Conclusion

In the study of the initial microstructure of model steels (A, B, C, F, G and H) the main difference was found in the case of steel A. All the materials present a bainitic microstructure but in the case of A model steel there are also small islands of ferrite with a volume fraction of 13%. The presence of ferrite in this material could be associated with the absence of Ni and low amount of Mn. Both are gamma stabilizers, so their absence promotes the presence of alpha phase. On the other hand, according with EBSD results, the origin of ferrite islands is given by bainitic transformation and not by independent nucleation, since these ferritic islands are not separated by any grain boundary to the adjacent bainite microstructure as they have a similar orientation.

Studying the other model steels in was found, by means of EBSD analysis, that the steels B, C and G exhibit a smaller grain size and a pronounced presence of small angle grain boundaries that may be explained by different preferred variant selections during the bainitic transformation. This is in agreement with de dislocation density values. Even though the values estimated by PAS is slightly higher than the one measured by means of (S)TEM, the evolution found for the different model steels is the same. A, F and H have lower values of dislocation density compared with B, C and G model steels. The lower values of dislocation densities obtained by TEM can be associated to the fact that one family of 100 dislocations is missing in all the cases since the measurements were done with grains oriented on zone axis [110]. The same tendency was observed for the lath width that is thicker for steels F and H (higher average grain size (Table 6)) compared to steels B, C and G.

Two families of precipitates were found in the materials. The first one corresponds to carbides with Cr, Mn, V and/or Mo mainly and are placed in general at grain boundaries. In the case of A model steel there are a significant lower volume fraction of these precipitates. Thus, by APT it is clear that the matrix is depleted in C, Mo, Mn, V, Cr, in all the studied materials except for steel A. No observation of a reduction in the elemental content may be because of the presence of a lower carbide volume fraction in steel A as has been observed by SEM and TEM. The second family of precipitates corresponds to small V-rich precipitates (likely nitrides) placed within grains with a mean size below 10 nm. By means of APT, no clustering or precipitates were observed in all unirradiated steels. No precipitates were observed under APT analyses, which were seen under SEM and TEM. Considering the whole volume analysed in each material, if there were such clusters/precipitates, their number density should be lower than about 3×10^{21} m^{-3}.

Regarding K, L, M and N model steels grades K and L have similar microstructures, composed of tempered martensite, bainite and two types of precipitates: ξ carbide and likely M7C3. The microstructures of steels grades M and N are more complex, composed of a mixture of ferrite, bainite and martensite and, only for grade N, fine precipitates. The volume fraction of precipitates in grade N is qualitatively lower than the observed in grades K and L. Optical microscopy analysis (not presented here) has shown the presence of retained austenite in grade M, which can be expected in this kind of material. The microstructure seen in Figure 34 and the equilibrium diagram in Figure 32 suggest that a low volume fraction of austenite was

formed during the heat treatment at 640 ºC for 12 h. Cooling to room temperature, in air, leads to austenite decomposition into ferrite, bainite, possibly a fraction of martensite and to the retention of austenite. Hence, the final microstructure of steel grade M is composed of the latter microconstituents and tempered martensite and bainite, which were previously formed during water quench, after austenitization at 900 ºC.

Analysis by means of PAS shows the model steel K, L, M and N have a slightly lower dislocation density in unirradiated state then the rest of the studied samples.

6. Bibliography

[1] R. Krause Rehberg, Positron Annihilation Spectroscopy on Defects in Semiconductors, presentation ICDS 2015.

[2] M. F. McCann, K. M. Smith, Direct measurement of the K electron capture to positron emission ratio in the decay of 22Na, J. Phys. A: Gen. Phys. 2 (1969) 392

[3] M. J. Puska, P. Sanku, R. M. Nieminen, Positron affinities for elemental metals, J. Phys. Condens. Matter 1 (1989) 6081.

[4] R. Krause-Rehberge, S. H. Leipner, Positron annihilation in Semiconductors. Springer, Berlin, Germany, 1998. ISBN 3-540-64371-0

[5] J. Simeg Veternikova, Study of Materials for Advanced Reactor Systems, Doctoral thesis, FEI STU Bratislava 2012

[6] P. Hautojärvi, L. Pöllänen, A. Vehanen, J. Yli-Kauppila, Vacancies and carbon impurities in α-iron: Neutron irradiation, J. Nucl. Mater. 114 (1983) 250, P. Hautojärvi, Positrons et Solids, Springer, Berlin, p.89, 1979

[7] P. Hautojärvi, Positrons et Solids, Springer, Berlin, p.89, 1979

[8] R. Krause-Rehberge, S. H. Leipner, Positron annihilation in Semiconductors. Springer, Berlin, Germany, 1998. ISBN 3-540-64371-0

[9] P. Hautojärvi, L. Pöllänen, A. Vehanen, J. Yli-Kauppila, Vacancies and carbon impurities in α-iron: Neutron irradiation, J. Nucl. Mater. 114 (1983) 250

[10] V. Kršjak, Positron annihilation study of advanced nuclear reactor materials, Doctoral thesis, FEI STU, Bratislava, Sept., 2008.

[11] J. Kansy, J.: Nucl. Instrum. Meth., vol. A 374, 1996, pp. 235

[12] S. Pecko, Analysis of Reactor Pressure Vessel Steels using Positron Annihilation Spectroscopy, Dctoral thesis, FEI STU, Bratislava 2016

[13] R. Krause-Rehberge, S. H. Leipner, Positron annihilation in Semiconductors. Springer, Berlin, Germany, 1998. ISBN 3-540-64371-0

[14] V. Sabelova, V.: Study of the radiation resistance of alloys based on Fe-Cr. Doctoral thesis, INPE FEI STU, 2014.

[15] S. Pecko, Analysis of Reactor Pressure Vessel Steels using Positron Annihilation Spectroscopy, Doctoral thesis, FEI STU, Bratislava 2016

[16] V. Sabelova: Study of the radiation resistance of alloys based on Fe-Cr. Doctoral thesis, INPE FEI STU, 2014

[17] W. Anwand. et al.: Appl. Surf. Sci., vol. 194, 2002, pp. 131-135

[18] S. Abhaya, G. Amarendra: Phys. Status Solidi C, vol. 6(11), 2009, pp. 2519–2522

[19] M. Petriska, M. et al.: Physics Procedia, vol. 35, 2012, pp. 117 – 121.

[20] D. Giebel, J. Kansy, Physics Procedia, Volume 35,2012,122-127,ISSN 1875-3892

[21] Y.Park, J. T. Waber, M. Meshii, C. L. Snead, Jr., C. G. Park, Phys. Rev. B 34, 823 (1986), J Kočík, E Keilová, J Čížek, I Procházka,Journal of Nuclear Materials, Volume 303, Issue 1,2002, 52-64,ISSN 0022-3115

[22] R. Krause-Rehberge, S. H. Leipner, Positron annihilation in Semiconductors. Springer, Berlin, Germany, 1998. ISBN 3-540-64371-0

STRUMAT-LTO

Structural Materials for Nuclear Safety and Longevity

🌐 www.strumat-lto.eu

✉ contact@strumat-lto.eu